LASER-INDUCED ACOUSTIC DESORPTION ATMOSPHERIC PRESSURE PHOTOIONIZATION MASS SPECTROMETRY FOR COMPLEX MIXTURE ANALYSIS

A Dissertation
Presented to
The Academic Faculty

by

Kevin Andrew Benham

In Partial Fulfillment
of the Requirements for the Degree
Doctorate of Philosophy in the
School of Chemistry and Biochemistry

Georgia Institute of Technology
May 2019

LASER-INDUCED ACOUSTIC DESORPTION ATMOSPHERIC PRESSURE PHOTOIONIZATION MASS SPECTROMETRY FOR COMPLEX MIXTURE ANALYSIS

Approved by:

Dr. Thomas Orlando, Advisor
School of Chemistry and Biochemistry
Georgia Institute of Technology

Dr. Ronghu Wu
School of Chemistry and Biochemistry
Georgia Institute of Technology

Dr. Facundo Fernandez
School of Chemistry and Biochemistry
Georgia Institute of Technology

Dr. Faisal Alamgir
School of Materials Science and Engineering
Georgia Institute of Technology

Dr. Amanda Stockton
School of Chemistry and Biochemistry
Georgia Institute of Technology

Date Approved: February 27th , 2019

Seek the truth, always question, and be ever vigilant of truth's many imposters.

ACKNOWLEDGEMENTS

Beginning with the agencies responsible for supporting this work, I must first acknowledge the Center for Chemical Evolution at the Georgia Institute of Technology for their continued and unwavering support of this research. Additionally, this work acknowledges the parent organizations, the National Science Foundation (NSF) and National Aeronautics and Space Administration (NASA) for bestowing the Georgia Institute of Technology with this prestigious research center.

On an individual basis, I'd first like to make mention of the difficult and pioneering work of my predecessor, Dr. Joshua Symonds and for leaving me with a feasible and promising body of microplasma work to build upon. Other notable mentions of colleagues in my time in the EPICS lab include Dr. Reuben Gann for providing myself and others with extensive practical lab knowledge and the example he set as an inquisitive and thorough scientist. I must also thank my close classmates and colleagues, Aaron McKee, Alex Elder, Brant Jones, Micah Schaible, and Alma Castaneda for their support throughout this journey. And of course, I thank my advisor Professor Thomas Orlando for giving me the freedom and space to pursue my curiosities and interests, even when they may have been tangential to this research.

Aside from the EPICS lab I would also like to thank the members of the Fernández lab for their help on getting started with the complex instrumentation employed throughout this work. I also wish to thank Professor Facundo Fernández for the significant amount of resources provided through his lab to reach the accomplishments made by this research.

The progress afforded through the kind gifts of instrument time and usage was crucial to the success of this work.

Lastly, I would like to thank my fiancé Elyse Paske, and my family. Your support, kindness, and encouragement have been indispensable throughout this odyssey.

TABLE OF CONTENTS

LIST OF TABLES

LIST OF FIGURES

LIST OF SYMBOLS AND ABBREVIATIONS

AH	Azerbaijan aromatic-naphthenic heavy sweet crude
API	atmospheric pressure ionization
APPI	atmospheric pressure photoionization
APCI	atmospheric pressure chemical ionization
AP-MALDI	atmospheric pressure matrix-assisted laser desorption/ionization
atm	atmosphere, pressure unit (=101325 Pa)
CI	chemical ionization
CFD	computational fluid dynamics
csv	comma-separated values
Da	Dalton, mass unit (= 1.66e-27 kg)
DAPPI	desorption atmospheric pressure photoionization
DBE	double-bond equivalent
DC	direct current
DESI	desorption electrospray ionization
EA	electron affinity
EI	electron impact ionization
ESI	electrospray ionization
eV	electron-volt, energy unit
EVOO	extra-virgin olive oil
FAPA	flowing atmospheric pressure afterglow
FT-ICR	Fourier-transform ion-cyclotron resonance
IE	internal energy
IP	ionization potential

LAAPPI	laser ablation atmospheric pressure photoionization
LAESI	laser ablation electrospray ionization
LIAD	laser-induced acoustic desorption
LTP	low-temperature plasma ionization
MALDI	matrix-assisted laser desorption/ionization
MHCD	micro-hollow cathode discharge
MS	mass spectrometry
MSI	mass spectrometry imaging
NaTFA	sodium trifluoroacetate
NIST	National Institute of Standards and Technology
Pa	Pascal, pressure unit
PA	proton affinity
PADI	plasma assisted desorption/ionization
PCA	principal component analysis
ppb	parts-per billion
ppm	parts-per million
qTOF	quadrupole time-of-flight
rf	radiofrequency
SRM	standard reference material
SWIFT	stored-waveform inverse Fourier-transform
T	Tesla, magnetic field strength unit ($N\ s\ C^{-1}\ m^{-1}$)
TOF	time-of-flight
VH	Venezuelan heavy sour crude oil
VUV	vacuum ultraviolet

SUMMARY

This work chronicles the development of a novel desorption-ionization source coined as laser-induced acoustic desorption atmospheric pressure photoionization (LIAD-APPI) for mass spectrometry analyses. It is built on the combining technologies first developed by others (Chapter 1) combining the back-irradiated foil desorption technique, laser-induced acoustic desorption (LIAD) with a novel photoionization source known as the micro-hollow cathode discharge (MHCD) for atmospheric pressure photoionization (APPI).

Early in this work (Chapter 2), a smaller MHCD device was designed where the hydrogen Lyman-α (10.2 eV) emission line created in the discharge could be measured after exiting the device window. The combination of LIAD and this technology initially enabled fairly sensitive analysis of standard non-polar test compounds α-tocopherol and cholesterol by LIAD-APPI using dopants. In this "forward-ejected" geometry, additional successful desorption and analysis was also demonstrated for several other non-polar compounds. This configuration relied solely on the diffusion of the volatilized species and vacuum driven flow at the instrument's inlet for collection. As a disclaimer, chapter two's contributions and readings are taken as a near copy of work published in the Journal of the American Society of Mass Spectrometry (JASMS) with allowed use for thesis purposes as prescribed by JASMS author rights [1].

A subsequent iteration of this work (Chapter 3) combined a nebulizing jet for APPI dopant introduction and sample collection. This greatly decreased the time for peak collection and sensitivity of the technique. Detection limits for α-tocopherol and

cholesterol were measured in the hundreds of fmol range placing this technique on a comparable scale with similar desorption-ionization instances. These improvements enabled analyses of triacylglycerols and sterol-esters where molecular ions or quasi-molecular ions could be identified. Additionally, Chapter 3 introduces the technique's feasibility with complex mixtures such as extra-virgin olive oil. As a disclaimer, chapter three's contributions and readings are taken as a near copy of work published in the JASMS with allowed use for thesis purposes as prescribed by JASMS author rights [2].

Building upon the optimized source geometry in Chapter 3, Chapter 4 demonstrates the coupling of this source to a Fourier-transform ion-cyclotron resonance (FT-ICR) mass spectrometer for ultra-high-resolution mass spectrometry studies. Because of the applicability to low-polarity mixtures, LIAD-APPI is demonstrated as a natural method for sampling complex petroleum mixtures. These studies returned upwards of ~20,000 peaks in a single spectrum with ~1,800 identified compounds for the heavily degraded, increasingly complex petroleum mixtures studied.

This work concludes discussing the accomplishments presented and leaves the reader with some important future directions to continue improving upon this technique. Conclusively, this work serves as a linear development of a new desorption ionization technique LIAD-APPI from its inception to effective application and deployment.

CHAPTER 1. INTRODUCTION

1.1 Context and Motivation

Development of new ion source technologies have enabled some of the greatest advancements regarding chemical analysis by mass spectrometry (MS). So much of the information and its quality determined by MS is dependent on the conditions in which the analyte ions are generated. In the early forms of MS, researchers primarily relied on electron-impact (EI) ionization, a "hard-ionization" technique, occurring in high to ultra-high vacuum conditions to generate ions. This technique was particularly limited by the vacuum interface in which it must occur and the high degree of fragmentation of the molecular species of interest complicating the span of samples that could be analyzed, sample throughput, and interpretability of the resulting mass spectra. However, in 2002, Koichi Tanaka and John B. Fenn received the Nobel Prize in Chemistry for the development of matrix-assisted laser desorption/ionization (MALDI) and electrospray ionization (ESI), respectively. This was a significant moment for the field, signaling the impact that new ionization sources have had and will continue to have on expanding chemical analyses afforded by mass spectrometry. Since then, the field of atmospheric and ambient ionization techniques has provided a wealth of options for sampling and ionization, each with their own benefits and drawbacks. The ambient class of techniques arising in this field aim to provide rapid sample analysis from the surface of solid samples with little to no sample preparation. In this chapter, this work aims to introduce the technology, techniques, and prior work regarding ambient MS. Specifically, this work is

based in the current movement in the field of MS to develop increasingly more robust and rapid ambient ionization techniques for apolar molecular analytes.

1.2 Ambient and Atmospheric Ionization Sources

In the field of mass spectrometry, there are two distinct forms of high pressure ionization sources: ambient and atmospheric pressure. To avoid any confusion as one understands the context of this work, we begin by defining an ambient ionization source as any ion source aiming to sample compounds from a surface in the open environment where as atmospheric pressure ionization (API) sources, though operating at ~ 1 atm, typically sample species from a nebulized or charged spray in closed, nitrogen purged environments [3].

1.2.1 Atmospheric Pressure Ionization Sources

There are three major sources in the API category ESI, atmospheric pressure photoionization (APPI), and atmospheric pressure chemical ionization (APCI). In each of these instances, a liquid spray is driven through a nebulizer consisting of a microcapillary centred in a flow nozzle designed to generate a high velocity jet flow. The liquid flowing from the end of the capillary is thereby vaporized through this action where subsequent events lead to the ultimate ionization of the molecular entities contained therein.

1.2.1.1 Electrospray ionization (ESI)

As mentioned earlier, ESI was first developed by John B. Fenn and found itself to be a dominant technique used in a vast number of routine chemical analyses [4]. This technique is best characterized by pumping a liquid sample through a capillary needle

typically held at a potential of 1 – 5 kV. As the liquid reaches the tip of the capillary, it begins to form what is referred to as a Taylor cone due to the imbalanced charge in the liquid [5]. Because of this charged environment, desolvation of the emitted liquid is intensified due to the Coulomb repulsion between like charges in the droplets formed. The ions generated at this point are described by two theories: the ion-evaporation model (IEM) and charge residue model (CRM). IEM describes the process as a function of the droplet radius where, after the droplet radius decreases to a certain size, the electric-field becomes strong enough to eject ions contained within the droplet into the gas phase [6]. Apart from the IEM model, the CRM has been theorized as a possible pathway to ionization. In this model, droplets continue splitting into increasingly small droplets, eventually evaporating away all solvent and leaving residual charge on the remaining molecule [7, 8]. While there has been some debate which mechanism is more prevalent, it is easy to see that ESI is well suited for the analysis of *polar* molecules. As a result, it is not straightforward to analyze *apolar* molecules with ESI and ESI based techniques. Although, some have been successful using various sample additives to selectively enhance the reproducibility of detection of cholesteryl esters and glycerolipids [9, 10].

1.2.1.2 Atmospheric Pressure Chemical Ionization (APCI)

As another example of a robust spray-based API technique, APCI has been developed as an analysis tool for compounds spanning a range of polarity [11, 12]. With this technique, the liquid sample is desolvated primarily through the action of the sheath gas on the fluid emitted from the mirocapillary tip and the heating of several components in the environment. In the region between the microcapillary tip and inlet, a corona discharge is initiated by applying a several kV potential to a fine needle tip. This discharge acts to ionize

the gases in the source chamber (primarily O_2 and N_2) creating anionic or cationic charged intermediates. These subsequently ionize compounds of interest M, through several pathways in positive mode shown in Equations 1-8 [11, 13].

$$N_2 + e^- \rightarrow N_2^+ + 2e^- \quad (1)$$

$$N_2^+ + 2N_2 \rightarrow N_4^+ + N_2 \quad (2)$$

$$N_4^+ + H_2O \rightarrow H_2O^+ + 2N_2 \quad (3)$$

$$H_2O^+ + H_2O \rightarrow H_3O^+ + OH^{\cdot} \quad (4)$$

$$H_3O^+ + H_2O + N_2 \rightarrow H^+(H_2O)_2 + N_2 \quad (5)$$

$$H^+(H_2O)_{n-1} + H_2O + N_2 \rightarrow H^+(H_2O)_n + N_2 \quad (6)$$

$$H^+(H_2O)_n + M \rightarrow MH^+(H_2O)_m + (n-m)H_2O \quad (7)$$

$$MH^+(H_2O)_m \rightarrow MH^+ + mH_2O \quad (8)$$

However, because of the high internal energy of the charged intermediate species (e.g. N_2 IP 15.58 eV) and typically high temperatures required for desolvation, this technique tends to be more energetic than other API sources [14]. The consequences being fragmentation of more labile molecules as well as complicating the spectrum through ionization of the solvent.

1.2.1.3 Atmospheric Pressure Photoionization (APPI)

As an alternative to APCI, APPI is also useful for the ionization of apolar species eluted in liquid form from a nebulizing needle. In this technique, a radio-frequency excited gas contained within a glass lamp emits vacuum ultraviolet (VUV) light which acts to photoionize atmospheric additives called dopants [15]. These photoionized intermediates can interact with the gas-phase molecules generated by the nebulizing spray to ultimately ionize the analytes of interest through processes shown in equations 9-13 for positive mode [16].

$$D + h\nu(> 10\ eV) \rightarrow D^{+\cdot} + e^{-} \quad (9)$$

$$D^{+\cdot} + M \rightarrow M^{+\cdot} + D\ if\ IP(M) < IP(D) \quad (10)$$

$$D^{+\cdot} + M \rightarrow [D - H]^{\cdot} + MH^{+}\ if\ PA(M) > PA([D - H]^{\cdot}) \quad (11)$$

$$D^{+\cdot} + nS \rightarrow [D - H]^{\cdot} + S_nH^{+}\ if\ PA(S_n) > PA([D - H]^{\cdot}) \quad (12)$$

$$S_nH^{+} + M \rightarrow MH^{+} + nS\ if\ PA(M) > PA(S_n) \quad (13)$$

Where IP and PA are the ionization potential and proton affinity, respectively, and D, M, and S are the dopant, analyte, and solvent molecules. For negative mode, equations 14-18 describe the primary ionization mechanism adapted from Kauppila et al. [17].

$$O_2 + e^{-} \rightarrow O_2^{-\cdot} \quad (14)$$

$$M + e^{-} \rightarrow M^{-\cdot}\ if\ EA(M) > 0\ eV \quad (15)$$

$$M + O_2^{-\cdot} \rightarrow M^{-\cdot} + O_2\ if\ EA(M) > EA(O_2) \quad (16)$$

$$M + O_2^{-\cdot} \rightarrow [M - H + O]^{-} + OH^{\cdot} \quad (17)$$

$$M^{-\cdot} + O_2 \rightarrow [M - H + O]^- + OH^{\cdot} \quad (18)$$

$$M + O_2^{-\cdot} \rightarrow [M - H]^- + HO_2^{\cdot} \; if \; \Delta G_{acid}(M) < \Delta G_{acid}(HO_2^{\cdot}) \quad (19)$$

$$M + [S - H]^- \rightarrow [M - H]^- + S \; if \; \Delta G_{acid}(M) < \Delta G_{acid}(S) \quad (20)$$

Where EA is the electron affinity and ΔG_{acid} is the gas phase acidity. Special note should be taken of equation 11, demonstrating the charge transfer ionization pathway which makes APPI so effective for ionization of low to non-polar analytes which do not readily protonate or form negative ions.

Because the VUV photon energy of these lamps is in practice usually no higher than 10.64 eV (Krypton), this process excludes most liquid chromatography (LC) solvents from being ionized [15, 18]. In effect this simplifies the spectrum, though it is noted that post-ionization reactions can lead to further complexity. Nevertheless, APPI has been adopted as a standard API technique and can be found as a component for nearly all commercial instruments.

Multiple studies have sought to address the parameter space of this technique with regards to the lamps and dopants used for APPI-MS analysis [16, 19, 20]. Traditional lamps for APPI have included argon, krypton, and xenon with the majority of studies being conducted with krypton lamps (hν = 10.03 eV, 10.64 eV) [18]. These lamps typically operate on rf power sources and are comprised of a sealed glass tube and two electrodes. These lamp assemblies are widely available and quick to implement in a laboratory setting, running on rf power supplies typically 28 W or greater. The primary drawback of this

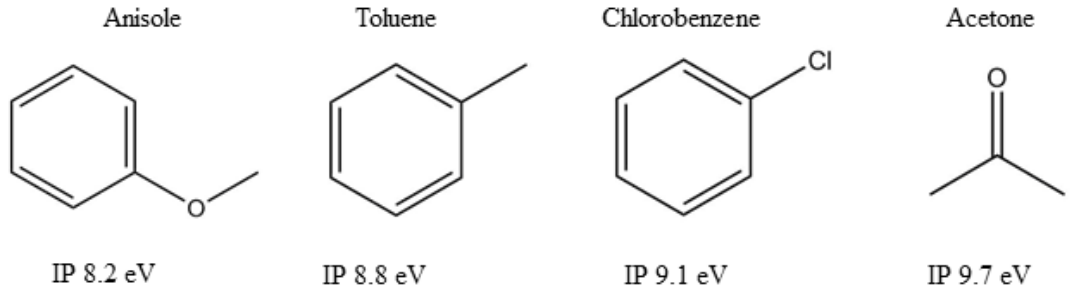

Figure 1-1: Common APPI dopants and their ionization potentials.

instrumentation is the need for an assortment of lamps if alternative photo-emission is desired.

The use of dopants has been seen as critical for APPI since its inception [15]. Need for this parameter is given by the fact that the likelihood of ionization of some analyte, low in concentration relative to the solvent, is low due to photon absorption by the solvent. By adding a dopant, this raises the fraction of ionizable molecules in the sample greatly and, due to the high collision rate at atmospheric pressure, acts to ionize the molecular analytes of interest. Some of the most widely studied dopants and their ionization potentials (IPs) can be seen in Figure 1.1. Again, a key benefit here being that the available energy of the dopant photoion is not great enough to ionize the solvent or atmospheric gases while still being high enough to ionize potential target molecules. Effects of the different dopants on the resulting spectrum can vary depending on the chemical nature of the sample and the ionization potential of the dopant. Itoh et al. aimed to investigate the efficacy of different dopants for APPI and found that a 0.5/99.5 vol/vol mixture of anisole and toluene was ideal for analysis of a mixture of polyaromatic hydrocarbons (PAHs) [21].

Chemistries explored with APPI have included sterol analysis in plasma, environmental sampling, petroleomics, and many more [22-24]. The technique has found a defining use as an apolar analysis tool although, it still is capable of ionizing polar compounds. While there have been great successes with APPI, this technique still suffers from the need for a liquid sample that can be volatilized creating a need for careful and sometimes lengthy sample preparation protocols. This difficulty is not limited to APPI and is a large driver for creating the next class of sources we will discuss.

1.2.2 Ambient Ionization Sources

The field of ambient ionization sources has gathered an extensive array of techniques, many of which are unique. As a reminder, these techniques are characterized as any technique aiming to sample and ionize material from a solid surface in the open environment, outside of any chamber or enclosure [3]. The sampling is typically accomplished through the use of laser, thermal, nebulized solvent, or electrospray desorption mechanisms and either through a part of that process or a sequential distinct technique, the sampled gas phase species are ionized [25-29]. In essence, ambient MS generally aims to provide a platform requiring minimal to no sample preparation and a means for quickly switching between samples. Though the literature has become abundant with many one-of-a-kind instances of ambient ionization sources just 5 years after the first demonstrations, the discussion here will be limited to a few of the most prominent and pertinent to the field and this work [30].

1.2.2.1 Desorption electrospray ionization (DESI)

As one of the first examples of ambient ionization sources, desorption electrospray ionization (DESI) has made its impact on a variety of fields including protein/lipid imaging in brain tissues, metabolite profiling, and even machine learning enabled forensic science [31-33]. The technique is thought to desorb species on an arbitrary surface by via a "droplet pick-up" model in which the charged aerosol droplets from the electrospray directed at the surface capture analytes and lift them into the gas phase [34]. The subsequent ionization process is effectively the same as ESI. Therefore, this technique is exceptionally suited for polar analytes.

1.2.2.2 Direct Analysis in Real Time (DART)

Not long after the demonstration of DESI, the first direct analysis in real time (DART) paper was presented in 2005 [26, 28]. Though the coined name DART is attractive, it detracts from any information on how the source mechanistically functions. Notably, this is a plasma-based chemical ionization technique which typically directs helium metastables ($He(2^3S)$ or $He(2^1S)$, IE 19.8 eV, 20.0 eV) via a heated gas jet onto a sample positioned in front of the inlet acting to thermally desorb species on the sample surface (Note that we will denote the helium metastable as He* henceforth). Ionization of those species typically takes place as protonation reactions in the gas phase due to the abundance of protonated water clusters formed through a chain reaction initiated by ionization of N_2 by He^* in a similar manner to equations 2-8. However, depending on the environment and source variables some pathways may prevail over others. Because this technique was solvent-free, the large electronic energy of the metastables formed does not lead to a large background signal. However, it is possible for DART to induce

fragmentation of analyte species through more energetic Penning ionization (equation 21) or the higher heat of the thermal gas jet.

$$He^* + M \rightarrow He + M^{+\cdot} + e^- \quad (21)$$

Regardless, the robustness of a technique based on metastable formation did not go unnoticed. This brought forth a boom in plasma-based ionization source research including flowing atmospheric pressure afterglow (FAPA), plasma assisted desorption/ionization (PADI), low-temperature plasma (LTP) ionization, and novel microplasma discharge ionization techniques [29, 35-37]. Each of these examples provided unique instances of applying plasmas to ambient ionization MS and are a significant basis for the foundations of this work and use of atmospheric pressure discharges.

1.2.2.3 Desorption atmospheric pressure photoionization (DAPPI)

Leaving the realm of relatively high energy species, photoionization was brought to the forefront of ambient MS through the demonstration of desorption atmospheric pressure photoionization (DAPPI) [27]. In this technique, a heated microchip nebulizing jet containing the atmospheric dopant is directed at the sample surface at ~45° angle. The heated spray jet acts to thermally desorb molecules on the surface. In the gas phase, ionization occurs through the ion-molecule reaction pathways described for APPI and shown in equations 9-18. This technique has been shown to be useful for a variety of applications including rapid lipid and pharmaceutical screening, food analysis, mass spectrometry imaging (MSI), and explosives screening. [38-41]. Recalling from the discussion on APPI, it is well known that the ionization pathways for DAPPI are useful for apolar and polar analytes. However, when it comes to larger, more labile species, Suni et

al. noted for phospho- and sphingolipids, higher temperature thermal jets were required to desorb these from the surface [42]. Consequently, a relatively high degree of fragmentation is observed in the resulting spectrum, thus limiting the technique with respect to these classes of molecules.

1.2.2.4 Laser desorption/ionization and laser desorption post-ionization techniques

Differing from the desorption mechanisms discussed thus far, a swath of the ambient ionization literature is filled with techniques using high-powered lasers to ablate, desorb, or sometimes also ionize the species on the surface in question. One such example includes laser ablation atmospheric pressure photoionization (LAAPPI). In the work of Vaikkinen et al., it was demonstrated that molecular and fragment specific peaks could be seen for compounds weighing less than 500 amu and provided a complimentary mass spectrum of sampled rat brain tissue to another laser based technique, laser ablation electrospray ionization (LAESI) [25, 43]. Both techniques took advantage of the high absorption of the mid-infrared (2940 nm) laser by the water-rich biological samples to efficiently desorb the species contained therein. Though this provided an excellent result for these samples, this can be seen as a method requiring a water matrix thus not applicable to non-biological or dehydrated samples.

Of particular interest to this work are the instances of ambient sources combining laser-induced acoustic desorption (LIAD) with a secondary ionization technique. One of the most successful, LIAD/APCI, has been demonstrated for PAHs and saturated hydrocarbons [44-47]. Nonetheless robust, LIAD/APCI was found to produce a high relative deprotonated molecular ion abundance for high flow rates of O_2 carrier gas. This

depleted the formation of protonated water clusters, enabling an enhanced degree of ionization for the non-polar compounds studied [47]. In addition, LIAD has also been coupled with ESI to provide an ambient solution to larger, biological compounds including albumin, hemoglobin, and α-casein [48]. Though LIAD was a novel improvement, this technique is still best applied to more polar samples due to the inherent mechanisms associated with ESI. In each of these instances, LIAD was a key development allowing ease of sample preparation and a widely effective desorption response. Thus, there is a great interest in understanding this technique and the extents to which it can be applied.

1.3 Technologies of LIAD-APPI

1.3.1 LIAD

To clarify the discussion, LIAD as it is related to this field typically refers to back-irradiating 5 – 20 μm foils with short ns laser pulses focused to a power density of 10^8-10^9 W cm^{-2} thereby desorbing the species deposited on the opposing side (Figure 1.2).

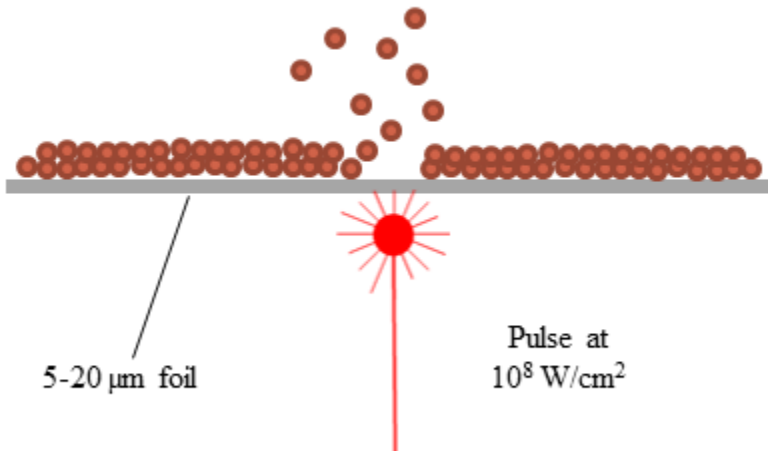

Figure 1-2: LIAD schematic illustrating molecular species (red-orange circles) being desorbed from an area opposite of the side of the laser strike.

Before too much meaning is attributed to the name LIAD, we must first note that this is a known misnomer. Lindner and Seydel first reported the phenomenon after back-irradiating a 1 - 20 μm thick solid samples containing a mix of sugars and NaI on copper support grids with a laser of power density 10^{11} W cm^{-2} [49]. Their results demonstrated effective detection of sodiated molecular ions in an intact form for samples without perforation of the laser pulse. Without much evidence, they postulated that the underlying mechanism was related to the laser-driven shock wave propagating through the material effectively "shaking-off" the species contained. The results went largely unnoticed until Golovlev et al. reported negative hydrogen ions and electrons being emitted from foil surfaces [50]. These studies appeared to support the acoustic shock-wave theory albeit with a curious sample construction of a 300 nm thick metal coating on a sapphire cell encapsulating a 750 μm thick mercury layer. Nevertheless, this study coined the term, LIAD. After interest and use of the technique began to rise, the work of Zinovev et al. sought to elucidate the true mechanism of typical LIAD implementations consisting of an organic layer adsorbed onto one side of a thin metal foil [51]. Their reasoning provided a simple kinetic energy relation (Equation 22).

$$v \geq \sqrt{2E_b/m} \tag{22}$$

This revealed that the estimated foil displacement velocities (v) required for desorption are in the range of 100-500 m/s in order to break the binding energy ($E_b = 0.05 - 0.5$ eV) of most adsorbed small molecules with mass, m [52]. This was in direct contrast to observed measurements of foil displacement velocities measured at a few meters per second [53].

Hence the reported acoustic “shake-off” mechanism is very unlikely to cause molecular desorption. Ref. [51] then postulates that the true causal mechanism of LIAD most likely arises from thermal and mechanical stresses due to mismatch of the analyte films adsorbed on foil. Later works clarify this hypothesis by noting that most foil-adsorbed analyte species consisting of at least a few layers of material are not in a minimal energy state and in fact have some residual stress associated with their adsorbed state [54]. Upon back-irradiation by the laser pulse, the generated acoustic/thermal field distorts the opposite foil surface causing cracking and delamination of the analyte film thereby leading to repulsive and excited electronic states for desorption [55, 56]. This is supported by the observation that there is a nonlinear desorption yield dependence on laser intensity and an independence of desorbate velocity on driving laser intensity as reported by Zinovev et al [55].

To be sure, the previous work on LIAD does not explore the physical scenarios where there is only a sparse amount (e.g. sub-monolayer coverage) of analyte on foil and the precise foil surface-molecule interaction that would occur. In this scenario, there is no analyte film and associated stress therein, yet desorption for these scenarios would be expected given the emission of ions and electrons from foils [50]. Future studies involving specialized spectroscopy and ultra-high vacuum (UHV) experiments would need to be conducted to truly gain insight into the dynamics of desorption in this regime.

While the exact mechanism and scenarios constituting LIAD are not well defined, the field of mass spectrometry has nonetheless utilized LIAD as a viable desorption technique. One of the first instances characterizing LIAD was demonstrated in Pérez et al. under vacuum conditions with EI and chemical ionization (CI) [57]. Their results gave the very powerful conclusion that LIAD could be used to successfully volatilize a range of

intact, thermally labile molecules deposited on thin foils. Subsequently, a flurry of interest spread across the analytical community demonstrating LIAD to be useful for larger hydrocarbons, bioparticles, petroleum distillates, biological cells, and many other applications [58-61]. These early indications demonstrated LIAD to be a notably versatile technique allowing for desorption of any mass or class of molecule or particle imparting a minimal amount of energy in the process.

1.3.2 Plasma fundamentals and microplasmas

In addition to this work characterizing the first ambient implementation of LIAD-APPI, it also employs a unique photoionization tool known as the micro-hollow cathode discharge (MHCD). These devices boast many important benefits. Though to understand them, we must first understand the underlying fundamentals of plasmas and microplasmas.

1.3.2.1 Direct Current (DC) Plasmas and Electrical Breakdown

A plasma is best defined as a state of matter in which a gaseous substance is ionized becoming electrically conductive so that electric and magnetic fields dominate the behaviour of the system [62]. This definition encompasses a range of physical systems so to clarify the discussion relevant to this work, we will consider a plasma system consisting of two electrodes in a gaseous environment at low to moderate (~ 760 torr) pressures.

Before a plasma can exist, it must first be initiated by some electric field generated by the electrodes. Upon introducing the electric field, the trace amounts of background ions

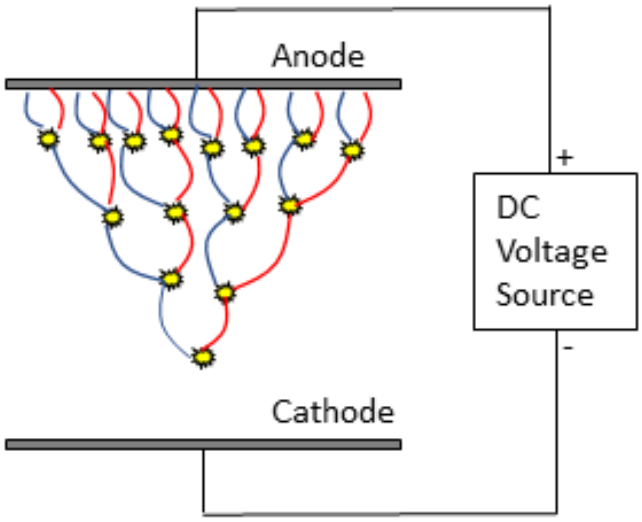

Figure 1-3: Visualization of a Townsend avalanche. Blue lines indicate path of incident electron where as red lines indicate path of the liberated electron. The yellow stars indicate the ionization event itself.

and electrons are accelerated, ionize other neutral species, and generate additional charged species to continue the process given a high enough field strength [63]. This electrical breakdown process is known as the Townsend avalanche/discharge and is displayed in Figure 1.3 for illustration. However, the Townsend discharge is generally known as a dark discharge leading up to the breakdown point at which the glow discharge is formed. The breakdown point or voltage is considered to be the point at which electrons are being produced faster than they are lost due to attachment and recombination. This process was first described empirically by Freidrich Paschen who provided a very useful formula for determining breakdown voltage shown in equation 23 [64].

$$V_b = \frac{bpd}{\ln(apd) - \ln(\ln(1 + 1/\gamma)} \tag{23}$$

Where a and b are empirical constants, γ is the secondary emission coefficient which depends on cathode material, p pressure, and d is distance. The resulting plot is shown to

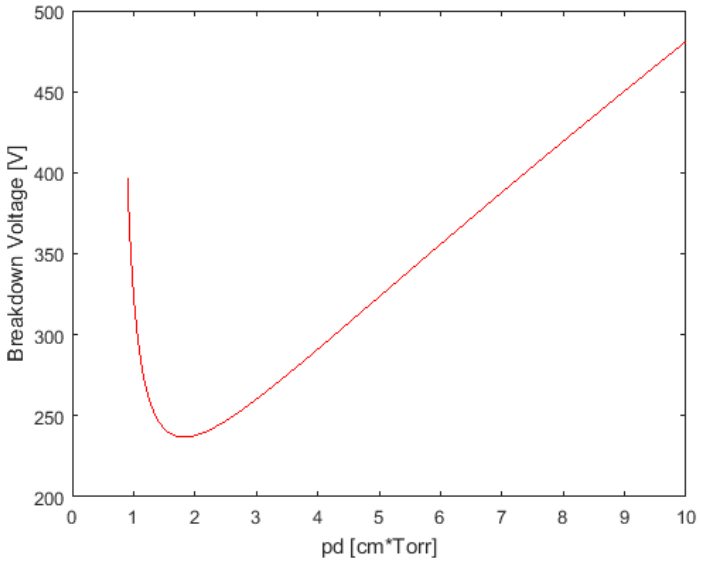

Figure 1-4: Paschen curve for Neon gas. Where b = 130 V cm^{-1} Torr^{-1}, a = 1.84 cm^{-1} Torr^{-1}, and γ = 0.8

be a function of pd and is expressed in cm Torr is shown in Figure 1.4 for neon gas. Note, that if the pressure is held constant and the electrode distance is varied, one can easily construct a device to operate at the minimum of this curve and minimize the voltage required for plasma ignition. This is the one the main benefits of microplasma devices. In fact, others who have studied microplasmas at atmospheric pressures have found significant deviations from Paschen's law for electrode distances at 1-10 μm [65]. Previous findings indicated that at small electrode gaps at atmospheric pressure, the charge density becomes so great that it distorts the electric field. This lowers the barrier for electron emission from the cathode, increasing the charges accelerated by the applied electric field, and thus creating the observed deviation in breakdown voltage from Paschen's law [66].

Peculiarities like these, among the benefits of being small, compact, and versatile devices, are primary drivers for the significant amount of interest in microplasmas [67].

1.3.2.2 Into the Glow

The plasma devices most useful to this work operate in what is known as the glow discharge regime under the general current voltage relationship provided in Figure 1.5 (adapted from [68]). This describes the entire process leading up to thermal arcing starting

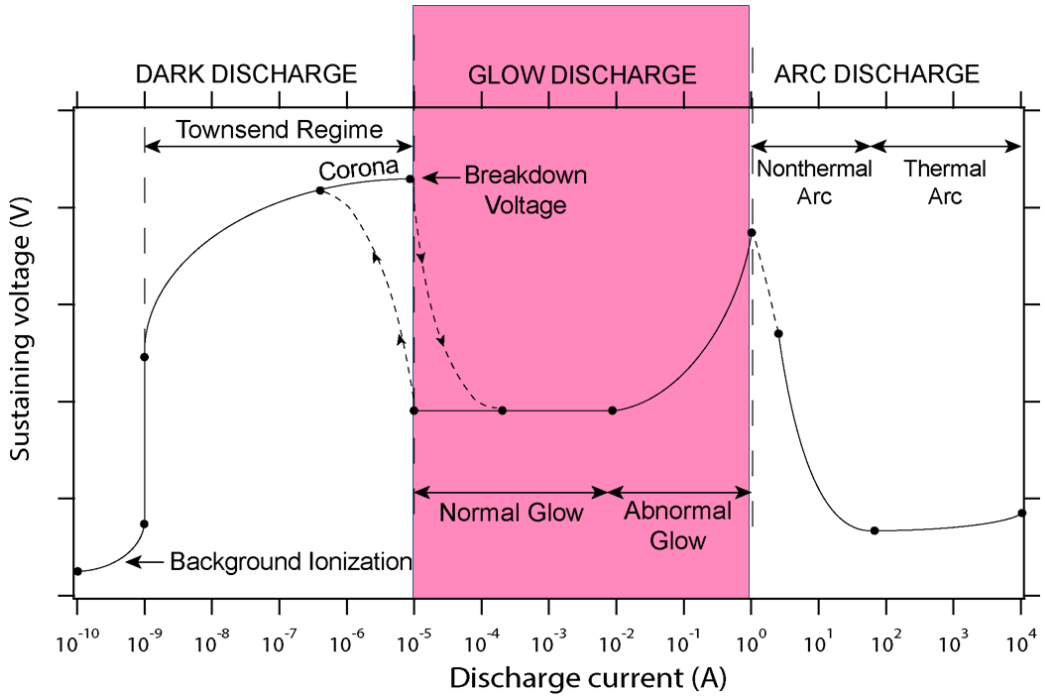

Figure 1-5: A generalized plot of current vs. voltage across multiple plasma regimes. Pink box indicates the glow discharge regime important to this work.

from very small currents with high sustaining voltages. In the "dark" discharge regime, the voltage asymptotically approaches the breakdown voltage described earlier upon which the plasma transitions to the glow discharge, named because of the visible glow typically observed from plasmas in this state. Because of the energetic environment and the excited

states of the species therein, the dynamics of the species in the glow lead to a high rate of photo emission making this state of plasma an efficient photon emitter. However, the type of photoemission obtained from this plasma state can vary depending on gas composition, current-voltage regime, and gas transport properties. Therefore, it is important to understand which devices generate a desirable plasma environment and how to optimize those devices for the desired task.

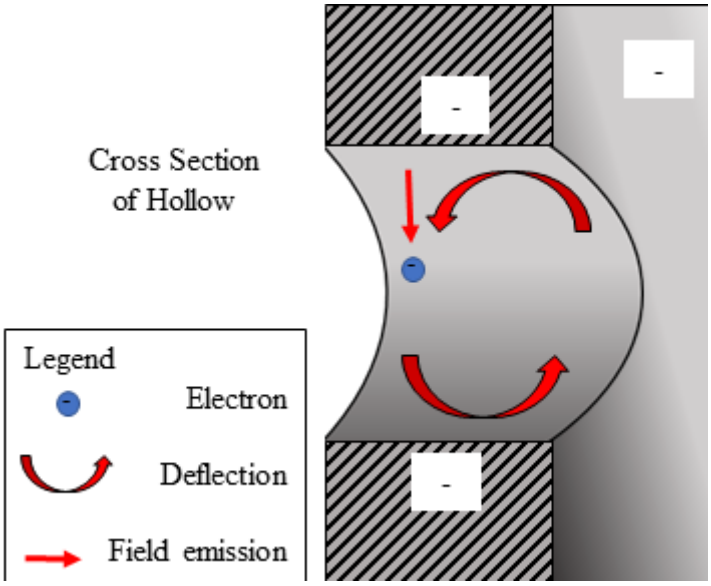

Figure 1-6: Schematic illustrating the Pendel Effect in a hollow cathode discharge device. The cathode is the only electrode shown for this figure.

1.3.2.3 Micro-hollow cathode discharges (MHCDs)

Without excessive motivation, we will turn our attention to the micro-hollow cathode discharge (MHCD). These devices are characterized by the hole or hollow fabricated in the cathode material. This geometry creates an interesting phenomenon known as the Pendel effect shown in Figure 1.6. Because of the negative potential of the

cathode, electrons in the plasma oscillate in the hollow of the cathode generating multiple collisions with other species in the system [69]. Thus, this leads to a more efficient generation of excited species and a range of utilizable photoemissions. Particularly, excimers or excited dimer species forming in MHCDs were first reported by Schoenbach et al. who observed excimer VUV photoemission at high pressures (760 Torr) of argon and later xenon [70, 71]. It is well known that in nearly all discharges, excimers are formed via a three-body collision process, thus producing the pressure dependence observed by Schoenbach et al. This process is described by equation 24 for a general gaseous species X with its respective metastable species denoted X^* [71].

$$X^* + X + X \rightarrow X_2^* + X \tag{24}$$

Furthermore, table 1.1 is provided illustrating the different excimer VUV emissions that are expected for pure rare gases typically used for MHCDs. It is expected that for a MHCD in a pure environment of these gases, that these emissions would be observed efficiently at higher pressures. However, given a mixture of these or other gases, it is likely that these emissions would not be observed owing to the collisional quenching of the excimer state. As a pertinent example to this work, previous studies observed hydrogen Lyman-α emission from a neon hydrogen mixture with MHCDs. From their observations it was concluded that the near-resonant collisional energy transfer of the neon excimer with H_2 leads to the hydrogen Lyman-α emission observed. This process is illustrated by equations 25-27.

$$Ne^* + Ne + Ne \rightarrow Ne_2^* + Ne \quad (25)$$

$$Ne_2^* + H_2 \rightarrow 2Ne + H + H^*(n = 2) \quad (26)$$

$$H^*(n = 2) \rightarrow H(n = 1) + h\nu(121.6\, nm) \quad (27)$$

Accounting for the dissociation energy of the H_2 molecule at 4.48 eV, the transition energy of the Lyman-α line at 10.2 eV, and the available energy of a decaying Ne_2^* molecule at 14.8 eV, the process is observed to be near-resonant supported by the observed efficient formation of the Lyman-α emission [72, 73]. This is a particularly important finding for this work as this is the primary means of VUV generation employed for LIAD-APPI.

Table 1-1: Common excimer emissions from rare gases [74].

Rare Gas	Peak λ (nm)	Energy (eV)
He	75	16.5
Ne	84	14.8
Ar	130	9.54
Kr	145	8.55
Xe	170	7.29

In addition to the efficient excimer formation expected from MHCDs in static gas environments, there has also been the added benefit of using flow to introduce the gas in the hollow of the discharge. This has been shown to be an effective method for reducing impurities in the plasma gas (namely oxygen) and to enhance the VUV flux emitted [75]. By reducing oxygen impurities, the lifetimes of these devices can be increased by limiting oxidation of the electrodes which are typically fabricated from molybdenum.

1.4 Summary

When this work began, techniques like DAPPI, DART and DESI had already been well characterized and the newer atmospheric and ambient implementations were illustrating success. In addition, MHCDs had recently been demonstrated to offer photoionization capabilities in an ambient setting for some small molecules. Therefore, this work found a natural marriage of the components described in the subsequent chapters. The rest of this thesis will focus on a first implementation, an optimized implementation, and the application of the LIAD-APPI source to crude oil analysis, some of the most complex chemical mixtures known.

CHAPTER 2. LASER-INDUCED ACOUSTIC DESORPTION ATMOSPHERIC PRESSURE PHOTOIONIZATION VIA VUV-GENERATING MICROPLASMAS

We demonstrate the first application of laser-induced acoustic desorption (LIAD) and atmospheric pressure photoionization (APPI) as a mass spectrometric method for detecting low-polarity organics. This was accomplished using a Lyman-α (10.2 eV) photon generating microhollow cathode discharge (MHCD) microplasma photon source in conjunction with the addition of a gas-phase molecular dopant. This combination provided a soft desorption and a relatively soft ionization technique. Selected compounds analyzed include α-tocopherol, perylene, cholesterol, phenanthrene, phylloquinone, and squalene. Detectable surface concentrations as low as a few pmol per spot sampled were achievable using test molecules. The combination of LIAD and APPI provided a soft desorption and ionization technique that can allow detection of labile, low-polarity, structurally complexmolecules over a widemass range with minimal fragmentation.

2.1 Introduction

Over time, the field of mass spectrometry (MS) has expanded in scope due to the introduction of a variety of ion generation methods that extend the range of systems that can be probed. Of particular interest is the development of various MS techniques that are suitable to analyze minute amounts of analytes deposited on surfaces, each having different drawbacks and advantages.[76] Non-polar molecules have, thus far, been difficult to

analyze by surface MS techniques due to both the inherent ionization mechanisms and amount of energy imparted to the molecules during the desorption/ionization events. Due to their low proton affinities, these compounds do not protonate easily, and are not detected with high sensitivity using techniques such as desorption electrospray ionization (DESI) or matrix-assisted desorption ionization (MALDI). As a consequence, alternative surface analysis techniques that focus on photoionization of neutral desorbates have been developed including desorption atmospheric pressure photoionization (DAPPI) and laser ablation/desorption photoionization.[25, 77, 78] With DAPPI, a heated solvent jet desorbs analytes from a surface which undergo atmospheric pressure photoionization (APPI) initiated by a radiofrequency driven vacuum ultraviolet radiation emitting (RF VUV) lamp and then swept into the atmospheric pressure inlet of a mass spectrometer. Despite its appealing coverage in terms of analyte polarity, studies have suggested DAPPI may not be best suited for labile high molecular weight compounds due to the relatively large amount of heat required to desorb larger molecules, and the subsequent fragmentation.[42] As for methods involving direct (without matrix) laser ablation/desorption, these are also known to produce fragmented gas phase molecules due to direct irradiation from the desorption laser as well as above plume/plasma interactions. Direct laser ablation/desorption is also often limited to lower molecular weight desorbates.[79]

Laser-induced acoustic desorption (LIAD) is capable of desorbing analytes in a wide range of molecular weights and has therefore received significant recent attention. [50, 80-82]LIAD is accomplished by irradiating the backside of a metal foil ~ 5-20 μm thick with a nanosecond laser pulse of power density ~ 10^8 W/cm^2. After absorption of this pulse, molecular species are ejected from the opposite side of the foil with relatively little

energy transferred to the desorbed species.[57, 83] Since LIAD is known to generate mostly neutral and intact molecules, this technique is well suited for softly producing pulses of low-polarity thermally-labile gas-phase molecules.[57, 84, 85] Initial studies describing the LIAD process suggested an acoustic wave mechanism for volatilization.[86] However, subsequent studies suggest a more complex mechanism where laser induced stresses in the foil cause cracks in deposited molecular crystals and repulsive non-equilibrium electronic surface states thus creating desorption sites from which analytes are ejected.[56, 83] Though now considered to be misleading, we continue to use the term LIAD here due to familiarity. Applications of LIAD to ambient mass spectrometry surface analysis scenarios demonstrated its viability for desorption of various organic compounds in a mass range extending up to m/z 762 using atmospheric pressure chemical ionization (APCI) as the tool for ion generation.[87]

Recent developments in microplasma ion sources for ambient/atmospheric MS have demonstrated their viability as vacuum ultraviolet (VUV) sources for APPI techniques.[88] This specific class of plasma device, the micro-hollow cathode discharge (MHCD), is characterized by a small hollow in the cathode of the device in which Pendel electrons experience multiple collisions with the plasma gas.[69] For a neon:hydrogen admixture discharge gas, these interactions are known to produce neon excimers that through near-resonant energy transfer dissociate H_2 leading to Lyman-α (10.2 eV) photon emission.[73] The emission spectra from these devices are also known to be dependent upon the discharge gas composition, flow rates and discharge current/voltage.[74, 75, 88]

In this work, the generation of VUV light and the potential utility of MHCDs as miniature, low power consumption, atmospheric pressure photoionization sources for

applications in surface desorption measurements is demonstrated. Specifically, we report the first combination of LIAD and APPI for the analysis of low-polarity compounds deposited on titanium foil. This combination utilizes a MHCD with a LiF exit window that seals the plasma cavity, blocks the emission and release of reactive plasma species, and allows the transmission of VUV to mid-infrared photons. This LIAD-APPI approach provides the ability to detect picomols of nonpolar substances on a foil surface, and is expected to be general and particularly applicable for larger molecules that are prone to unimolecular decay and fragmentation if desorbed by other means.

2.2 **Experimental**

2.2.1 Materials, Chemicals, and Sample Preparation

12.7 µm thick titanium foil (99.8% metals basis) for the LIAD experiments was purchased from Alfa Aesar (Ward Hill, MA, USA). The low-polarity compounds studied (α-tocopherol, perylene, cholesterol, phenanthrene, -phylloquinone, and squalene), solvents (toluene, hexane, ethanol, dichloromethane) and molybdenum foil (100 µm thick) for the plasma device electrodes were purchased from Sigma Aldrich (St. Louis, MO, USA). The LiF window used in the MHCD device (10 mm diameter, 1mm thick) was purchased from Crystran (Poole, Dorset, UK). Samples were deposited on the 12.7 µm Ti foil using the iMatrixSpray open source deposition system (Grubenacker, Switzerland). Solutions ranging from 10mM - 1µM were deposited by the iMatrixSpray system through ten coating cycles which leads to a pixel to pixel coefficient of variance of 7% or less.[89]

2.2.2 Microplasma Device

The device developed for these experiments is a custom-built MHCD designed with a LiF window to ensure VUV photon transmission. The particular device used in this work (Figure 2.1) is an improved and miniaturized iteration of a previous device described in ref. [88]. Device diameter was scaled down by 35% and total volume was scaled down by 86% to ensure closer proximity of the MHCD output to the laser desorption/ionization region (Figure 2.2). As shown in Figure 1.1, the MHCD cathode and anode electrodes were separated by 100 μm thick mica as a dielectric and holes through the electrodes and mica spacer were fabricated between 100–200 μm in diameter by either mechanical drilling or electrical discharge machining. A ballast resistor (R = 97 kΩ) was used to limit the discharge current (Figure 2.1(b)).

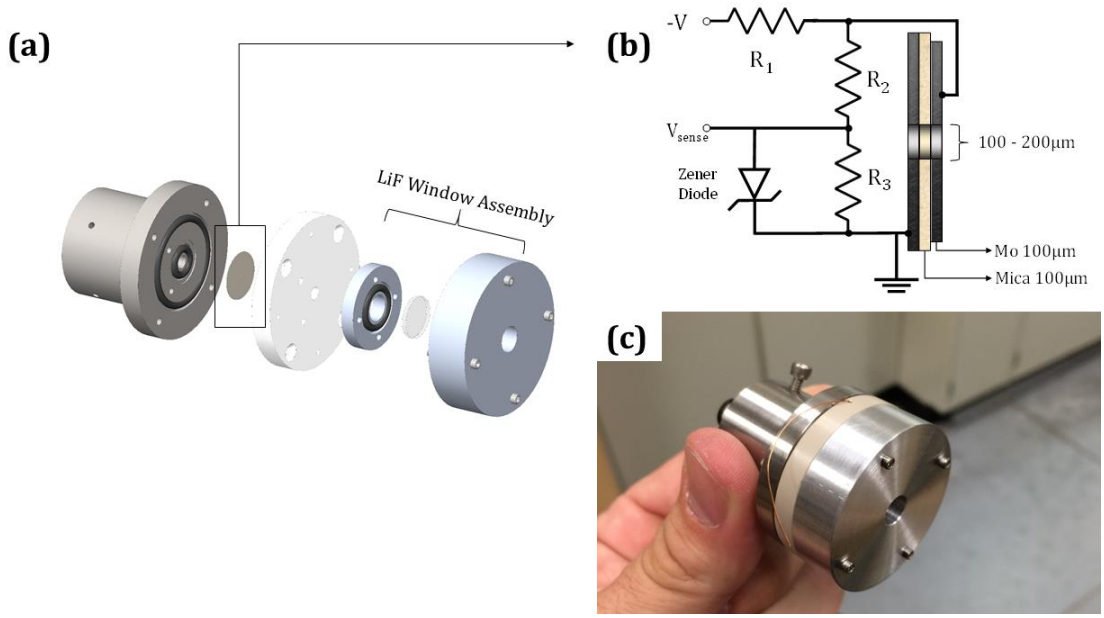

Figure 2-1: (a) Exploded view of the 3D model of the microplasma VUV device. (b) Circuit diagram with including ballast resistor (R_1 = 97 kΩ) and voltage divider used for observing the discharge potential (R_2 = 21 MΩ, R_3 = 560 kΩ). (c) Picture of the device taken following fabrication.

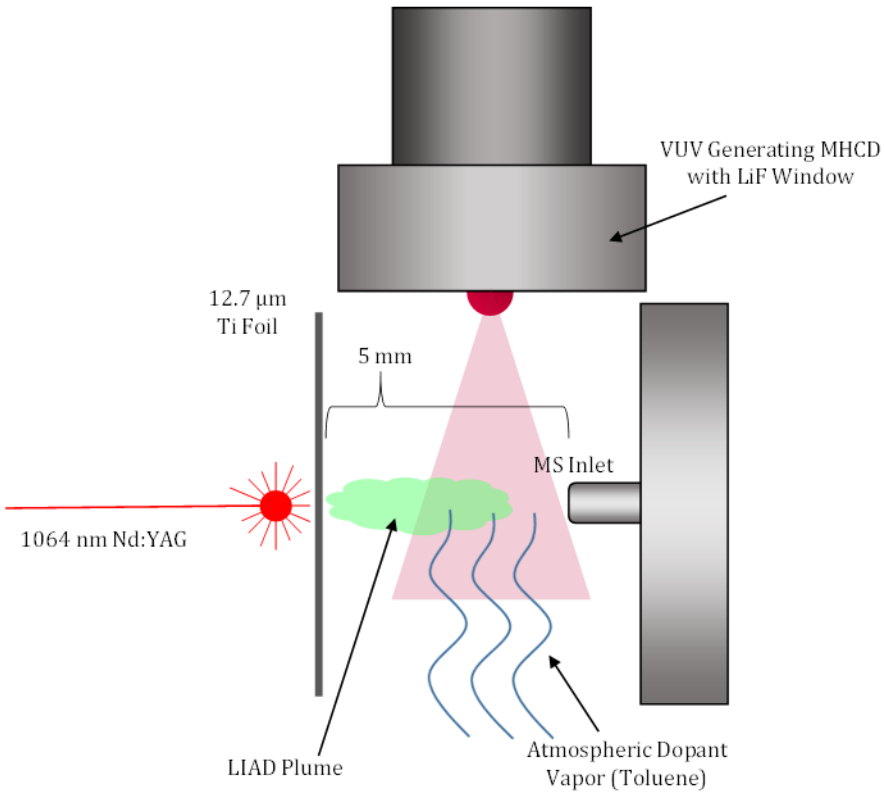

Figure 2-2: Schematic of the LIAD APPI ion source assembly including a VUV-generating MHCD illustrating the process of desorbing molecules via LIAD, transferring them to the region containing reactive dopant photoions, and transfer into the mass spectrometer.

2.2.3 Microplasma Operation

Lyman-α (10.2 eV) light generation was accomplished by operating the MHCD with the admixtures of 3-7% hydrogen in neon as previously reported in similar devices.[88] For all mass spectrometry experiments, unless otherwise noted, a nitrogen purge in the device cavity (2 SLM) was allowed to run for 10 minutes, and shut off before plasma ignition. The plasma gas mixture of 4% H_2 in Ne then flowed through the device at 40 sccm to enhance excimer formation and thus VUV emission.[75] Current delivered to the device was limited between 10 – 11 mA by the Stanford Research Systems model

PS350 power supply (Sunnyvale, CA, USA). The corresponding applied voltages ranged between 1100 – 1200 V. Flow rates were controlled by two FMA-5500 series mass flow controllers (MFCs) from Omega Engineering (Stamford, CT, USA). For VUV energy-resolved spectroscopy experiments, the MHCD cavity was purged with argon and a 7% H_2 in Ne plasma gas flowed into the device at 70 sccm, while the current was varied between 5 – 10 mA. Though the VUV emission and LIAD-APPI experiments were carried out under slightly different relative gas mixing ratios, the emission is not expected to vary drastically especially under constant current/discharge conditions.

2.2.4 VUV Monochromator Instrumentation

Measurements of the Lyman-α output of the device were made using a 0.2 mVUV monochromator (Acton VM-502) equipped with a sodium salicylate scintillator and PMT detector at the Cryogenic Chemistry Laboratory at NASA's Jet Propulsion Laboratory (Pasadena, CA, USA). Calibration of the instrument was accomplished using a Hg lamp and tuning of the Lyman-α line resolution was performed with a RF argon/hydrogen lamp. Using the emission lines of Hg at 253.7 nm and 184.5 nm a resolution of 5 Å could be estimated. For measurements on the plasma device, the spectrometer was operated at low vacuum (0.1 torr) and the device was sealed to the monochromator inlet by Apiezon putty. This was done to reduce further attenuation of the Lyman-α emission intensity by windows external to the device.

2.2.5 LIAD-APPI Setup

The LIAD substrate foils were secured tightly over a metal tube to ensure a flat foil surface and placed at a fixed position 5 mm from the inlet of a Bruker micrOTOF-Q II

mass spectrometer (Bruker, Billerica, MA). The instrument was operated in positive mode in the range of 50 to 1000 m/z with the following settings: +50 V capillary bias, -50 V end plate offset, 3.0-4.0 L min^{-1} N_2 dry gas at 34 °C, 3.3 mbar foreline pressure, and a 5.81×10^{-7} mbar TOF pressure. A vial of HPLC grade toluene was placed beneath the LIAD foil surface where the vapor present due to normal evaporative loss would act as an APPI dopant. The liquid level was checked and replenished periodically to ensure a consistent atmospheric concentration between experiments. A 1064 nm Nd:YAG laser (Continuum, San Jose, CA, USA) with a spot size of 0.11 cm^2 was aligned directly with the mass spectrometer inlet capillary at a power density of 0.6×10^8 W/cm^2, and operated at a pulse frequency of 10 Hz. This laser strikes the backside of the foil ejecting molecules via the LIAD process into the region containing toluene photoions generated by Lyman-α photons from the MHCD. These molecules are then ionized via APPI mechanisms near and flowing towards the inlet of the mass spectrometer and are then collected. This process is schematically shown in Figure 2.2. Before all experiments the MHCD was on with toluene present and signal was monitored. Base peak intensity from toluene oxidation products was observed to be between $1\text{-}1.5x10^4$ counts and only significantly deviated from that amount if the photon producing discharge was observed to be unstable. Typical compound analyses were accomplished by taking 1 min of spectra in the 50-800 mass range, starting the laser pulse sequence after 6s of collection with only the MHCD running. This length of data acquisition was done to observe signal rise time and signal consistency over time. Cholesterol and α-tocopherol were studied in decreasing surface concentrations by depositing more dilute solutions of each on foil via the iMatrixSpray system.

2.3 **Results and Discussion**

2.3.1 Microplasma Lyman-α Output

The results for Lyman-α emission from the MHCD device are shown in Figure 2.3. The flow rate and hydrogen concentration used were held constant to observe the effect of plasma current on the output of the device. For the operating conditions described, Lyman-α flux was found to be greatest at a discharge current of 10 mA which corresponds to an applied voltage of -1130V. Though Lyman-α emission from MHCDs is known, it was important to assess generation and transmission through the LiF window for our particular device.

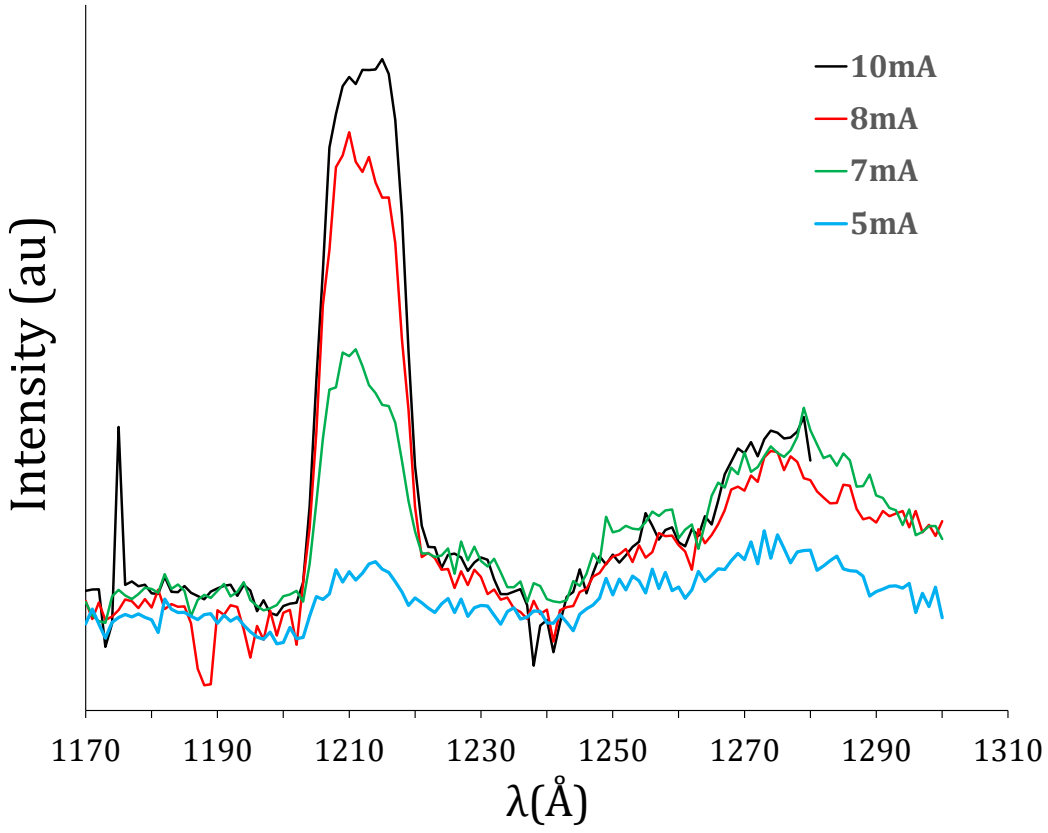

Figure 2-3: Measurements of Lyman-α emission at 1216 Å from the MHCD at varied discharge currents.

Previous reports of these devices typically have them operating at pressures below 1 atm.[72, 73, 90] This demonstrates that Lyman-α can be successfully generated in the relatively high-pressure environment of our device and transmitted through the LiF window for photoionization use. Benefits of using this device include a compact, low power consumption alternative for generating Lyman-α. It is shown here to be generated at as low as 7 mA corresponding to 5.8W of power consumption compared to 20 – 100W consumption by typical Lyman-α RF VUV lamps. The emission of MHCDs is also known to be relatively more efficient due to the hollow cathode geometry increasing the density of high energy electrons and leading to efficient excimer formation.[74] Also, MHCDs do not require a high voltage spark source to initiate plasma breakdown due to the low breakdown voltage achieved by using a 100 μm electrode spacing and a 760 Torr operating pressure. This brings the value of the pressure-distance scaling to be at or near a minimum along the Paschen breakdown curve.[91] As mentioned previously, the potential for MHCDs to be tunable photon sources also exists due to the observed spectral dependence on gas composition, plasma gas flow, and applied current/voltage.[74, 75, 88] With this in mind, it is conceivable that a set of operating parameters can be determined allowing for a tunable emission spectra to rapidly alter emission spectra to desired photon energies for photoionization purposes. In conjunction with carefully selected dopants according to their ionization potentials, this could lead to means of a minimally energetic form of APPI.

2.3.2 LIAD-APPI of Low-Polarity Organics

To extend the applications of microplasmas in MS and to demonstrate a novel means for desorption and mass analysis of low-polarity species, α-tocopherol, perylene, cholesterol, phenanthrene, phylloquinone, and squalene were chosen for analysis by LIAD-

APPI. For demonstration purposes, these analytes were deposited on the titanium foil in surface coverages of 10 nmol/cm^2. Control analyses were performed by recording spectra without the MHCD operating and laser firing. In every case no analyte signal was observed. This may be due to absorption by atmospheric water dropping the 10.2 eV photon flux by two orders of magnitude over a few centimeters in the region of the LIAD plume combined with the neutral number density of desorbates being too low to yield any appreciable amount of photoionized products. Thus the production and transport of toluene photoions within and towards the LIAD plume region has significant impact on ionization efficiency.

Resulting mass spectra taken in positive mode are shown in Figure 2.4. Interesting features of these spectra included relatively few species observed, dominated by the molecular ion for phenanthrene, perylene, α-tocopherol, and squalene while the cholesterol spectra favored the $[M\text{-}H_2O]^+$(m/z 368) and $[M\text{-}OH]^+$(m/z 369) peaks and exhibited a weak signal from the $M^{+\cdot}$ (m/z 386). The presence of the $[M\text{-}H_2O]^+$ peak from cholesterol has been observed before in early electron impact studies where the mechanism of its formation was suggested to be complicated.[92] Phylloquinone was also successfully analyzed presenting a $[M+H]^+$ base peak at m/z 451. Spectra from α-tocopherol, cholesterol, and phylloquinone were also consistent with spectra reported in studies using DAPPI using toluene as a dopant.[42] These results indicate LIAD-APPI is successful at desorbing and ionizing low-polarity organics; a class of molecules which is best suited to analysis by methods that do not owe their mechanism of ionization primarily to proton transfer. As a comparison, LIAD and synchrotron VUV photoionization have been combined previously under vacuum conditions to analyze heavy oils and lanthanide

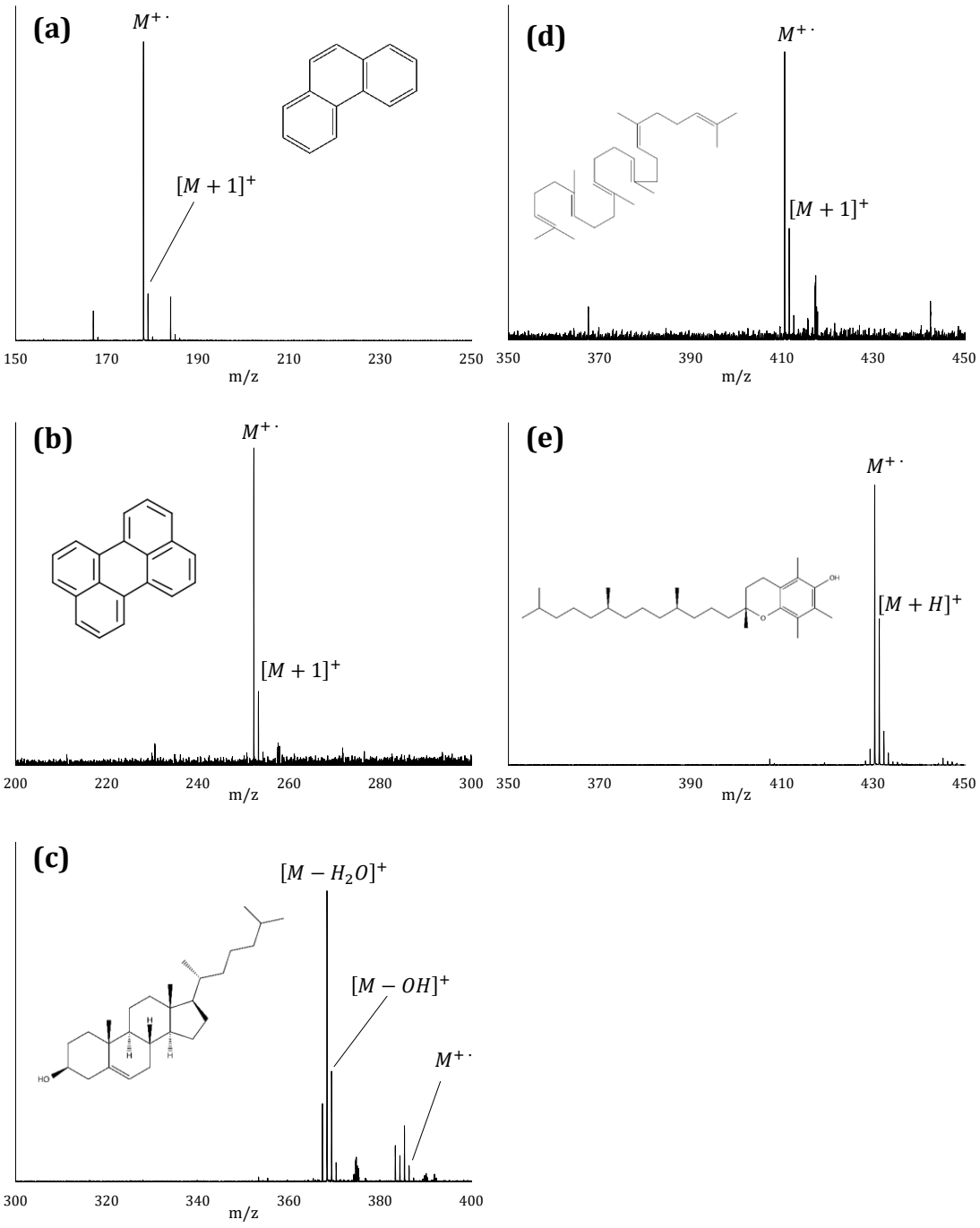

Figure 2-4: Positive ion mode spectra of phenanthrene (a), perylene (b), cholesterol (c), squalene (d), and α-tocopherol (e). Indicated masses are $M^{+\cdot}$ at m/z 178, $[M+1]^+$ at m/z 179 for (a); $M^{+\cdot}$ at m/z 252, $[M+1]^+$ at m/z 253 for (b); $[M-H_2O]^+$ at m/z 368, $[M-OH]^+$ at m/z 369, $M^{+\cdot}$ at m/z 386 for (c); $M^{+\cdot}$ at m/z 410, $[M+1]^+$ at m/z 411 for (d); and $M^{+\cdot}$ at m/z 430, $[M+H]^+$ m/z 431 for (e).

phthalocyanines extending up to m/z 1865.[81] Our analysis approach should allow for

higher sample throughput and a much easier and cost-effective method of photoionization in an atmospheric pressure setting.

2.3.3 Mechanisms of LIAD-APPI and Detection Limits

Mechanisms of APPI contributing to the effective ionization of low-polarity molecules desorbed via LIAD may include direct photoionization of the analyte, charge exchange with photoionized dopant molecules introduced in the sample region when the ionization potential (IP) of the dopant is greater than that of the analyte, and protonation of higher proton affinity analytes via reactive dopant photoions.[17] No signal was observed in the absence of the toluene dopant which is consistent with the observation that analyte ion-formation is heavily dependent upon the ion-molecule reactions with dopant photoions.[15, 17] Due to the relatively low IP of toluene (IP = 8.8 eV) compared to other high vapor pressure dopant molecules, e.g. chlorobenzene and acetone (IP $\geq$ 9 eV), we expect this to be a relatively soft means of charge transfer ionization.[93-95] The efficient formation of the molecular radical cation for the samples shown can be attributed to their effective ionization potentials. For α-tocopherol, phenanthrene, perylene, and squalene with IPs equal to 6.7 eV, 7.9 eV, 6.96 eV, and 6.9 eV respectively, it can be concluded that the molecular radical cation peak is dominant due to all IPs being lower than that of toluene by at least 0.9 eV.[96-99] This allows for a very favorable charge exchange. With cholesterol (IP = 8.5 eV) and phylloquinone (estimated IP = ~9.3 eV compared to IPs of vitamin K2 derivatives), the IPs lie closer to or exceed that of toluene owing to the less abundant radical cation formation from the charge exchange reaction.[100, 101] Early studies on cholesterol fragmentation support this observation using electron ionization at 70 eV and 16 eV where the molecular radical cation was found to be the dominant peak in

the mass spectrum and also demonstrate its sensitivity to internal vibrational temperature causing increased fragmentation.[92, 102]

Estimating the toluene number density in the air to be ~10^{16} mL^{-1} due to vapor diffusion and using a photoionization cross section of 3.0 x 10^{-17} cm^2 for 10.2 eV photons on toluene [103], the number density of toluene photoions can be estimated to be on the order of 10^5-10^6 mL^{-1}. This assumes a Lyman-α flux of 2.0 x 10^9 photons $s^{-1}sr^{-1}$ from an estimated 5% of total radiative output seen in Lyman-α lamps.[88, 104] This number is much smaller than the estimated number density of the desorbed products $N_{des} > 10^9$ mL^{-1}. This estimate assumes an average uniform upper bound for the toluene photoion density in the region of the LIAD plume whereas the actual photoion density may be localized about

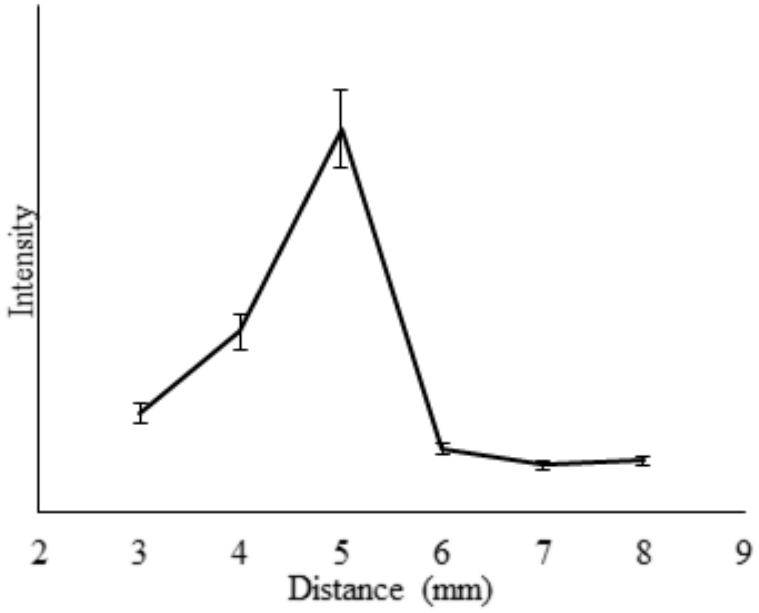

Figure 2-5: Plot of peak intensity of alpha-tocopherol $M^{+\cdot}$ versus foil distance from the inlet. Closer distances blocked the VUV emission, thus reducing the amount of available ions.

the window of the MHCD thus reducing the number density in the region of the plume even further. Thus the sensitivity for this source geometry is determined by the forward

ejection of the desorbates through the LIAD process and the pressure-driven flow at the inlet of the mass spectrometer but limited by the amount of toluene *ions* present lowering the ionization efficiency. Optimizing the setup to maximize collection consisted of observing base peak intensity of α-tocopherol spectra versus foil distance from the inlet. The result led to an optimum distance of 5 mm (Figure 2.5) relative to the mass spectrometer sampling port. The higher collection at the optimum distance is mainly attributed to closer proximities cutting off photon flux thereby reducing ions generated and further distances being too far for most desorbates to reach the inlet.

Due to the unknown amount of analyte desorbed by each individual laser shot, we report the amount detected to be the initial amount present on an area the size of the laser beam diameter due to the observed spatial disturbance of more concentrated films to be equal to that area. To assess the sensitivity of the technique, representative samples of cholesterol and α-tocopherol were deposited in decreasing amounts on titanium foil to observe the lowest detectable amount of analyte per spot sampled. These molecules were chosen due to the ease by which they could be deposited in uniform coatings via the deposition method described above. The peaks used to determine the lowest detectable amounts were chosen by observing the base peaks from the demonstrative spectra. Choosing a signal to noise ratio of 3 for the peaks monitored to be considered detectable, the lowest detected amounts correspond to 9.2 pmol for cholesterol and 3.0 pmol for α-tocopherol. The results shown in Table 2.1 demonstrate that the technique is sensitive enough to observe few pmol quantities for the compounds chosen. These values are at or slightly lower than lowest corresponding molar amounts reported in DAPPI studies however an estimated limit-of-detection of 190 fmol for α-tocopherol with DAPPI has been

reported.[42, 105] Improvements to obtain similar values such as using atmospheric dopant sprays to aid in desorbate transport and increase toluene photoion number density in the plume region are currently being explored. This would retain the known ability to softly desorb large molecular weight species with LIAD and aid in their atmospheric transport

Table 2-1: Lowest Detected Amounts of Cholesterol and α-tocopherol. Foil coverage values were calculated using parameters from the iMatrixSpray system and relative error based on inhomogeneity of sample and uncertainty in laser spot size.

Compound	Representative Peak	Solution Conc. [μM]	Surface Conc. (pmol/cm^2)	Lowest Detected Amount (pmol/spot)	Relative Error (±pmol/spot)
cholesterol	m/z 368 $[M\text{-}H_2O]^+$, m/z 369 $[M\text{-}OH]^+$	8.3	8.3	9.2	±2.8
α-tocopherol	m/z 430 $M^{+\cdot}$	2.7	2.7	3	±0.9

and ionization without overheating the sample. Overall the results clearly indicate the potential for LIAD-APPI to be a highly sensitive technique for the analysis of low-polarity organics under ambient conditions.

2.4 Conclusion

The first application of laser-induced acoustic desorption and atmospheric pressure photoionization as a mass spectrometric method for detecting adsorbed low-polarity organic molecules has been demonstrated. The unique approach involved the use of a Lyman-α generating microhollow cathode discharge microplasma photon source in conjunction with the addition of a gas-phase molecular dopant. This combination provides both a soft desorption method and a relatively soft ionization technique. The total energy inherent in the desorption step is low and the total energy deposited in the product ion is

low enough to produce spectra with minimal fragmentation for most molecules. Detectable surface concentrations as low as a few pmol per spot were achievable using test molecules such as α-tocopherol and cholesterol. Efforts are underway to improve the ion transport and toluene photoion density parameters which should extend the mass range to higher molecular weights and allow detection of lower concentrations than shown here. These include the use dopant sprays to aid in transport and increase ionization efficiency of molecules while still using LIAD as the main desorption mechanism. The sample preparation and analysis technique together may prove useful in detecting reaction products generated from drying aerosol sprays on metal surfaces. If successful, LIAD-APPI may prove to be a useful approach to detecting larger and more labile molecules, molecular assemblies, and aggregates than shown here.

2.5 **Acknowledgements**

This work was jointly supported by NSF and the NASA Astrobiology Program, under the NSF Center for Chemical Evolution, CHE-1504217. Work at JPL on VUV detection was supported by a joint Jet Propulsion Laboratory-Georgia Institute of Technology Strategic University Research Partnership (JPL-GIT SURP) grant.

CHAPTER 3. SWEEP JET COLLECTION LASER INDUCED ACOUSTIC DESORPTION ATMOSPHERIC PRESSURE PHOTOIONIZATION FOR LIPID ANALYSIS APPLICATIONS

Laser-induced acoustic desorption coupled to microplasma-based atmospheric pressure photoionization (LIAD-APPI) using a nebulized sweep jet to aid in dopant introduction and ion transmission has been applied to the analysis of model, apolar lipid compounds. Specifically, several sterols, sterol-esters, and triacylglycerols were detected using dopants such as anisole and toluene. Additionally, several triacylglycerols, sterols, carboxylic acids, and hopanoids were detected from complex mixtures of olive oil and Australian shale rock extract as a first demonstration of the applicability of LIAD-APPI on real world samples. Detection limits using a sweep jet configuration for α-tocopherol and cholesterol were found to be 609 ± 61 and 292 ± 29 fmol, respectively. For sterol-esters and triacylglycerols with a large number of double bonds in the fatty acid chain, LIAD-APPI was shown to yield greater molecular ion or $[M+NH_4]^+$ abundances than those with saturated fatty acid chains. Dopants such as anisole and toluene, with ionization potentials (IPs) of 8.2 and 8.8 eV, respectively, were tested. A greater degree of fragmentation with several of the more labile test compounds was observed using toluene. Overall, LIAD-APPI with a nebulized sweep jet requires minimal sample preparation and is a generally useful and sensitive analysis technique for low polarity mixtures of relevance to biochemical assays and geochemical profiling.

3.1 Introduction

Traditional atmospheric pressure mass spectrometry (MS) ion production and sampling techniques such as electrospray ionization (ESI) and matrix-assisted laser desorption ionization (MALDI) are typically used to obtain information regarding the lipid profile of complex samples [106]. ESI typically yields $[M+H]^+$ or $[M-H]^-$ ions for positive or negative mode, respectively. However, it struggles to sensitively detect sterols, triacylglycerols, and low-polarity compounds without ammonia or metal ion adduct formation [9, 107-109]. While being able to analyze extended mass ranges, MALDI requires careful selection of a co-crystallization matrix to ensure the correct information can be gathered from the sample due to both desorption efficiency and the polar mechanism behind the ionization event [110, 111]. Therefore, considerable effort has been made towards developing desorption/ionization techniques to analyze these types of low-polarity species [3]. A well-studied example of these techniques is atmospheric pressure photoionization (APPI) [15]. In an APPI-related technique, known as desorption atmospheric pressure photoionization (DAPPI), a heated solvent jet is used to lift analytes into the gas phase and undergo APPI [27]. While this has been shown to be useful for low-polarity compounds, studies report that high thermal heating of the sample is required to analyze heavier species.[42] This can be problematic for larger, thermally labile lipids. In addition to DAPPI, there have been several examples of laser ablation/desorption atmospheric pressure photoionization techniques in the literature [25, 78]. This class of techniques boasts benefits including high spatial resolution and sensitive response to low-polarity compounds but, direct laser irradiance leads to higher ion activation and is limited to relatively low molecular weight compounds [79].

The applications of MS to lipid analysis have spanned a range of sample classes including biological tissues, food oils, minerals, and even abiotic lipid systems [107, 112, 113]. On the topic of minerals, shale rocks from deposits across the world have been studied by MS to understand their apolar composition [114-116]. More recently, the lipid profile of shale and other carbonaceous rocks have been shown to be markers for distinguishing abiotic and biotic carbon sources [117]. Therefore, a tool to robustly analyze these types of components could be useful in the search for prebiotic and early life lipid fingerprints. As for low-polarity lipid systems, triacylglycerols are particularly important due to their relevance in biological systems and food products such as olive oil. Additionally, these are also expected to be formed in abiotically plausible Fischer-esterification reactions between glycerol and carboxylic acids [118].

Previously, laser-induced acoustic desorption (LIAD), has been coupled to a microplasma-based APPI source to effectively desorb and ionize non-polar to low-polarity compounds deposited on Ti thin-foils [1]. This development i) alleviates the need for a heated solvent jet used in DAPPI, ii) eliminates the task of matrix selection found with MALDI, and iii) offers a well-known ability to efficiently desorb virtually any mass or class of intact molecular compounds from a foil surface [50, 80-82]. Additionally, LIAD avoids direct laser irradiation of the sample leading to fragmented gas-phase molecules as seen with direct laser ablation techniques. These capabilities make LIAD an ideal desorption technique requiring no sample pretreatment and minimizing the amount of energy imparted to the desorbed species. LIAD is most typically accomplished by back irradiating a 5 – 20 μm thick foil with a laser focused to a power density of ~ 10^8 W cm^{-2}. For this experimental regime, it is suggested that irradiating the backside of the foil

generates an acoustic-thermal wave distorting the opposite side. The subsequent cracking and release of intrinsic stresses known to exist in the deposited films gives rise to repulsive electronic states that lead to desorption of molecular analytes into the gas phase with relatively little energy imparted to the desorbed species [55, 57, 119]. However, confirming the exact nature of the surface-adsorbate interaction in the LIAD process is an area that requires further investigation.

In this chapter, LIAD-APPI using a nebulized dopant jet to desorb, ionize and collect low-polarity compounds for MS applications is described. APPI is accomplished using a previously-described VUV generating microhollow cathode discharge (MHCD) [1, 88]. The combination of sweep jet collection, robust desorption with LIAD, and charge transfer ionization with MHCD-enabled APPI allows analysis of large low-polarity sterol and lipid compounds. Due to this combination, this work demonstrates the analysis of olive oil and apolar Australian shale extracts as examples of the types of analyses that can be carried out using LIAD-APPI. We also present performance improvements with sweep-jet collection through experiment and qualitative investigations using computational fluid dynamic (CFD) simulations of the desorption/ionization source flow fields for different geometries.

3.2 **Experimental**

3.2.1 Materials and Chemicals

All low-polarity standards (cholesteryl-palmitate, cholesteryl oleate, cholesteryl linoleate, glyceryl trioleate, glyceryl trilinoleate, glyceryl trinonadecanoate, cholesterol, α-tocopherol, ergosterol) and various solvents (ethanol, chloroform, ethyl-acetate, ethyl-

ether) were purchased from Sigma Aldrich (St. Louis, MO, USA). The atmospheric dopants used, *ReagentPlus*® 99% anisole and OmniSolv® 99.9% toluene, were also purchased from Sigma Aldrich. For olive oil experiments, a known high-quality brand of extra virgin olive oil (EVOO) (California Olive Ranch, Chico, CA, USA) was used.

To test the LIAD-APPI method with an unknown, a sample of black shale from the Corcoran Formation, Australia was investigated. The sample was a gift from Andrew Knoll, designated in his collection as K99 A82/3 479.2, 34.5 m. The age of the Corcoran Formation has been dated to 1.45 billion years, and the shale is known to preserve organic compounds from microbial life and algae.

Titanium thin-foil with thickness of 12.7 µm (99.8% metals basis) was purchased from Alfa Aesar (Ward Hill, MA, USA). The MHCD device used in these experiments was designed and custom built as previously described [1]. Circular MHCD electrodes were fabricated with ~100 µm diameter hollows from molybdenum foil (100 µm thick) purchased from Sigma Aldrich. Lithium fluoride windows used to seal the device from the external environment were custom ordered from Crystran (Poole, Dorset, UK). For the samples where specific surface concentration was needed, the iMatrixSpray deposition system (Grubenacker, Switzerland) was used to deposit samples via a nebulized stream of solution in repeated coatings giving a reproducible surface homogeneity [89].

3.2.2 Sample Preparation & Deposition

Solutions for limits of detection experiments were prepared individually by depositing α-tocopherol and cholesterol solutions prepared in ethanol and ethyl-acetate, respectively, with concentrations of 100 nM to 100 µM using 10 coating cycles on the

iMatrixSpray system. Ten cycles were used to ensure a pixel to pixel coefficient of variance of 7% or less [89]. Analyzed standard samples were prepared by pipetting 100 µL of ~ 1 mM solutions onto Ti foil and let dry until all liquid had evaporated. EVOO on Ti foil was prepared by first diluting 1 mL of EVOO to 10 mL with chloroform, and depositing with the iMatrixSpray system.

Extraction of three to five grams of the two types of Australian shale rocks was performed by first breaking the rocks into a rough powder in a cleaned foil container. The powder was ground for ~ 5 minutes with a mortar and pestle and 3 mL 2:1 v/v mixture of chloroform-methanol and 1 mL of H_2O was added and subsequently ground for ~ 5 min. The thick gray slurry and liquid were transferred to a brown glass vial with 8 mL of the chloroform-methanol mixture. The mixture was then centrifuged at 4000 rpm for 5 min in glass centrifuge tubes to separate the two layers. The bottom, chloroform phase was decanted into brown glass vials for storage after pipetting off the top aqueous phase. The chloroform phase was then pipetted in 5 applications of 100 µL to the Ti foil for LIAD-APPI analysis.

3.2.3 MHCD Device & Operation

Previously, MHCD devices have been fashioned in a similar manner for use as VUV photon sources under ambient conditions [1, 88]. The device used in this work is an iteration of the previous two where improvements include reducing the overall device diameter from a cylindrical 3.68 cm to a cubic design with 2.67 cm width/height, symmetrizing the inlet and outlet flows of the device (Figure 3.1a), and switching the hydrogen introduction component of the flow system to a 0-10 sccm mass flow controller

(MFC). This low flow rate controller is used to introduce H_2 into the Ne gas stream for efficient Lyman-α (10.2 eV) light generation [73]. Flow settings for the device were consistently kept at a total flow rate of 40 sccm of Ne containing 4% H_2 controlled by the two FMA-5500 series MFCs from Omega Engineering (Stamford, CT, USA). These

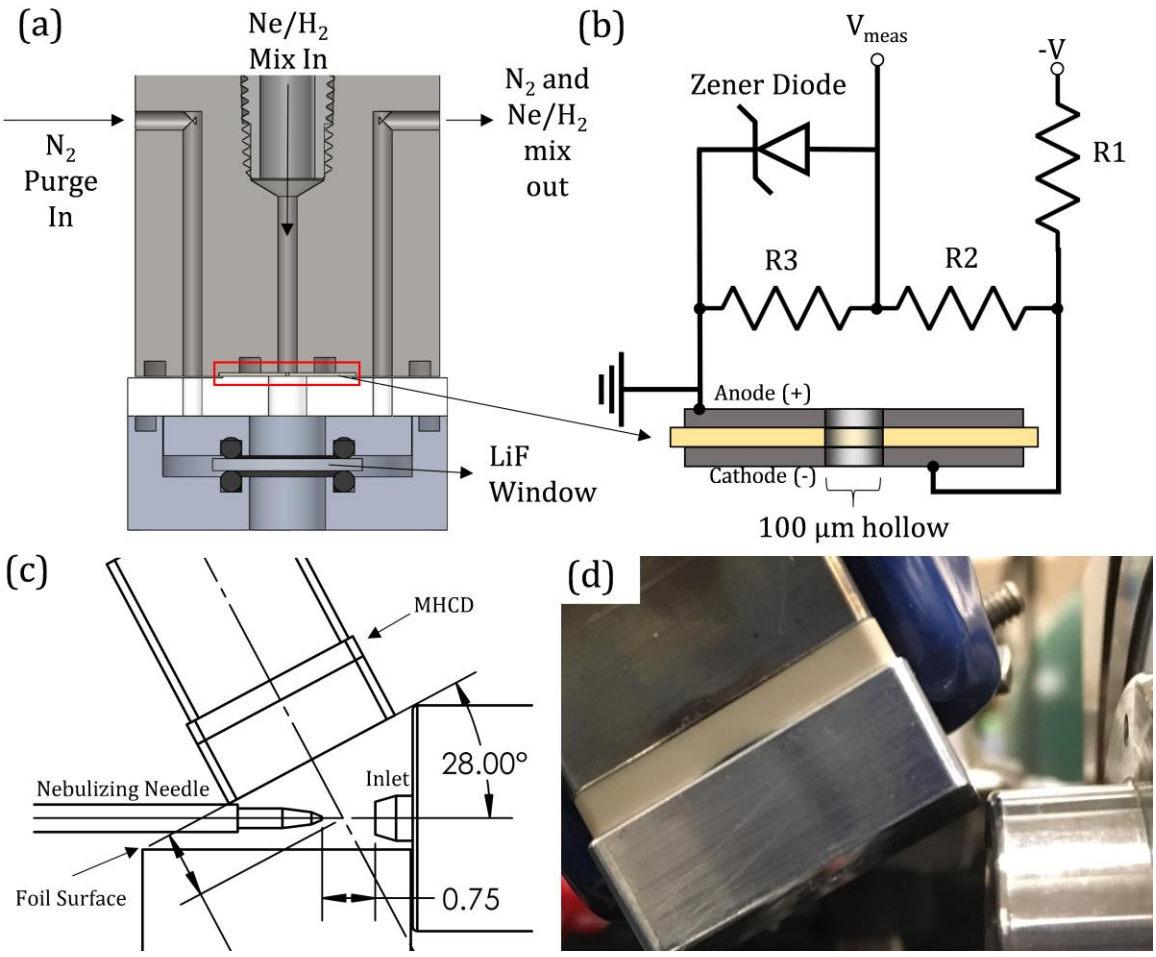

Figure 3-1: (a) Image of the cross section of the MHCD photoionization device and housing illustrating flow characteristics. Ne/H_2 mix was introduced via the 1/16" NPT fitting at the top of the device. Not shown are the welded 1/8" tubes for the in/out flow channels on either side of the device. (b) Circuit diagram showing how voltage was applied to the cathode using R1 (= 97 kΩ) as the primary ballast resistor and voltage divider (R2 = 21 MΩ, R3 = 560 kΩ) used for observing the discharge potential (adapted from Benham *et al.* 2016). (c) Scaled drawing of the LIAD-APPI set up where the VUV generating MHCD was at a 28° angle to the inlet centerline, nebulizing needle was positioned 0.75 cm from the inlet, and the intersection point of the illuminating glow of the MHCD and dopant sweep jet was 0.94 cm from the exit of the MHCD. (d) An image of the actual set up.

settings are expected to both reduce gas impurities in the discharge as well as increase excimer yields leading to higher photon output [75]. For all mass spectrometry experiments, current was limited between 9 – 10 mA using a ballast resistor (Figure 1b) and the Stanford Research Systems model PS350 power supply (Sunnyvale, CA, USA) leading to applied voltages between -1000 and -1150V.

3.2.4 Sweep Jet LIAD-APPI Setup

To improve the response and sensitivity of LIAD-APPI, a new configuration was adopted (Figure 3.1c). Here, the foil is placed just below the inlet and the 1064 nm Nd:YAG laser (Continuum ®, San Jose, CA, USA) is focused to a point on the back-side of the foil passing in front of the inlet with a pulse width of 7 ns and rate of 10 Hz. This results in a desorption plume directly in front of the inlet which is orthogonally intercepted by a sweep gas containing the atmospheric dopant introduced by a nebulizing needle. The MHCD is positioned such that it is illuminating the sweep gas mixture thereby generating the photoions needed for ionizing the LIAD desorbed plume. Proximity of the MHCD axis to the axis of the nebulized dopant spray was minimized by setting the MHCD face at a 28° angle with the nebulizer giving a centerline distance of 0.94 cm with the intention of reducing the effects of Lyman-α attenuation by atmospheric water and oxygen (Figure 3.1c). An image of the actual experimental set-up is shown in Figure 3.1d. The LIAD laser was kept at a power density of 0.8×10^6 W cm^{-2} measured and determined from the averaged focused spot diameter of 2.025 mm. The nebulizer flow rate was controlled by the pressure setting in the Bruker control software set to a relative pressure of 1 bar. Flow rate for dopant introduction was measured to be 9.75 µL min^{-1}.

3.2.5 Mass Spectrometry Experiments

The primary mass spectrometer used for these studies was a Bruker micrOTOF-Q II. The instrument was operated primarily in positive ion mode with a typical high vacuum pressure of 4.10 x 10^{-7} mbar, low vacuum of 1.91 mbar, +50 V capillary bias, -50 V end plate offset, 5.0 L min^{-1} N_2 dry gas, and a drying/capillary temperature of 125 °C. In the experiments to identify the $[M+18]^+$ species observed, we reproduced these standard source settings on a Bruker solariX XR 12 T Fourier transform ion-cyclotron resonance (FT-ICR) mass spectrometer. For standard analyses and EVOO analysis, a modified version of Bruker's default wide tuning method assured signal for ions entering the instrument from m/z 200 – m/z 3000. However, it should be noted that ion transmission through the series of RF components was highly dependent on the peak-to-peak voltage settings of each ion optics element. Thus, it was difficult to obtain signal over a wide m/z detection range and, in most cases, lower masses were poorly transmitted. For all experiments the resolving power was found to be ~6,000 using the full-width at half maximum estimation. For the analysis of black shale extracts, a lower mass tuning method was used providing greater transmission for the m/z 100 – m/z 600 range. Masses were calibrated using a standard ESI tuning mix (Sigma Aldrich, St. Louis, MO, USA) on a weekly basis. In general, masses were observed to remain accurate except in the event of instrument shutdown, or significant HV changes.

3.2.6 CFD Simulations and Computational Details

The software used in this work was COMSOL Multiphysics version 5.3a (COMSOL, Burlington, MA) and the simulations were carried out on a Dell desktop

computer with a 3.40 GHz Intel® Core™ i3-3240 dual-core processor and 8 GB of memory. The geometries used in these studies were drawn using SolidWorks computer-aided design software. The forward ejected system was modeled as a 2D axisymmetric geometry whereas the sweep jet configuration was modeled as a 2D cross-section of the source due to lack of symmetry. To obtain better convergence of more computationally intensive models, an initial "guess" velocity field was first calculated using the less computationally intensive k-ε turbulence model [120]. All simulated flow fields were obtained in the absence of thermal convection and particle trajectories were modeled without the small electric field produced by the 50 V bias on the mass spectrometer inlet capillary.

3.3 **Results and Discussion**

3.3.1 Sweep Jet Collection Improvements

For all standard analysis experiments, solutions of the various components were deposited in surface concentrations of up to ~ 50 nmol cm^{-2}. With this surface concentration, similar time-series signal response to LIAD was observed for sterol, sterol-ester, and α-tocopherol samples. Figure 3.2a illustrates the typical extracted ion chronograms of the $[M-H]^+$, $[M]^{+\bullet}$, and $[M+H]^+/[M+1]^{+\bullet}$ (i.e. protonated and ^{13}C isotopic) species of α-tocopherol produced by the forward-ejected LIAD-APPI configuration (dotted black line). Also shown is a significant signal response (solid red line) improvement for the sweep jet configuration. In both experiments for both configurations (Figure 3.2b-c), the laser pulse sequences were started at 6 s and ion abundance was

observed to be higher for the sweep jet configuration sampling a spot of 60.24 pmol versus 118.8 pmol for the forward ejected.

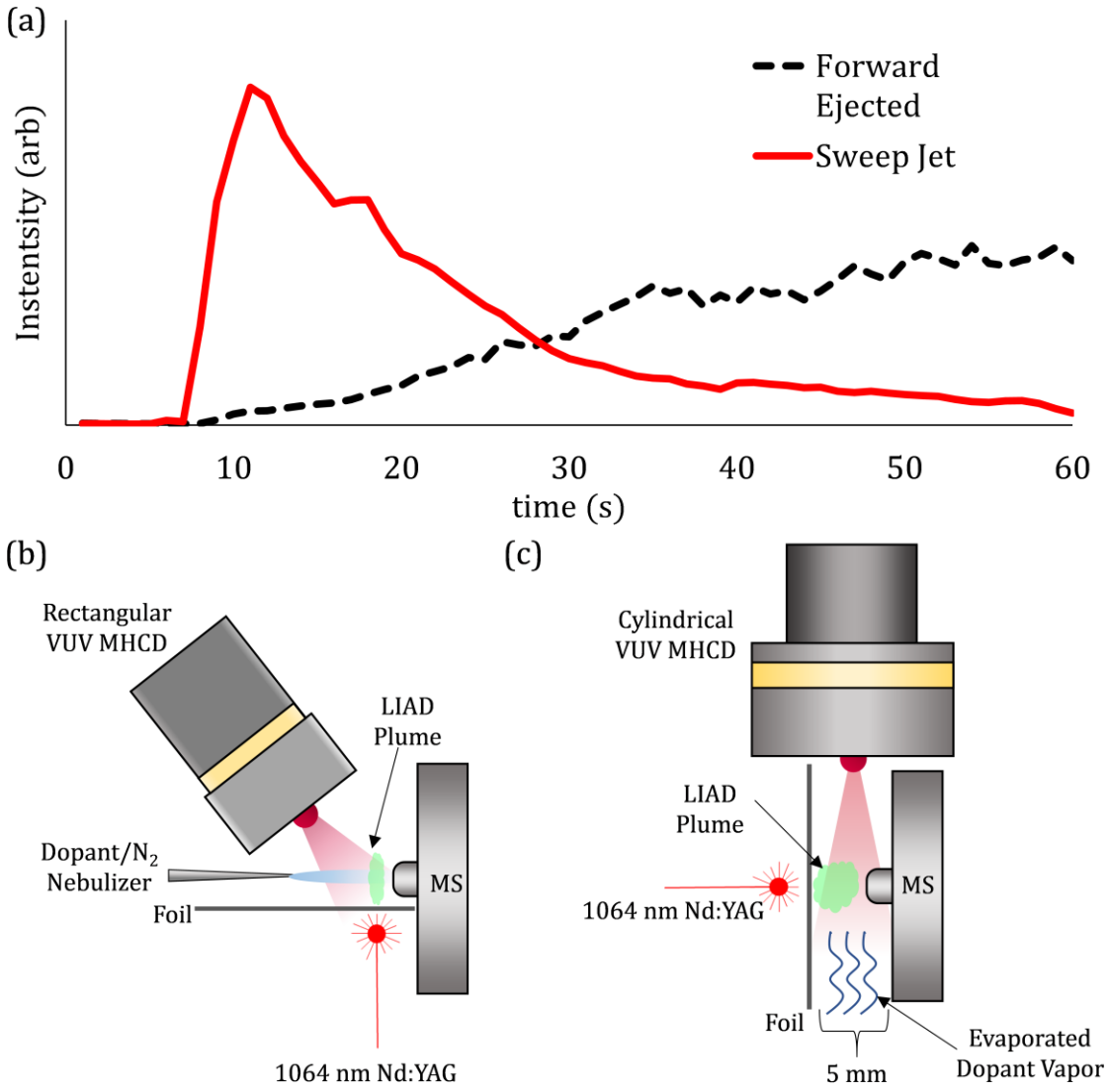

Figure 3-2: Extracted ion chronograms for α-tocopherol determined from the $[M-H]^+$, $[M]^{+\bullet}$, and $[M+H]^+/[M+1]^{+\bullet}$ species. (a) The red line indicates signal obtained using the sweep jet configuration and the dotted black line represents the response using the forward ejected approach. (b) illustrates a schematic of the sweep jet configuration and (c) illustrates the schematic for the forward-ejected approach adapted from Benham et al. 2016.

It is apparent that overall collection efficiency has greatly improved using the sweep jet collection. This has also led to an improvement in the limits of detection (LODs) for the standard APPI test compounds, α-tocopherol and cholesterol at 609 ± 61 and 292 ± 29 fmol, respectively. Detection was confirmed by observing the base peak(s) for the compounds that exhibited clear desorption response and had a S/N of at least 3. The LODs were determined from surface concentrations as defined by iMatrixSpray parameters and the desorption area (assumed to be circular) defined by the measured laser spot diameter of 2.025 ± 0.72 mm. The deviations correspond to the errors due to surface homogeneity and measurement uncertainty in the laser spot added in quadrature. Tocopherol was found to be most sensitively analyzed with anisole whereas cholesterol detection was most sensitive with toluene as an atmospheric dopant. The larger triacylglycerols displayed a

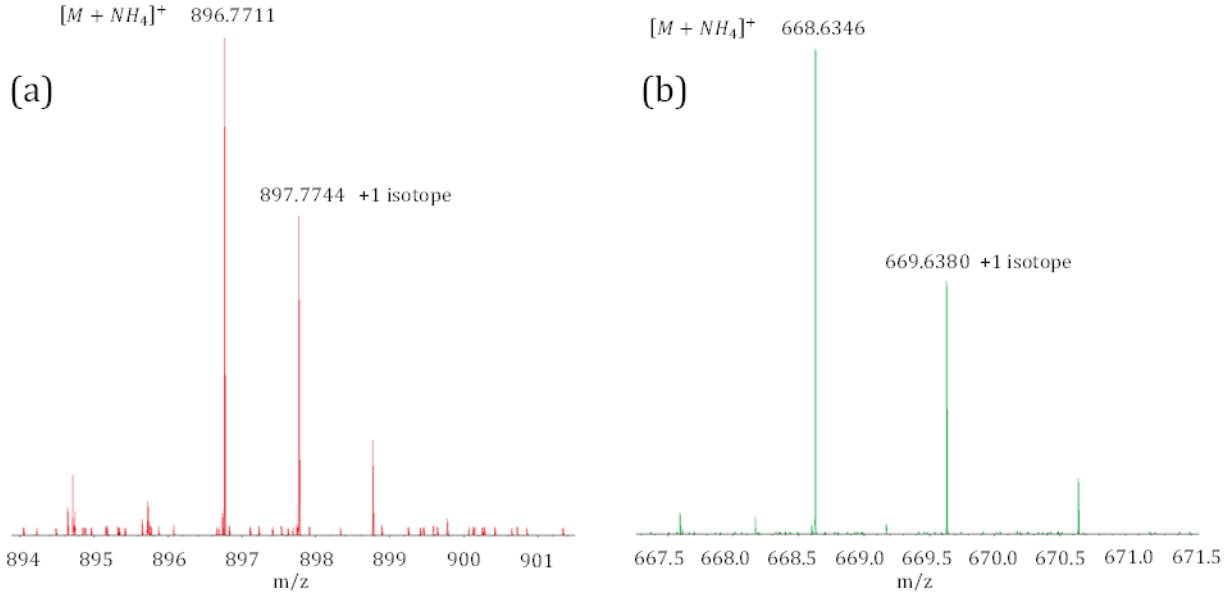

Figure 3-3: FT-ICR spectra of (a) glyceryl trilinoleate ammonium adduct with mass error of 0.508 ppm and resolution of 167,188. (b) spectra of cholesteryl oleate ammonium adduct with mass error of 0.188 ppm and resolution of 222,534.

longer time constant to reach full abundance. The primary reason for this likely results from the slower uptake into the mass spectrometer due to the larger collisional cross

sections and increased transport times even with the nebulized jet. For all standards, at least some appearance of a $[M+18]^+$ species was observed. To identify its origin, we reproduced the source configuration on a Bruker FT-ICR and re-tested several standard compounds. Ultimately, it is concluded that the $[M+18]^+$ species for these compounds can be definitively attributed to the ammonium adduct $[M+NH_4]^+$ using FT-ICR MS with a resolving power of 167,188 or greater, and sub-ppm mass accuracy (Figure 3.3).

3.3.2 CFD and Particle Trajectory Simulations

To elucidate the dynamics behind the observed collection improvements, the flow regimes for the inlet and capillary were investigated for both source configurations (Figure 3.4, Figure 3.5). Subsequently, particle tracing simulations were performed to observe the

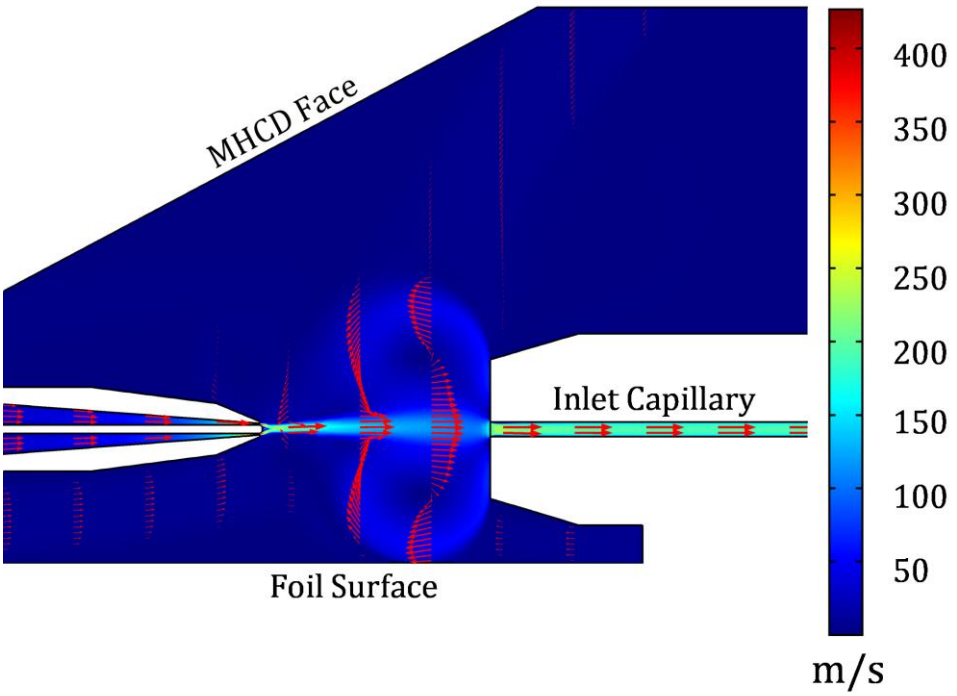

Figure 3-4: Sweep jet velocity magnitude color map and flow field vectors reflecting velocity direction and magnitude on a logarithmic scale. Total geometry not shown for ease of visualization.

dynamics of this uptake (Figure 3.6). These computations were carried out using the finite-element method in COMSOL Multiphysics software, a known computational tool previously applied to model other ion sources [121-123]. To obtain an accurate comparison of the flow for both regimes, primary inlet and outlet boundary conditions were modeled as constant pressures.

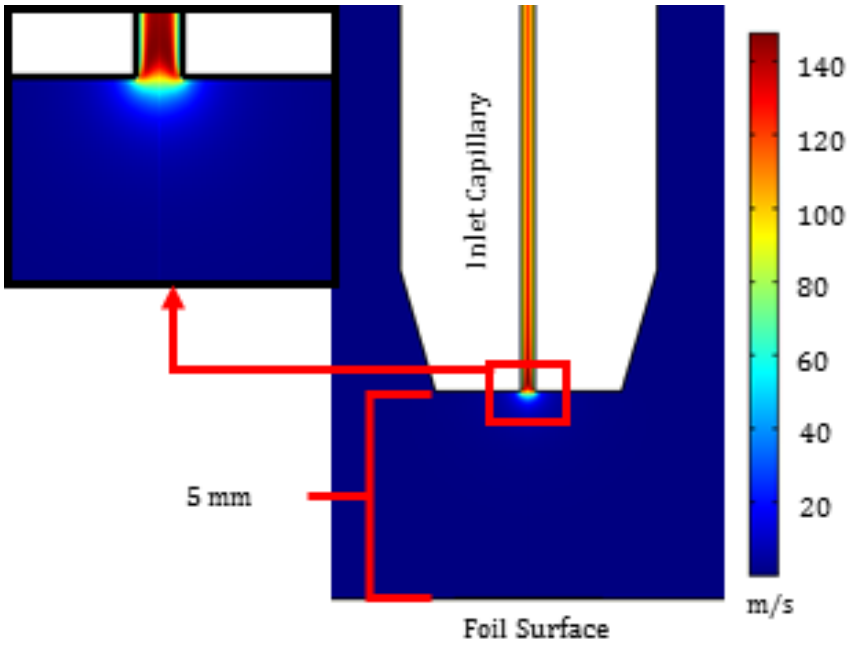

Figure 3-5: Forward-ejected velocity magnitude color map. Flow is entirely due to the low-pressure boundary condition (constant at 191 Pa) at the end of the inlet capillary in the geometry (not shown). Inset illustrates velocity increase only near the inlet at a distance of ~0.4 mm.

As a result, the sweep jet model is characterized by a 202.65 kPa air pressure entering the back of the nebulizer needle and a 191 Pa outlet pressure at the end of the MS glass capillary obtained by the measurements and settings given by the mass spectrometer control software. Other important conditions included the assumption of incompressibility

and no-slip boundary condition for all wall surfaces, reasonable assumptions given the higher pressure environment and expected absence of Knudsen flow. Notably, this leads to adverse pressure gradients which required use of Menter's Shear-Stress Transport (SST) model [124]. This two-equation eddy-viscosity model is used to satisfy the Reynolds-averaged Navier-Stokes (RANS) equations which are essentially modeling the velocity field as a superposition of a time averaged velocity component and a fluctuating component. Resulting stationary flow fields indicate that deflection of sweep jet flow lines directed towards the inlet surface combined with the relatively low resistance flow of the inner flow lines entering the inlet generate a substantial swirling vortex (Figure 3.4). This effect creates a relatively active flow field near the foil surface that draws particles into the jet and eventually transports them into the inlet capillary.

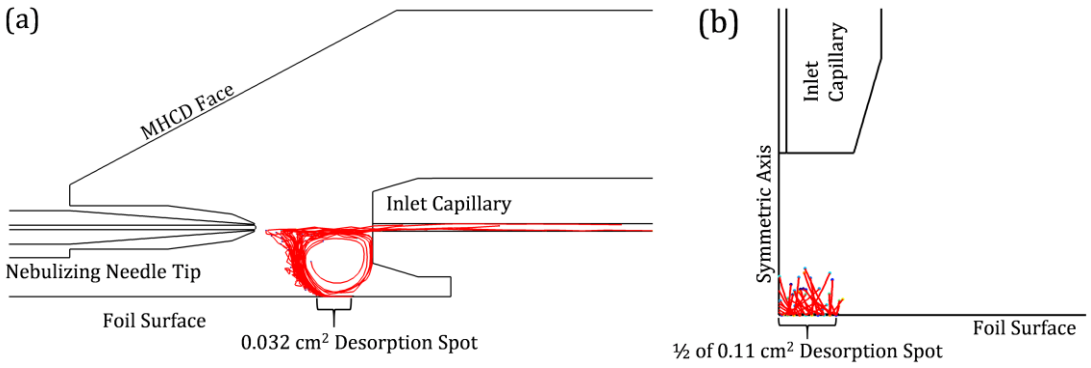

Figure 3-6: Simulated trajectories of the ejected attogram particles. Particles were initially uniformly distributed on the desorption spot with initial velocities of 50 m s^{-1}. The red paths in (a) show the particle trajectories in the sweep jet configuration after 0.7 ms illustrating the high degree of movement and faster collection at the inlet. The red paths in (b) represent the trajectories taken by each particle for the forward ejected setup after 5 ms. This was simulated on the 2D symmetric geometry used for calculating the flow fields thus particle movement is not simulated through the other half of the geometry.

As for the forward ejected configuration, the simpler geometry and lack of conical jet flow from the nebulizing needle allowed for simpler models to be used. Variables for the turbulent-dispersion model used for particle trajectory simulations were obtained through the k-ω turbulence model [125]. For comparison purposes, the laminar flow model offered a 25% increase in the magnitude of the velocity field very near to the inlet. Though the laminar velocity field is expected to be physically reasonable for the conditions in this geometry, this ultimately would be of no consequence to the particle simulations due to the relatively inactive velocity fields simulated between the foil surface and the inlet for both models.

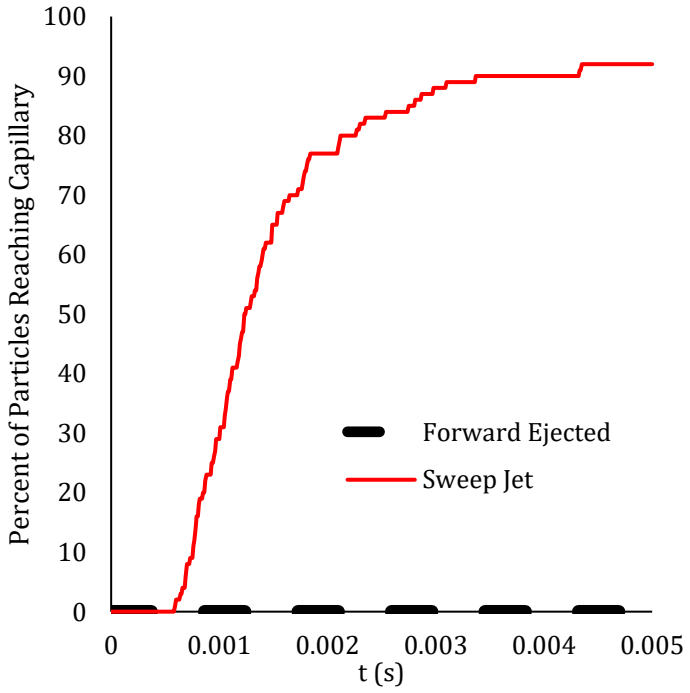

Figure 3-7: Particle accumulation in the capillary vs time for the particle simulations described.

To investigate collection of desorbed species in these simulated flow fields, a particle trajectory simulation was used. The particles were assumed to be hard spheres 1 nm in diameter weighing 1 attogram. Lighter particles, more comparable to the molecular

weight range studied, were not simulated due to convergence issues and required computational time. These particles were assumed to be ejected with velocities of 50 m s^{-1} from the defined sample spot, to experience drag forces from the fluid environment, and a force due to Brownian motion [55]. For the simulations, the electric field caused by the small potential on the inlet capillary was neglected due to computational complexity and likelihood that the forces exerted by the fluid are greater than the electrostatic force generated by the small potential for these experiments. The particles trajectories were simulated for both geometries up to 5 ms. For the sweep jet geometry, results indicated that the particles are first drawn into the swirl flow, at some point enter the forward stream, and eventually reach the spectrometer inlet. Figure 4a traces the trajectories of the desorbed particles from t = 0 until t = 0.7 ms to illustrate their path in the swirl flow. However, a better representation of these simulations in gif formatted video clips can be found at http://ww2.chemistry.gatech.edu/~orlando/epicslab/AtmSurfChem.html .

By the completion of the simulation at 5 ms, 92 of the 100 particles simulated have entered the inlet (Figure 3.7). Another benefit of this configuration is with the expected increase in collisions. The relatively high range of movement of these particles would cause more collisions with dopant photoions generated in the stream, thereby increasing the likelihood of analyte ionization. This is in stark contrast to the forward ejected configuration where no particles have entered the inlet by 5 ms. Therefore, it seems any collection with the forward ejected configuration is likely due to molecular diffusion to the inlet after the gaseous concentration near the foil is raised high enough from repeated desorption events increasing the concentration gradient. We do note the electric field in

this instance may have a non-negligible influence on particle trajectories given the lack of convection for transport.

To summarize, key differences in these simulations lie with neglecting the effect of the electric-field, unaccounted signal time delays due to ion storing protocol within the mass spectrometer, the use of attogram particles, and neglect of thermal effects on transport. Nevertheless, these results qualitatively explain the importance of the flow in the sweep jet configuration giving improvements like those seen in Figure 3.2a.

3.3.3 Sterols and Sterol Esters

Because one intent of this technique is to provide a desorption/APPI platform that maximizes molecular information for apolar chemical samples, we tested sterol-ester standards to establish performance on larger, labile apolar lipids. These were also chosen because of the inherent difficulties associated with their analysis via ESI, and relevance to biological and enriched oil samples [109, 126, 127]. In Figure 3.8a,b,c, the results are shown for cholesteryl palmitate, oleate, and linoleate, where common features include a large signal from the loss of the neutral fatty acid denoted $[M\text{-}FA]^+$, a protonated dimer , and the $[M+NH_4]^+$ adduct for both toluene and anisole as atmospheric dopants. For cholesteryl palmitate and cholesteryl oleate, only small $M^{+\cdot}$ signals are observed but for cholesteryl linoleate, a very large molecular ion is observed. While ionization of cholesteryl oleate has been studied using DAPPI, the $[M+NH_4]^+$ species was not reported [128].

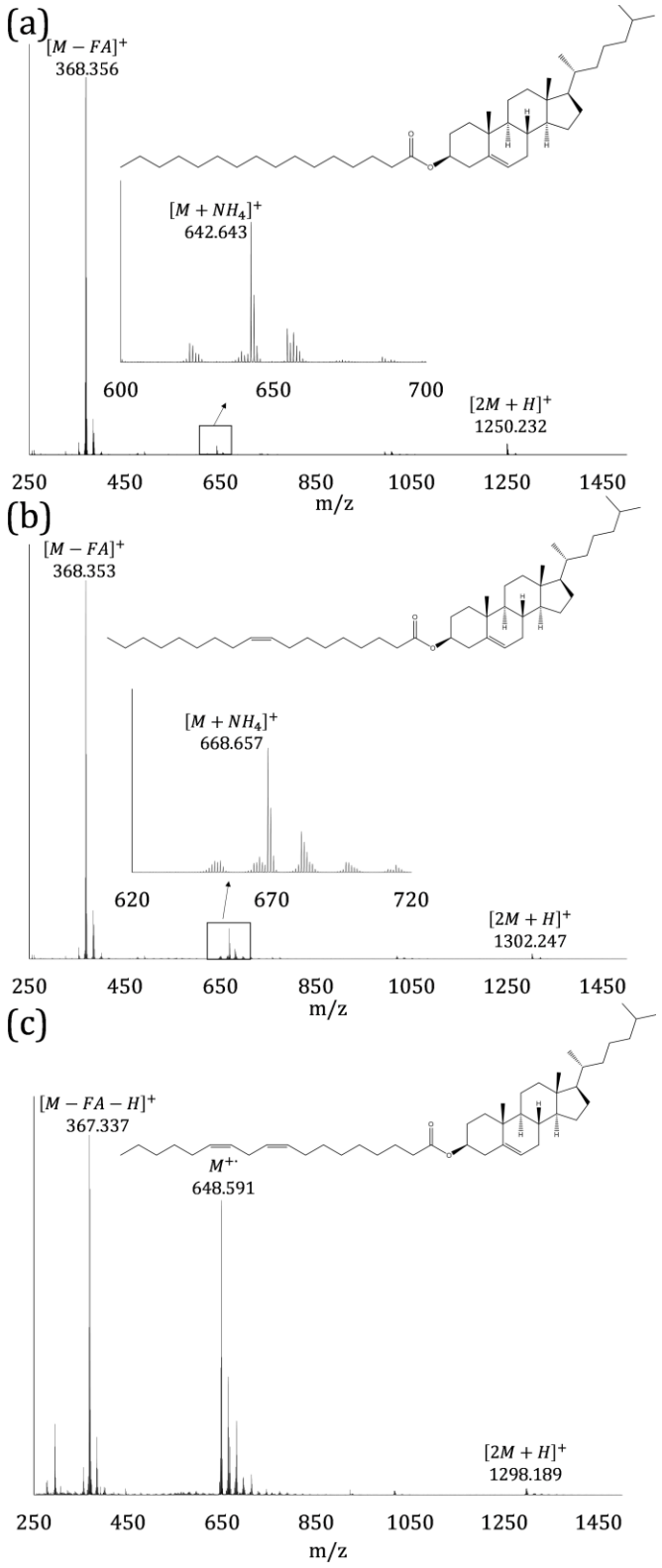

Figure 3-8: Spectra taken in positive mode LIAD-APPI with toluene as the dopant for (a) cholesteryl palmitate, (b) cholesteryl oleate, and (c) cholesteryl linoleate.

As shown in Figure 3.8, the sterol-ester spectra exhibit a trend of increasing molecular ion stability as the number of double bonds in the fatty acid chain increases, leading to a large molecular ion for cholesteryl-linoleate. This is likely due to the higher stability associated with structures containing a greater amount of double bonds as reported by Scholz et al. [129]. Varying the atmospheric dopant did not provide any appreciable differences in the spectra other than slight variances in the relative fragment intensities summarized in Table 3.1. This capability could prove useful in enriched food oil analysis since it involves rapid sample preparation and less energetic charge transfer ionization than APCI [11, 14, 129]. These results also constitute a first application of a desorption technique with APPI for the characterization of these compounds that presents an $[M+NH_4]^+$ species that could be useful in identification studies.

Table 3-1: Primary relative ion abundances for lipid standard compounds.

Compound	Assigned ions (toluene dopant)	Assigned ions (anisole dopant)
Cholesteryl palmitate	$[M-FA]^+$(100), $[2M+H]^+$(3) $[M+NH_4]^+$(2)	$[M-FA]^+$(100), $[2M+H]^+$(5), $[M+NH_4]^+$(1)
Cholesteryl oleate	$[M-FA]^+$(100), $[M+NH_4]^+$(8), $[2M+H]^+$(1)	$[M-FA]^+$(100), $[M+NH_4]^+$(6), $[2M+H]^+$(4)
Cholesteryl linoleate	$[M-FA-H]^+$ (100), $M^{+\cdot}$ (82)	$[M-FA+H]^+$(100), $M^{+\cdot}$(93)
Glyceryl trinonadecanoate	$[M-FA+H]^+$(100), $[M+NH_4]^+$(13), $[FA+C_7H_8+H]^+$(7)	$[M+NH_4]^+$(100), $[M-FA+H]^+$ (92), $[M+C_7H_8O_2]^+$(44), $[M+C_6H_6O]^+$(38), $[M+H]^+$(11)
Glyceryl trioleate	$[M-67]^+$(100), $[M+H]^+$(65), $[M+NH_4]^+$(67), $M^{+\cdot}$(50)	$[M-67]^+$(100), $[M+H]^+$(77), $M^{+\cdot}$(76), $[M+NH_4]^+$(40)
Glyceryl trilinoleate	$M^{+\cdot}$(100), $[M+1]^+$(69)	$M^{+\cdot}$(100), $[M+1]^+$(70)

In contrast to the lack of dopant effects with the sterol-esters, the smaller sterol compound ergosterol, which has been used as a standard for fragmentation and decomposition studies, was found to exhibit significantly different fragmentation patterns based on the atmospheric dopant [81]. As shown in Figure 3.9a-b, anisole (IP 8.2 eV) was found to yield the largest molecular ion signal, whereas toluene (IP 8.8 eV) yielded a

significantly reduced $M^{+\cdot}$ ion. This is most likely due to the larger amount of energy exchanged in the charge transfer collision with toluene. Transition state theory and its variants state that the unimolecular decomposition of a molecule is dependent on its total internal energy [130, 131]. Because the internal energy of the transition state formed in the ion-molecule collision is expected to be higher in the case of toluene (due to its higher IP),

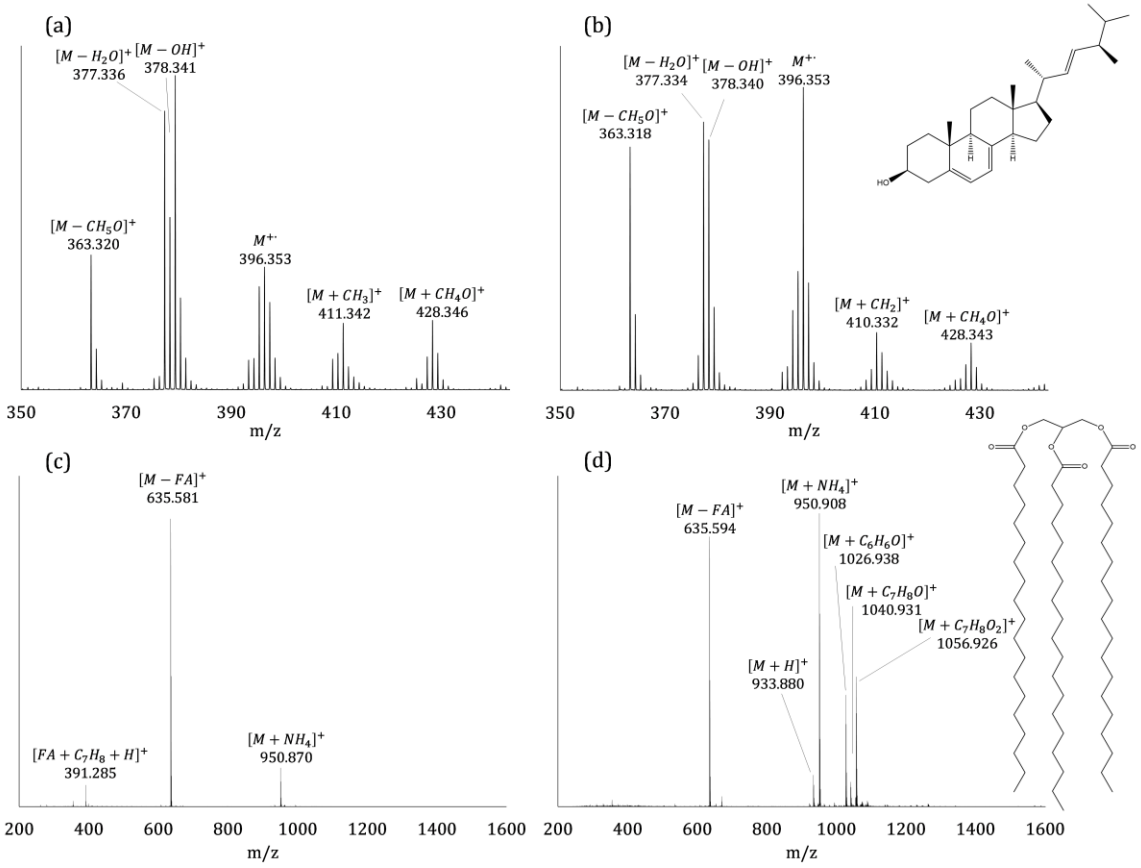

Figure 3-9: Spectra of ergosterol ($C_{28}H_{44}O$, exact mass 396.3392 u) using (a) toluene (b) anisole. Bottom row shows spectra of glyceryl trinonadecanoate ($C_{60}H_{116}O_6$, exact mass 932.8772 u) using (c) toluene and (d) anisole.

this is expected to populate the states corresponding to the formation of the $[M\text{-}H_2O]^+$, $[M\text{-}OH]^+$, or $[M\text{-}O]^+$ with greater frequency. This ultimately reduces the abundance of the molecular ion. The dependence of temperature on fragmentation of the ergosterol $M^{+\cdot}$ ion

was also investigated by lowering the capillary temperature on the instrument from 125° C to 50° C thereby reducing the thermal energy imparted to the molecule and molecular ion. A significant reduction in the $[M\text{-}CH_5O]^+$ fragment at m/z 363.32 was observed with no other noticeable effects. Because this ion at m/z 363 has been observed in the absence of charge transfer in other studies, this suggests that this loss is due to the unimolecular decomposition of the radical cation. Hence, the extent of this decomposition can be controlled by ambient temperature whereas the formation of the $[M\text{-}H_2O]^+$, $[M\text{-}OH]^+$, or $[M\text{-}O]^+$ fragment ions is due to the energy imparted in the ion-molecule transition state complex in the charge transfer ionization event.

3.3.4 Triacylglycerols

Triacylglycerols are known to have relevance in olive oil chemistry, abiotic lipid chemistry, and biological systems [113, 132, 133]. Typically, these compounds also require metal ion adduction for routine analysis with techniques such as ESI [108]. With LIAD-APPI in the absence of metal ions, significant molecular ion information was obtained for all standards tested, except for glyceryl trinonadecanoate using toluene. Glyceryl trilinoleate was observed to have the cleanest spectra containing primarily the $M^{+\cdot}$ as the base peak with small oxidation products for both dopants. Spectra for glyceryl trioleate contained the $M^{+\cdot}$, the $[M+NH_4]^+$ adduct, and the loss of 67 Da (m/z 817) as the base peak for both toluene and anisole dopants. These spectra are shown for both dopants in Figure 3.10. On the other hand, the saturated glyceryl trinonadecanoate primarily exhibited a $[M\text{-}FA+H]^+$ base peak, the $[M+NH_4]^+$ adduct, and a negligible $[M+H]^+$ ion with toluene (IP 8.8 eV) as the dopant (Figure 3.9c). However, with anisole (IP 8.2 eV), the $[M+H]^+$ and $[M+NH_4]^+$ ions were drastically increased relative to the $[M\text{-}FA+H]^+$. The relative

abundances of the assigned species are summarized in Table 3.1. As expected from the results with ergosterol, less conjugated triacyl ions are more stable when produced via a charge transfer reaction in which the internal energy of the charge donor minimizes energy transferred in the ion-molecule transition state complex reducing fragmentation. Additionally, this demonstrates a similar trend of increasing molecular ion stability with greater conjugation in the fatty acid chain as seen with the sterol-esters.

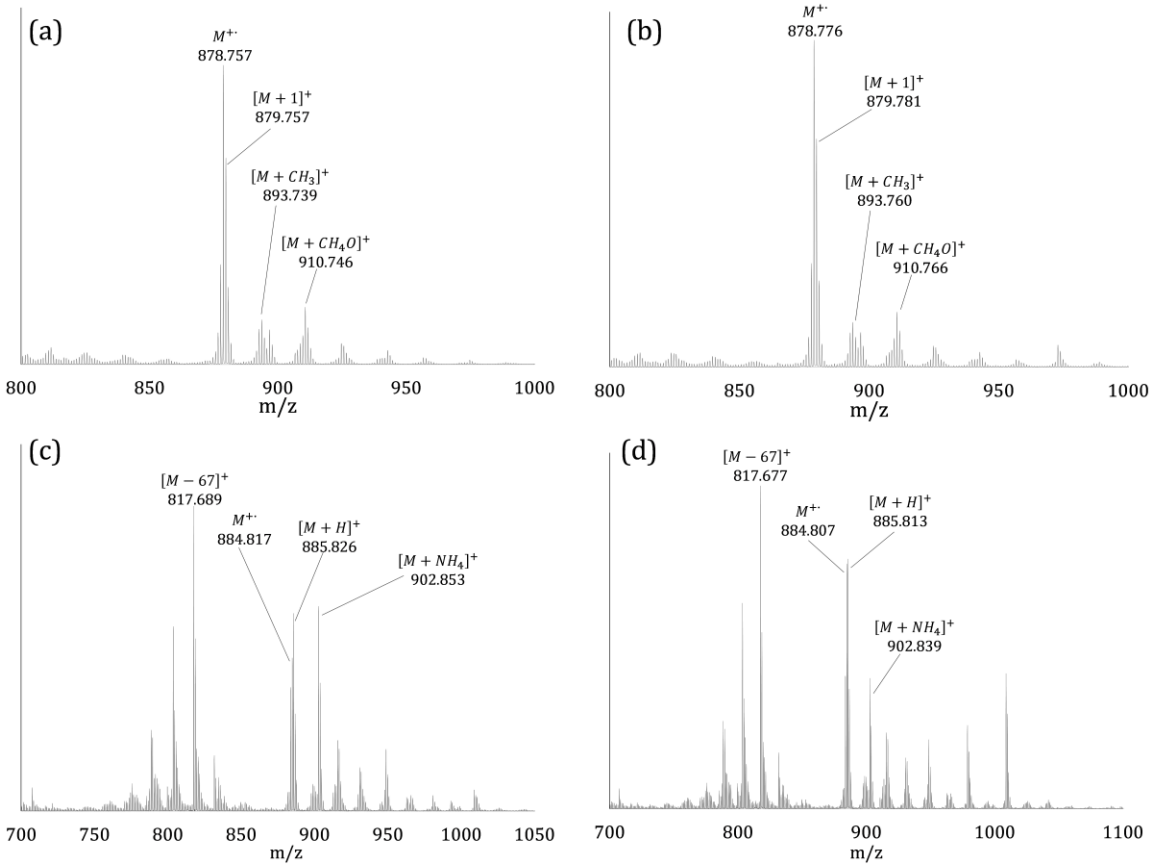

Figure 3-10: Triacylglycerol standards (a) trilinoleate with toluene dopant and (b) anisole dopant. (c) trioleate with toluene dopant and (d) anisole dopant.

3.3.5 Towards Complex Mixtures - EVOO and Chloroform Extracts of Australian Shale

Extra virgin olive oil (EVOO) was chosen to demonstrate complex mixture analysis by LIAD-APPI due to its high concentration of triacylglycerols. [134]. The resulting spectra, shown in Figure 3.11, are dominated by groupings of species corresponding to the triacyl content contained in the oil found in the range of m/z 850 – 910. Smaller species within the 570 – 640 m/z range most likely correspond to the loss of a fatty acid chain from

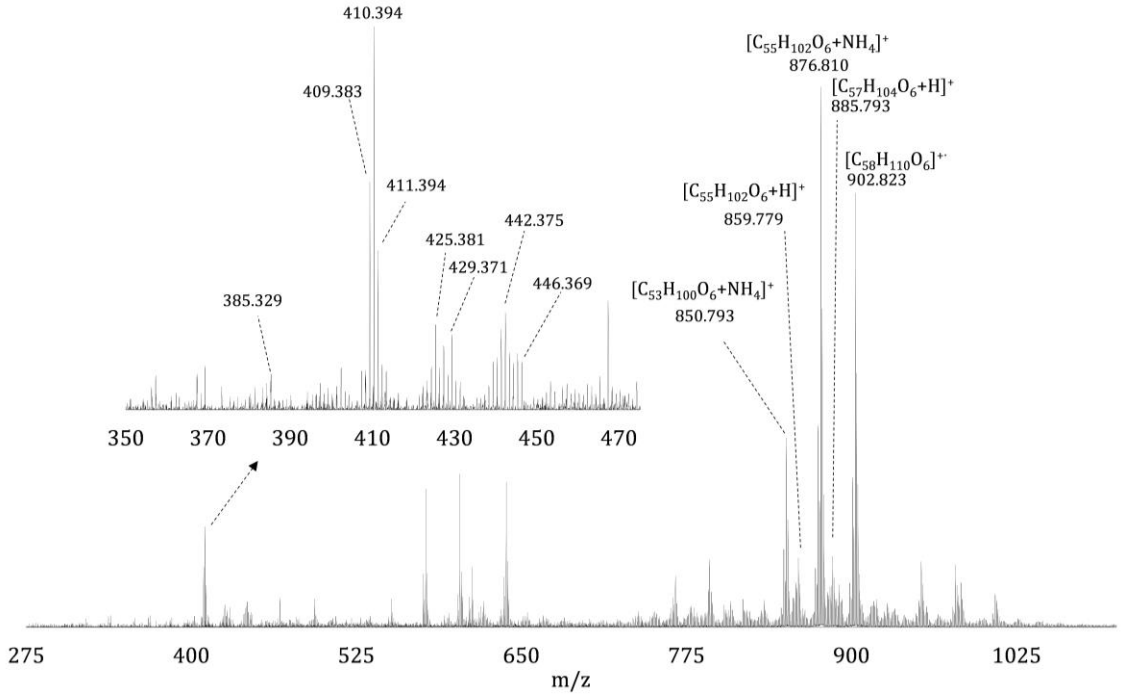

Figure 3-11: LIAD-APPI spectra of extra-virgin olive oil deposited on foil with anisole dopant. Inset shows the region containing the sterol content with tentative assignments summarized in Table 3.2. The region between 850-910 m/z contains signal from the intact triacylglycerols as molecular, protonated, or oxidation adduct ions.

a triacylglycerol and a small presence of diacylglycerols. Additionally, in the 360 –450 m/z range, low abundance signals for plant sterols were observed, with assignments provided in Table 3.2, and found to be consistent with previous direct analysis in real time (DART)

MS work [135]. One peculiarity arises with the observed ion at 902.823 m/z. With the standards, this signal would correspond to the $[M+NH_4]^+$ of glyceryl trioleate, but in similar abundance to the molecular and protonated ions (see Table 3.1). However, in the EVOO spectra, the molecular ion and protonated ion for trioleate are observed in relatively low abundance. Hence, the m/z 902.823 species has been primarily assigned the formula $C_{58}H_{110}O_6$ corresponding to a triacylglycerol with two saturated chains and one singly conjugated chain found using a database search [136]. Though we do note this could also be due to isomers of glyceryl trioleate forming the $[M+NH_4]^+$ in greater abundance or greater availability of ammonia in the complex mixture. This illustrates that LIAD-APPI can be a useful tool for the rapid analysis of olive oil samples, providing information on both the sterol and triacyl content by simply reconstituting in chloroform and depositing on foil. It should be noted that species below m/z 200 were not observed due to the

Table 3-2: Table of assigned sterols to observed signals in extra-virgin olive oil.

The left three columns are m/z values assigned to a particular ion.
* indicates values obtained with toluene dopant.
$[M+1]^+$ corresponds to the ^{13}C isotopic species whereas $[M+H]^+$ corresponds to the protonated species.

$[M-H_2O+H]^+$	$[M+1]^+$	$M^{+\cdot}$	Assigned Molecule	Exact Molecular Mass	ppm error	Exact Fragment Mass $[M-H_2O+H]^+$	ppm error
385.340*	-	-	hydroxy-cholesterol	402.3498	-	385.3470	-18.2
425.381	-	442.375	Erythrodiol, Uvaol	442.3811	-13.8	425.3783	6.35
397.367*	-	-	ß-sitosterol, stigmastanol	416.4018	-	397.3834	-41.3
-	-	397.367	3,5 stigmastadiene	397.3834	-41.3	-	
409.383	-	426.376	Cycloleucalenol	426.3862	-23.9	409.3834	-0.98
-	-	-	Obtusifoliol	-	-	-	
-	-	-	Citrostadienol	-	-	-	
-	-	-	Cycloartenol	-	-	-	
-	-	-	Butyrospermol	-	-	-	
-	-	-	Amyrins	-	-	-	
-	-	-	2,3 epoxisqualene	-	-	-	
-	411.394	410.394	Squalene	410.3913	6.58	-	
429.371	-	446.369	$C_{29}H_{50}O_3$	446.3760	-15.7	429.3733	-5.36

instrument's higher mass tuning for these analyses. Sensitivity could be improved using a more targeted optimization of the ion optics. Regardless, LIAD-APPI offers a straightforward sample preparation and analysis approach without the need for metal ion adduction, desorption matrix selection, or excessively heated surfaces for the analysis of these mixtures. Another benefit is that LIAD-APPI retains the intact molecular species such that a subsequent separatory technique could be used to aid in confirming molecular identification and more generally identify differences in EVOO aliquots due to variance in isomerization and composition. [137, 138].

As an additional example of the analysis of a complex sample, black shale rocks from the Corcoran formation in Australia estimated to be 1.45 billion years old were analyzed. We expected LIAD-APPI to be particularly applicable to desorb and ionize apolar species extracted from these shales due to previous successes with apolar hydrocarbons [1]. The LIAD-APPI mass spectrum obtained from the Corcoran formation rock sample using toluene as an atmospheric dopant is shown in Figure S5. Compounds present most likely include some form of a 31C and 32C hopanoids like those seen in Rybicki *et al.* and a mixture of stearic ($C_{18}H_{36}O_2$), palmitic ($C_{16}H_{32}O_2$), and other

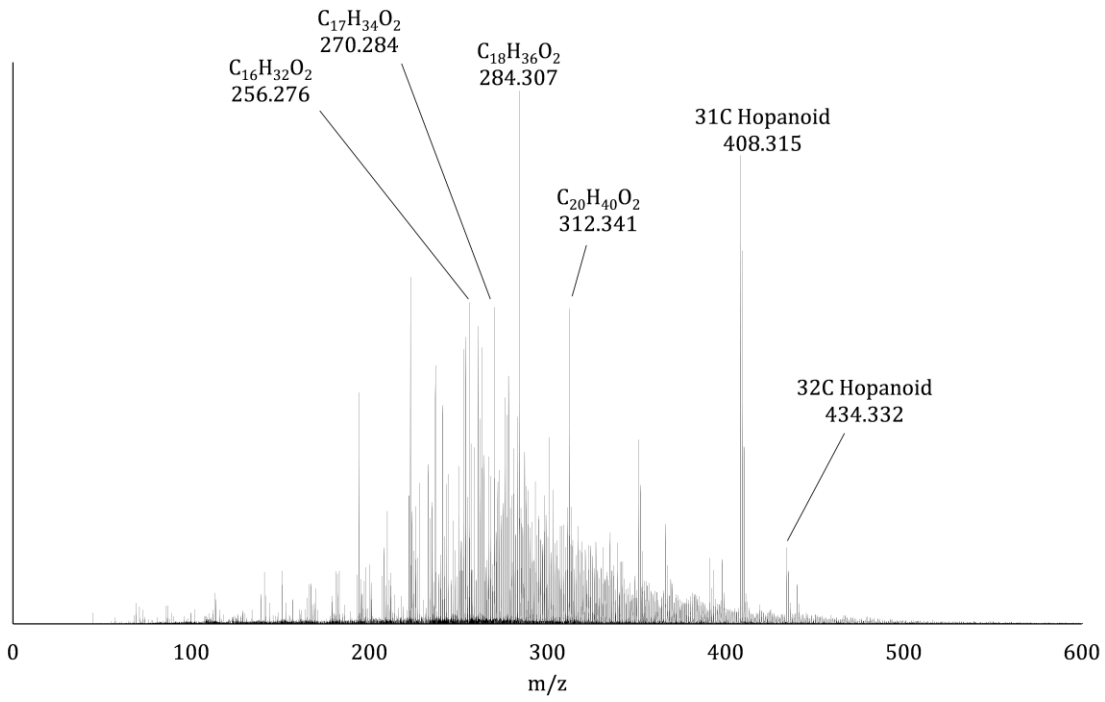

Figure 3-12: Positive mode spectra of the shale chloroform extract dried onto Ti foil using toluene. Notable species are at m/z values of 408 for the 31 C hopanoid and 434 for the 32 C hopanoid.

carboxylic acids [139]. The presence of the indicated carboxylic acids is likely considering the presence of additional deprotonated ions obtained in negative mode with LIAD-APPI. To elucidate the true molecular composition and to fully study the apolar composition of shales, combining LIAD-APPI with a separation technique, such as ion mobility, or MS/MS would be needed [116, 140]. Nevertheless, the successes shown here indicate LIAD in combination with MHCD photoionization or purely MHCD photoionization using a spray based sample introduction approach could be useful for analyzing the apolar organic extracts of many rock types, including meteorites. We expect this capability could

be integrated as a component for future spaceflight instrumentation aiming to observe the lipid composition of extraterrestrial bodies within the solar system [117, 141].

3.3.6 LIAD Mechanism - Oil desorption signal response

Two deposition methods were tested for the EVOO analysis: Deposition of a nebulized chloroform solution via the iMatrixSpray system and drop casting the same solution via pipette. The drop casted standard was found to offer less total ion signal from the sample despite having a greater surface concentration. This is in contradiction to the crystalline samples where greater surface concentration always yields greater signal intensity.

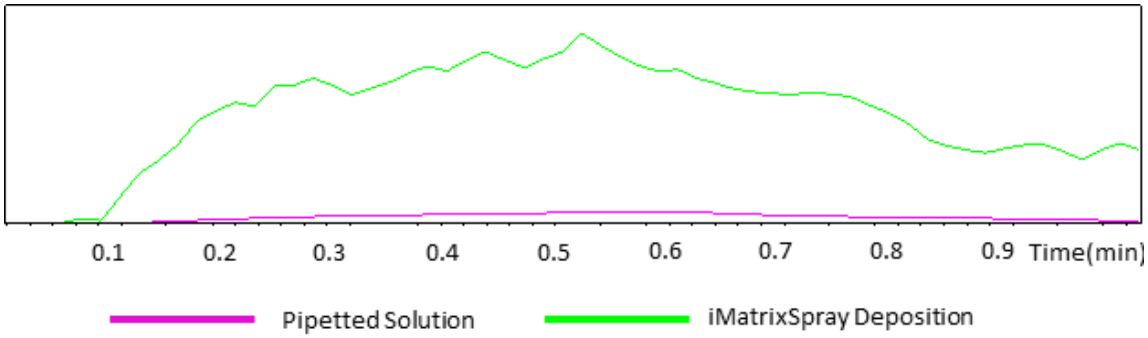

Figure 3-13: Total ion chromatogram for iMatrixSpray deposited EVOO solution versus pipetted/dropcasted solution illustrating enhanced desorption with the iMatrixSpray deposition method.

The drying mechanism in this case can be described as a large droplet slowly evaporating, which leaves a somewhat homogenous film of oil on the surface based on observation. On the contrary, the lower surface coverage obtained with nebulized deposition could be seen as a surface matrix of islands of small, dried microdroplets. Because the desorption yield of LIAD has been suggested to increase based on the extent of interfacial cracking between crystal domains, this could explain the higher sensitivity

with the nebulized deposition[55, 56]. Another explanation could be that for viscous liquid samples, the large amount of material on the foil surface acts as a viscous net to recapture lipid molecules initially ejected near the surface. Of course, with many successive coatings from the nebulized deposition, one would arrive at a homogeneous oil film on the surface. Whichever the case, this demonstrates the point that there is an optimal surface coverage method that maximizes concentration and interfacial domains for viscous liquid samples when preparing LIAD substrates.

3.4 Conclusion

LIAD-APPI with a sweep jet configuration using charge transfer active dopants in an atmospheric pressure environment has been shown to be a viable tool for analyzing dried solutions containing complex low-polarity mixtures. Generally, this approach offers a straightforward surface analysis involving minimal sample preparation with no need for metal ion adducts, desorption matrix selection, or excessively heated surfaces. With the sweep jet configuration, significant improvements in signal response time and decreased detection limits are achieved. These values are in the fmol range, which is close to or approaching values obtained with other atmospheric desorption schemes using laser desorption [25, 142]. We do note these values have potential to be improved further by using a more sensitive mass spectrometer and employing more rigorous flow modeling with optimally engineered designs to fabricate a modular front-end source like those commercially available.

Dopant effects have also been considered where we conclude that particularly labile lipids and sterols are best analyzed using lower IP dopants such as anisole in order to retain the intact analyte molecule in a molecular, protonated or water adduct ion form. Toluene seems best suited for sensitive analysis of sterols if extremely low concentrations are expected and significant molecular ion signal is not needed. In routine analyses of unknowns, it may be best to use a mixture of the two dopants as suggested by Smith et al. [143]. Each dopant provides similar fragmentation and observed abundances for sterol-esters and offers small $[M+NH_4]^+$ signal for the less conjugated species. In addition, fragmentations patterns exhibiting species we have labeled as the $[M-FA]^+$, $[M-H_2O]^+$, and $[M-OH]^+$ all appear to be consistent with sterols and sterol-ester fragmentation patterns reported in studies performed with APPI, DAPPI, and APCI [11, 25, 42, 43]. We suggest that these fragments can be generally expected for ionization sources utilizing an ionized intermediate compound to transfer charge to analyte and other species in the gas phase.

The successes shown here with complex mixtures indicate that LIAD-APPI can desorb and ionize a majority of the apolar compounds in a sample in a single experiment which could be useful in combination with a subsequent separation technique such as ion-mobility. Concretely, the LIAD-APPI technique should be readily applicable to chemical systems in abiotic membrane chemistry, geosciences, meteoritic analysis, biological lipidome studies, and food oil products.

3.5 Acknowledgments

We thank David Deamer and Andrew Knoll for providing a black shale sample from the Australian Corcoran Formation. This work was supported by the NSF and NASA

Astrobiology Program under the NSF Center for Chemical Evolution grant number CHE-1504217. The Bruker Q-TOF mass spectrometer was acquired through NSF grant CHE-0923179.

3.6 Supplemental Sphingomyelin Results

This section includes data not discussed in the main body of Chapter 3 for the sphingomyelin (SM) egg yolk extract mixture obtained from Sigma-Aldrich.

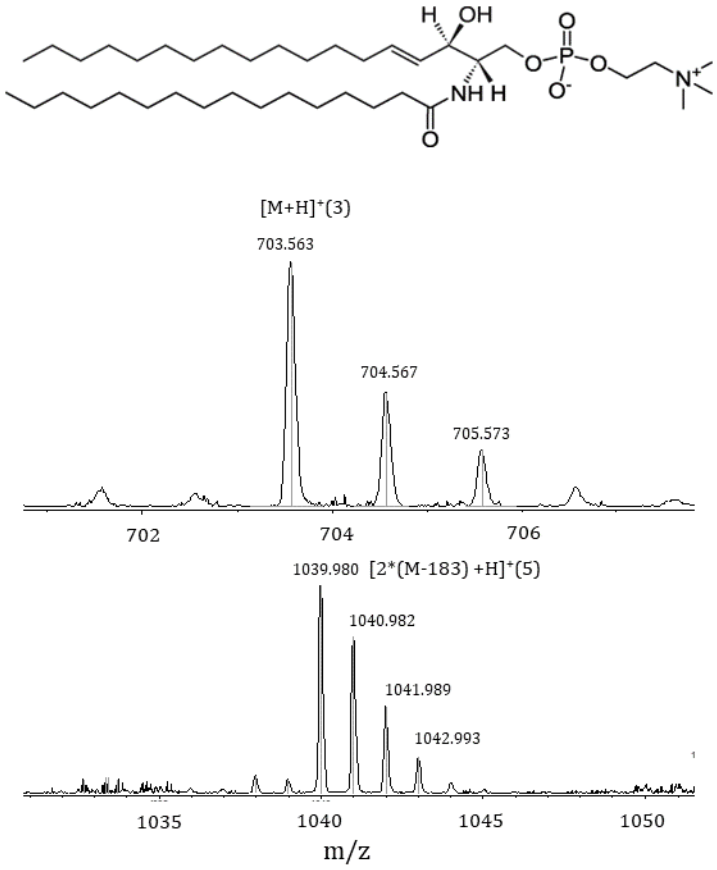

Figure 3-14: Spectra of 16:0 Sphingomyelin (SM) obtained from a surface concentration foil of ~ 50 nmol cm^{-2} with LIAD-APPI in positive mode. Top spectra demonstrates the protonated molecular ion is retained though in a very small relative abundance (~ 3%). Bottom spectra indicates the protonated dimer formed from the loss of the polar head of the lipid.

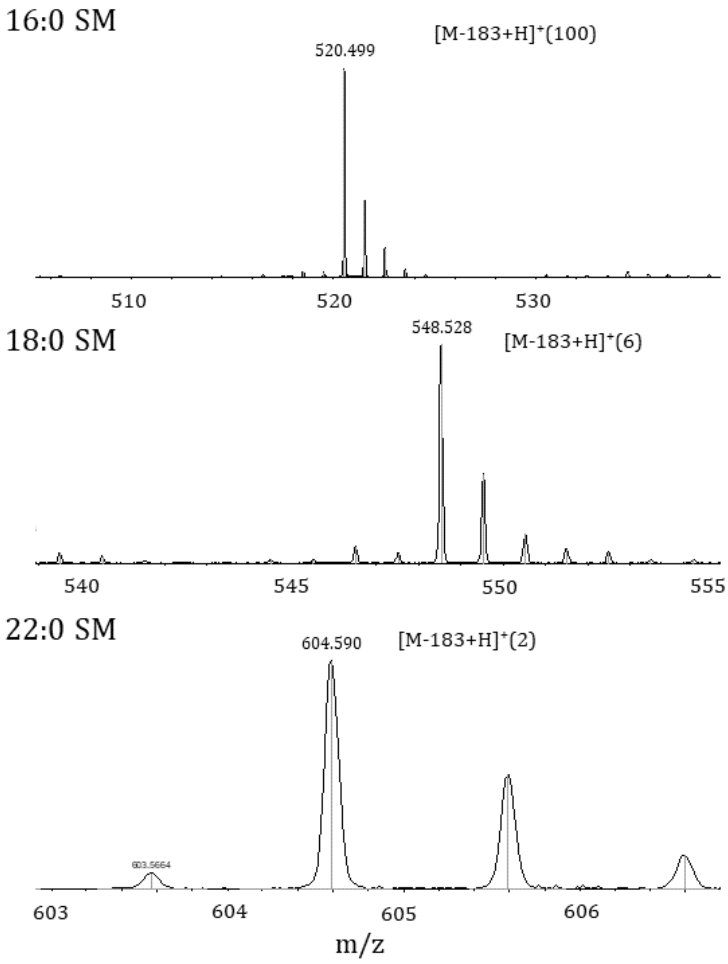

Figure 3-15: Spectra indicating the presence of all major SM components in the egg yolk extract mixture given by the protonated loss of the polar head fragment [M-183+H]$^+$ species in positive mode. These species appear in similar proportions to their reported abundance in egg yolk samples.

CHAPTER 4. ANALYSIS OF CRUDE OIL AND SHALE ROCK HYDROCARBONS VIA LASER-INDUCED ACOUSTIC DESORPTION ATMOSPHERIC PRESSURE PHOTOIONIZATION FT-ICR MASS SPECTROMETRY

4.1 Introduction

4.1.1 Petroleum

Petroleum complex mixtures are typically found in geological formations dating back hundreds of millions if not billions of years. Compounds comprising these mixtures are known to be derived from the decomposition of ancient organisms buried under intense heat and pressure for these periods of time. Because of the many different geological conditions that exist to produce petroleum, there is a wide variety of chemical compositions that can occur. Therefore, it is important to understand the processes leading to its formation and what types of petroleum different conditions may yield.

To begin describing the chemistry of the formation of petroleum we start with the death of ancient organisms typically consisting of large quantities of algae, zooplankton, or plant matter. In order for these to decompose into what we would find today as petroleum or fossil fuel, they must first settle into some oxygen deprived environment. A primary example of this would be algae dying off and settling to the bottom of some stagnant water formation such as a marsh or lakebed. Beginning at a depth of ~ 1 – 10m, anaerobic bacteria in this environment act to process the dead matter, liberating nitrogen from amino acids,

producing methane from saccharides, and removing sulfur in the form of hydrogen sulfide. The distribution of the products at this stage is dependent on the specific geological environment, thus the resulting petroleum chemistry can vary significantly. For example, shale oil originating from a more oxidative environment has been reported to have a greater O/C average atomic ratio than other sources [144, 145]. Nevertheless, the anerobic products, in addition to products from hydrolysis, recombine to form fulvic and humic

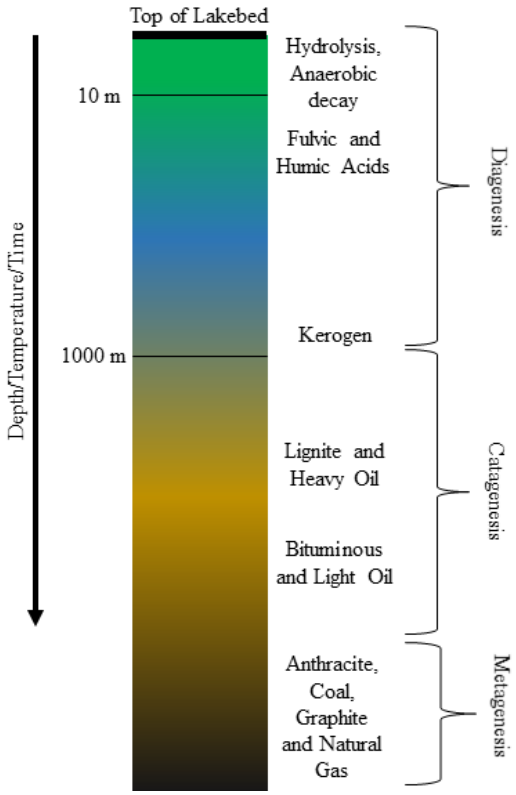

Figure 4-1: Generalized diagram of petroleum formation. Note that some sources are formed from chemical mixing and reaction with sources perceived to be from other stages of formation. For example, with bitumen formation a light oil is evaporated or degraded, sometimes in the presence of kerogen.

acids containing compounds with molecular weights extending up to the range of 10^4 Da [146, 147]. This first step of petroleum formation is typically referred to as the first phase of diagenesis or aerobic decay. The subsequent phase to aerobic decay taking place at

depths greater than 10 m form kerogen, a high molecular weight substance with no specific chemical formula originating from algal, plankton, and plant sources or types I, II, and III kerogen respectively [148]. In general, the structures of molecular kerogen species are considered to be very complex with ring-like structures sometimes relating to their biological origin [149]. Including early anaerobic decay, this entire process leading to kerogen formation is collectively known as diagenesis. However, final stages recombining the humic and fulvic species to form kerogen are not well understood.

As the kerogen proceeds to depths exceeding 1,000 m or often much greater, it is converted to petroleum in a process known as catagenesis. At these depths, temperature and pressure are sufficient for kerogen to undergo rearrangement through primaily radical chemical reactions. Because these are in the absence of external hydrogen sources, these reactions proceed to generate two main classes of products: hydrogen rich (high H/C ratio) or hydrogen deficient (low H/C ratio) compounds. Various temperatures, pressures and chemical environments determine the ultimate result of these reactions, but generally catagenesis is defined to occur until the H/C ratio has reached 0.5 [150]. After which, some define the stage leading to increases of aromaticity, or graphitic coal formation as metagenesis. These divergent pathways are responsible for forming either coals (low H/C) or oils and natural gas (high H/C).

Particularly interesting to this work are the formations of heavy crude oils and crude bitumen or oil sands. Heavy crudes are typically found in liquid form in a subterranean reservoir whereas bituminous sources are in a solid form underground typically consisting of a fraction with similar properties to heavy crude contained in a sand or coal-like medium [151]. There are many postulated pathways for the formation of bituminous sources

involving a combination of evaporation of light oils, bacterial decomposition of light oils, and geological shifting of oil wells to trap heavy oils in porous media [152, 153]. Because the solid-emulsion contains the petroleum product of interest, bitumen must be extracted using heat, steam, or some solvent. Whereas for heavier crude oils, the liquid contained in the reservoir can transition to a quasi-solid at atmospheric conditions. Hence for either a heavy crude oil or bitumen source, the resource of interest is the extremely viscous, tar-like substance. This is in contrast to light oils which flow freely under atmospheric conditions. Typically, these will contain a high degree of heteroatom compounds mainly consisting of oxygen, nitrogen, and sulfur. Some studies have even identified vanadium porphyrins in Orinoco belt heavy crude oil [154]. Gaining comprehensive information on samples from these sources is difficult and often requires several forms of analysis to resolve the variety of components. Concretely, these mixtures are known to be some of the most chemically complex forms of petroleum. As a result, it is important to understand their chemical composition as certain segments of the petroleum industry begin to rely increasingly upon these unconventional sources.

So as one may see, an extremely diverse set of scenarios can lead to the formation of petroleum. These conditions yield a rich variety of sources each with a richly complex chemical composition. At the risk of over generalization, a chart is shown in Figure 4-1 to summarize the products formed by the processes described above and is based on information from references [148, 155].

4.1.2 Fourier-transform ion-cyclotron resonance (FT-ICR) mass spectrometry

The field of petroleomics has benefited immensely from using mass spectrometry to identify the incredibly complex and vast distribution of compounds contained in crude oils and other petroleum fractions, or the petroleome. Historically, chemists and geologists relied upon wet chemical methods, spectroscopy, gas chromatography (GC), and high-pressure liquid chromatography (HPLC) to identify compounds within the petroleome [156-160]. Given newer technologies, the extent to which the petroleome can be defined can be taken to new heights enabling more accurate predictions on petroleum utilization, process improvements, and environmental impact response. As an introduction, we will explore the technologies elucidating these richly complex chemistries.

As a natural match for the analysis of the petroleome, the invention of ultrahigh-resolution mass spectrometry methods now allow for tens of thousands of compounds to be identified in a single analysis [161]. This has largely been afforded by the development of the state-of-the-art Fourier-transform ion-cylcotron resonance (FT-ICR) mass spectrometer [162]. To illustrate how these instruments achieve such high resolution and accuracy, we must first understand the force (F) experienced by a point charge in a static magnetic field given by equation 26.

$$F = qv \times B \tag{28}$$

Where q is the charge, v is the velocity, and $B$is the magnetic field strength typically given as teslas (T). As a result, the charge in the magnetic field rotates about the axis of the magnetic field. Using Newton's second law for centripetal force, this rearranges to show:

$$\omega_{freq} = \frac{\omega}{2\pi} = \frac{qB}{2\pi m} \quad (29)$$

Where ω_{freq} is the cyclotron frequency, ω is the angular velocity, and q/m is the inverse mass-to-charge ratio (m/z). However, to obtain a signal from an ion's rotation in the FT-ICR cell, it must first be "excited "to an appropriate cyclotron radius by radio-frequency (rf) excitations via an oscillating electric field such that the current induced by their motion can be recorded [163, 164]. The raw signal is a decaying oscillatory current as a function of time which can be decomposed into the individual frequencies that comprise it via a Fourier-transform. The Fourier-transform takes the raw oscillatory signal in the time domain and maps it to the frequency domain. These individual frequencies from each ion can then be related to the m/z as described above. The ultimate result of this instrumentation and analysis workflow is an extremely high peak resolution in the resulting mass spectrum with state-of-the-art instrumentation reaching mass-resolving powers of 2.7 x 10^6 (full-width half maximum FWHM estimation) at m/z 400 and sub 100 parts-per billion (ppb) mass accuracies [161]. These capabilities are particularly powerful for petroleum analysis given the incredible amount of compounds present with very small mass differences. Extremely minute mass differences typically cannot be resolved by other forms of mass analysis. A typical mass difference for petroleomics includes the SH_4 difference from C_3 with a mass difference of 3.4 mDa which can be resolved with orbitrap mass spectrometers [165]. An extreme example would be mass differences of 0.53 mDa differences between $H_8S_1{}^{34}S_1$ and C_5N_1 species, a difference only separated by the highest resolution FT-ICR instruments [161, 166].

4.1.3 Ion-source technology in petroleomics

In addition to complicating m/z separation, the oxygen, nitrogen, and sulfur species, as well as higher C number species, are not amenable for GC based analysis due to their low-volatility. This has brought electrospray ionization (ESI) and atmospheric pressure photoionization (APPI) forth as the atmospheric pressure ionization (API) techniques of choice for these types of analyses [167-169]. However, the large amount of heating required for desolvation, often reaching 300° C, can induce thermal degradation of more labile molecular compounds. While great for non-polar hydrocarbons and sulfur heteroatom species, APPI typically requires a flow rate of 50 µL min^{-1} for petroleum analysis introducing a heavy mass load on the spectrometer. Demonstrations of micro-APPI source technology offered a solution to this issue though this still required ~300° C vaporizing temperatures [170]. Nevertheless, APPI is the technique of choice for characterizing the non-polar fraction of crude oils. ESI in particular has known limitations regarding non-polar species though some have found ESI analysis workflows for sulfur heteroatom compounds in petroleum albeit requiring derivatization [169]. Recent work has aimed to characterize the extent of ion suppression in petroleum analysis by ESI [171]. These challenges have sparked some interest in developing other techniques to desorb and ionize a range of petroleum species in as non-selective a manner as possible.

Desorption electrospray ionization (DESI) has been shown to be an effective method for ionizing the water-soluble components in a heavy sweet (low-sulfur content) crude oil and exhibited best results for a electrospray jet formed from a 70:30 acetonitrile/toluene mixture [172]. Though a great deal of peaks were obtained, this approach appears to still be limited to the polar fraction of crude oil. Another technique exhibiting successful petroleum analysis combined laser-induced acoustic desorption (LIAD) with atmospheric

pressure chemical ionization (APCI) [87]. LIAD, as already mentioned, is well established for its ability to desorb virtually any mass or class of molecular species and even larger species such as cells and microparticles [59, 61]. LIAD is typically accomplished by applying a laser pulse with power density > 10^8 W cm^{-2} to one side 5-20 μm thick foil with an analyte film on the opposite side. Though there are still unanswered questions surrounding the true mechanism of LIAD, the analyte film cracking induced by the rapid restructuring of the foil surface is thought to generate the gas phase species observed [51, 55, 56]. This hypothesis is generally supported by observations in other work with LIAD under the conditions described [173, 174]. When combined with APCI, Nyadong et al. were able to demonstrate clean spectra of saturated hydrocarbons consisting mainly of the hydrogen-abstracted cation ($[M-H]^+$) for high flow rates of O_2 carrier gas [47]. Preceding this work, others had also demonstrated petroleum analysis by LIAD followed by electron ionization (EI) and chemical ionization (CI) in vacuum [60]. Though an important step in demonstrating LIAD to be useful for oil analysis, softer ionization techniques such as API, would be preferable. One such technique was demonstrated by Corilo et al. known as easy ambient sonic-spray ionization where the petroleum is deposited directly on an inert surface, desorbed by a sonic jet of charged droplets, and subsequently ionized [175]. This approach gave a simple workflow to obtain an appreciable number of peaks (~6000), though primarily from the polar constituents of crude oil.

To leverage the benefits of a few of the ion source technologies described, this work describes the application of LIAD-APPI for petroleum analysis enabled by FT-ICR mass spectrometry. This is the first instance of LIAD-APPI coupled to an FT-ICR mass spectrometer. Furthermore, APPI is accomplished through the use of a novel micro-hollow

cathode discharge device capable of producing the necessary vacuum-ultraviolet (VUV) radiation for photoionization [1, 88]. LIAD-APPI has previously been demonstrated as an effective means for desorbing and ionizing very apolar and labile lipid species as well as complex mixtures like extra-virgin olive oil and non-polar shale extract [2]. These successes suggest LIAD-APPI is an ideal candidate for petroleomics analysis. Furthermore, this approach boasts the benefits of low source temperatures, elimination of high mass load flow injection, ease of sample preparation, and ionizing a more representative distribution of compounds in a single analysis via APPI.

4.2 **Experimental**

4.2.1 Samples and Materials

Titanium foil (99.8% metals basis, 12.7 µm thickness) for the LIAD experiments was purchased from Alfa Aesar (Ward Hill, MA, USA). All hydrocarbon standards (perylene, coronene, squalene, decanoic acid, stearic acid) and molybdenum for the MHCD electrodes were obtained from Sigma Aldrich (St. Louis MO, USA). The electrodes were fabricated with ~100 µm holes via fine tip drilling. The atmospheric dopants used, ReagentPlus® 99% anisole and OmniSolv® 99.9% toluene, were also purchased from Sigma Aldrich. High purity lithium fluoride windows were custom ordered from Crystran (Poole, Dorset, UK) for the MHCD device. Macondo well oil was purchased from the National Institute of Standards and Technology (NIST) as standard reference material (SRM) 2779 and was sampled directly off of the well-head at the time of the Deepwater Horizon disaster [176]. An Azerbaijan heavy “sweet” aromatic-naphthenic (AH) crude oil and a Venezuelan heavy “sour” (VH) crude oil were purchased from ONTA, an educational

geology company (www.onta.com). A Basinal black calcareous (ca 550 Ma) shale listed in collection as KG91-70 from the Khatyspyt formation was provided as a gift from David Deamer and Andrew Knoll as an example of an unconventional petroleum source analysis.

4.2.2 Sample preparation

Standard samples were prepared dissolving a mix of perylene, coronene, squalene, decanoic acid, and stearic acid diluted in dichloromethane to concentrations of 594 µM, 999 µM, 7.11 mM, 3.72 mM, and 703 µM, respectively, and spotting 50-100 µL aliquots of the solution onto the Ti foil. Preparation of the Macondo well oil involved emptying the 1.2 mL of crude from the sealed ampoules into clean 10 mL volumetric flasks and diluting with hexane to create a stock solution. One milliliter of this stock solution was taken and diluted again to 10 mL with hexane yielding ~ 10 mg/mL solution. 300 µL of this solution was deposited across a foil surface area of ~ 5 cm^2 yielding a somewhat homogenous surface concentration though areas of higher accumulation were observed. The AH crude oil was prepared in the same manner to yield a 10 mg/mL solution and depositing 300 µL across the foil surface with similar homogeneity to the Macondo well samples. VH crude oil was prepared as a 10 mg/mL solution as well albeit using toluene as the solvent and only using 100 µL for foil deposition. The 550 Ma shale was prepared by first crushing the large rock pieces in a cleaned aluminum foil wrap with care taken to ensure none of the rock was exposed. The resulting small fragments, roughly the size of a rice grain, were then ground to a dust for 30 ~min with a clean agate mortar and pestle. The resulting dust was then extracted with toluene given it's efficacy as a shale extraction solvent [177]. 100 µL of the clear extract liquid was deposited on the foil for analysis.

4.2.3 LIAD-APPI Instrumentation

The VUV radiation required for photoionization was generated by the micro-hollow cathode discharge (MHCD) as previously described [1, 88]. Specifically, we generate hydrogen Lyman-α emission (121.6 nm, 10.2 eV) via a plasma gas mixture containing 4% H_2 in neon at a flow rate of 40 sccm at 760 Torr to reduce impurities [75]. This is expected to efficiently generate the hydrogen Lyman-α line via a near-resonant energy transfer process initiated by the neon excimer's collision with H_2 [73]. Flow rates of plasma gases were controlled by two FMA-5500 series MFCs from Omega Engineering (Stamford, CT, USA). Voltage was applied to the MHCD electrodes through the use of Stanford Research Systems model PS350 power supply (Sunnyvale, CA, USA) leading to applied voltages between -1000 and -1180V where typical operation included a current of 10 mA and an operating voltage of -1130V. The MHCD device itself is the same as a previously designed device by our group and is discussed in more detail elsewhere [2]. The dopants used in these experiments were introduced at a flow rate of 9.75 μL min^{-1} and were nebulized by a nitrogen gas flowing though the Agilent nebulizer needle via a pressure driven flow set at 1 bar on the Bruker instrumentation software. The needle was positioned at a 0.75 cm distance and centered with the inlet axis resulting in expected flow fields like those calculated in reference [2]. Figure 3-2b in Chapter 3 illustrates the LIAD-APPI configuration used. LIAD was accomplished through the use of an Opotek Opolette 2731 laser system configured to transmit the primary 1064 nm beam at a 20 Hz pulse rate. Laser intensity was limited to 75% by the Opotek software giving a time averaged power intensity of 550 mW or a power density of 0.6 x 10^8 W cm^{-2}. FT-ICR data acquisition and the laser pulse sequence were started simultaneously to ensure peak signal was observed

from a single desorption spot. For more on the time resolved LIAD-APPI signal dynamics see reference [2].

4.2.4 FT-ICR Mass Spectrometry Instrumentation

The FT-ICR mass spectrometer used in these studies was a Bruker solariX XR with a magnetic field strength of 12 Tesla (T). The instrument was pre-calibrated for LIAD-APPI experiments using the ESI source and a standard tuning mixture of sodium trifluoroacetate (NaTFA), ensuring mass errors < 500 ppb across a 150-1500 m/z range or 70-1200 m/z range where applied. An example of the accuracies achieved with this configuration for the provided reference masses is shown in Section 4.6, Table 4-2.

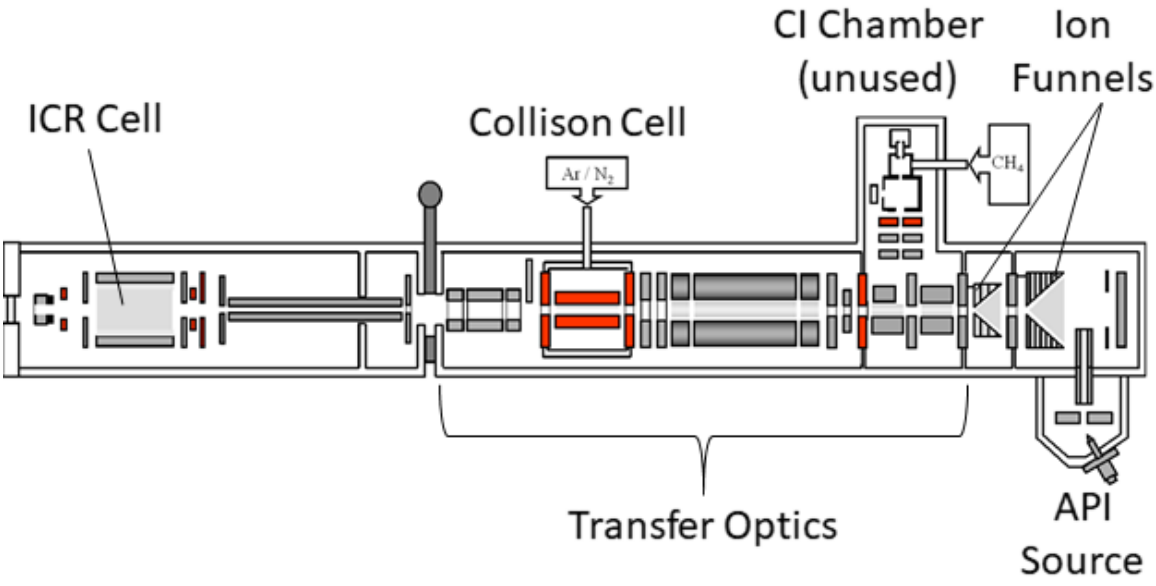

Figure 4-2: Schematic of the Bruker solariX XR 12 T FT-ICR mass spectrometer and optics. Our LIAD-APPI source was coupled to the API source interface by removing the source chamber door (Adapted from Bruker Compass © Software Suite, Bruker Daltonik GmbH, Bremen, Germany).

Settings on the Bruker API Source interface for LIAD-APPI were a drying temp of 120° C, drying gas flow rate of 5 L min^{-1}, capillary voltage of -50 V, and endplate offset voltage of 50 V. Ions were transported from the ambient source through a glass capillary and a series of rf multipoles and ion optics (Figure 4-2).In addition, all analyses on this instrument were performed via a sweep rf excitation of the respective ion cyclotron frequencies [164]. This was used to record the signal in a general broadband method.

4.2.5 Data Analysis

The software used for these studies was the Bruker Compass © software suite (Bruker Daltonik GmbH, Bremen, Germany) which controlled many of the underlying signal-to-noise (S/N) calculations, mass error, free-induction decay (FID) processing, and compound assignment calculations via proprietary algorithms. Sixteen scans were recorded and averaged by the acquisition software for each of the complex mixture analyses with accumulation times at either 0.1-0.2s. Magnitude mode profile spectra were processed with no data reduction for subsequent internal calibration. Homologous series observed to be present were identified for each crude oil spectrum and, given the confidence in the ESI calibration, were used to internally calibrate across the range of interest using a quadratic calibration model. Compound assignments were elementally constrained according to a standard for petroleum samples: Given a general formula, $C_c H_h N_n O_o S_s$, where c and h are

unlimited $0 \leq n \leq 5$, $0 \leq o \leq 10$, and $0 \leq s \leq 2$ [178]. Additionally, formulas yielding an error > 500 ppb were discarded unless otherwise noted.

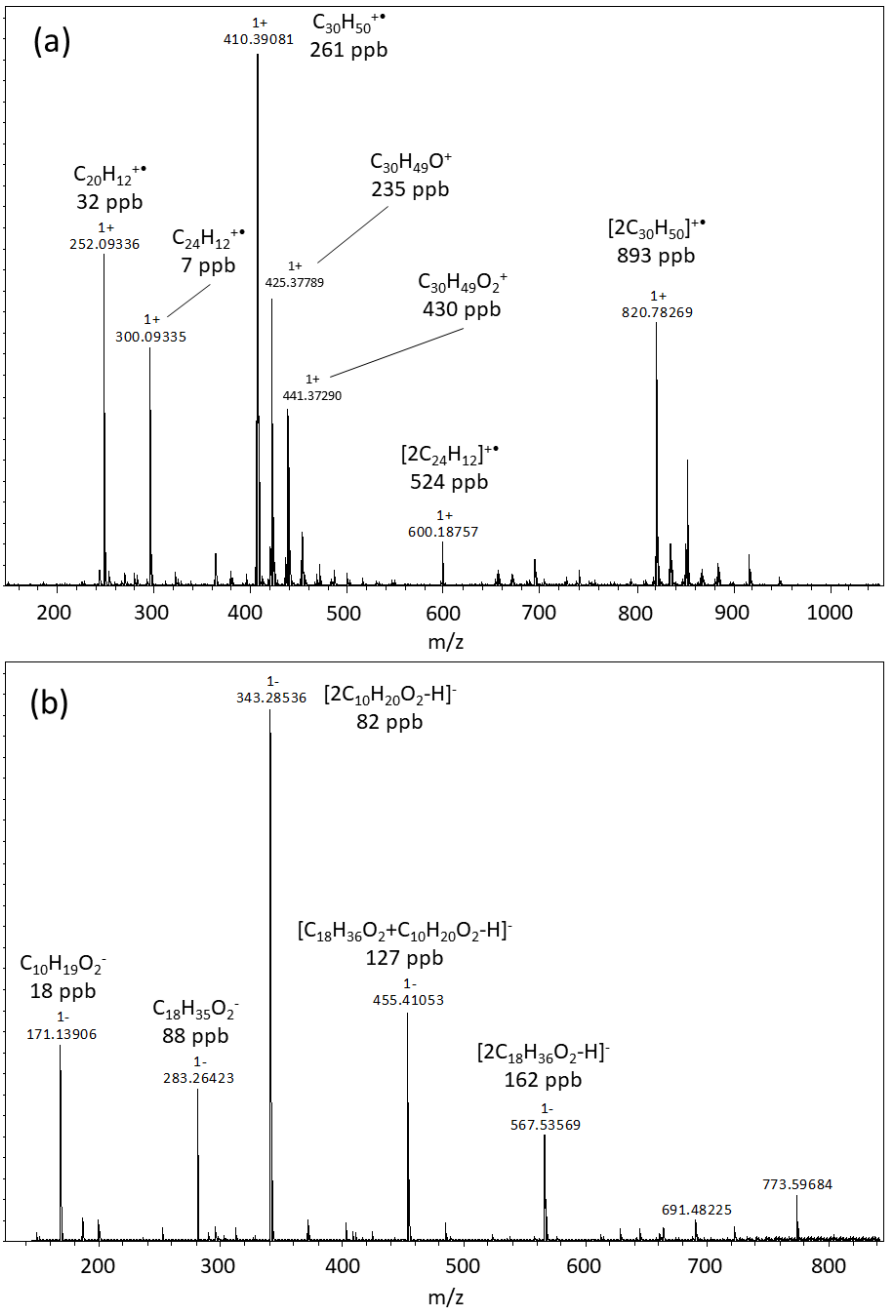

Figure 4-3: LIAD-APPI positive mode spectrum (a) and negative mode spectrum for (b) for a mixture containing coronene, perylene, squalene, decanoic acid, and stearic acid using anisole as a dopant. The carboxylic acids appear as deprotonated ions in negative mode where as the non-polar hydrocarbons appear as radical cations in positive mode. Shown below each assigned formula is its respective mass error with no internal calibration.

4.3 Results and Discussion

4.3.1 Hydrocarbon Standards

To gain an understanding of performance on non-polar mixtures, we tested the LIAD-APPI FT-ICR system on a mix of perylene, coronene, squalene, decanoic acid, and stearic acid diluted in dichloromethane. The resulting positive mode spectrum taken with anisole as the dopant shown in Figure 4-3a reveals a molecular radical cation ($M^{+\bullet}$) for coronene, perylene, and squalene as well as squalene and coronene dimer radical cations ($[2M]^{+\bullet}$). Relative abundances of the respective $M^{+\bullet}$ species did not reflect their concentration as prepared most likely due to this dimer formation. It is noted that as mixtures become more complex and individual analytes more dilute, the dimers are expected to not be observed due to low abundance or because the larger number of unique ions formed act to ionize neutrals before they are scavenged by clustering. This appears to be consistent with our results shown later with crude oil distributions with no clear compound assignment relations observed and a lack of a high abundance m/z distribution peaking at larger m/z's. Also shown in Figure 4-3 is the mass error obtained for the species observed without internal calibration. This is indicative of how well the instrument maintains mass calibration and accuracy as sources generating ions with slightly different energy distributions are measured. In general, this reveals a sub-ppm mass error which increases with increasing mass. Nevertheless, this result provides confidence that masses obtained from the instrument after calibration with the ESI source are close enough to internally calibrate post-analysis or perhaps even directly analyze.

In addition to the positive mode species, the deprotonated carboxylic acids ($[M-H]^-$) and their array of dimers were observed in negative mode (Figure 4-3b). This gave similar results to the positive mode spectra regarding mass accuracy and abundance obscuration by the dimer formation. This serves as a good demonstration for LIAD-APPI in negative mode for carboxylic acid species known to be observed in many geological and astrogeological samples [179, 180].

Despite the positive results discussed above, a standard mix containing higher alkanes triacontane and hexatriacontane combined with cyclic alkane 5α-cholestane offered no observed signal from these species using either toluene or anisole as a dopant. This is generally consistent with other observations on APPI as an ionization technique [181]. With these saturated hydrocarbon species, it has been demonstrated that LIAD/APCI can successfully generate the hydrogen-abstracted quasi-molecular cation $[M-H]^+$ in a stable manner with an oxygen reagent gas [47]. This is also consistent with the proposed mechanisms for formation of $[M-H]^+$ species given by Marotta et al. involving reaction pathways dependent on the ionization of O_2, H_2O, or N_2 [182]. Therefore, because APPI does not ionize species with IP > ~ 10 eV, it is apparent that this is the cause for the unobserved $[M-H]^+$ species. For completeness, it is noted that reactions with cationic saturated hydrocarbons have also been attributed to forming $[M-H]^+$ which may offer a new area of atmospheric dopant exploration to extend APPI to these species [183].

4.3.2 NIST SRM 2779 – Macondo well oil

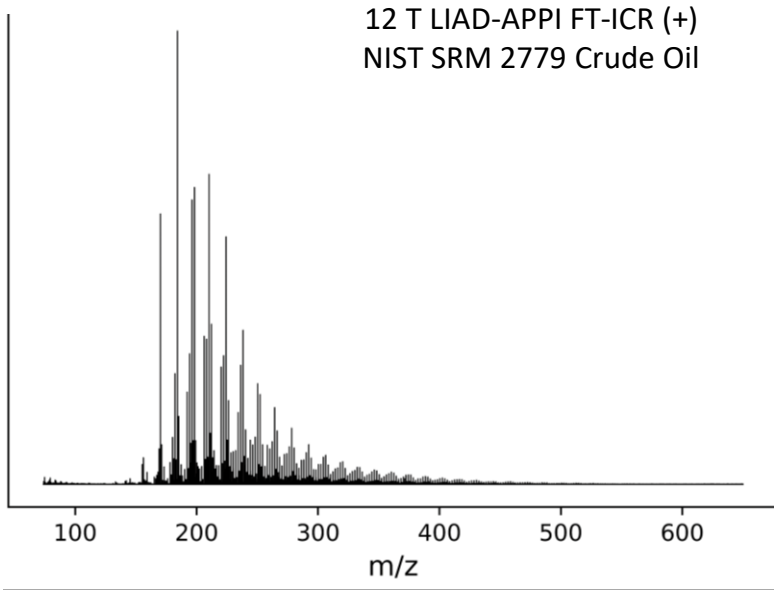

Figure 4-4: Positive mode spectrum with toluene dopant of the Macondo well oil sample indicating a lower m/z distribution consistent with a light oil character.

LIAD-APPI lends itself to apolar mixtures containing a variety of compound and therefore lends itself quite readily as a tool for crude oil analysis. To test the system on a known crude oil sample, we chose the NIST SRM 2779 crude oil recovered directly from the *Deepwater Horizon* disaster. The source of SRM 2779 is known as the Macondo well and the oil product is known by the petroleum industry as Mississippi Canyon Block 252 (MS252). It is generally characterized as a light, "sweet" oil. Light refers to the high relative abundance of lower mass organic compounds when compared to heavier crudes and is in a freely flowing liquid form at atmospheric temperature and pressure. "Sweet" designates this petroleum source to be low in sulfur content. Understanding the composition of these oils can better enable us to respond to their environmental impacts in

the aftermath of disasters like *Deepwater Horizon*. Shown in Figure 4-4 is a spectrum via

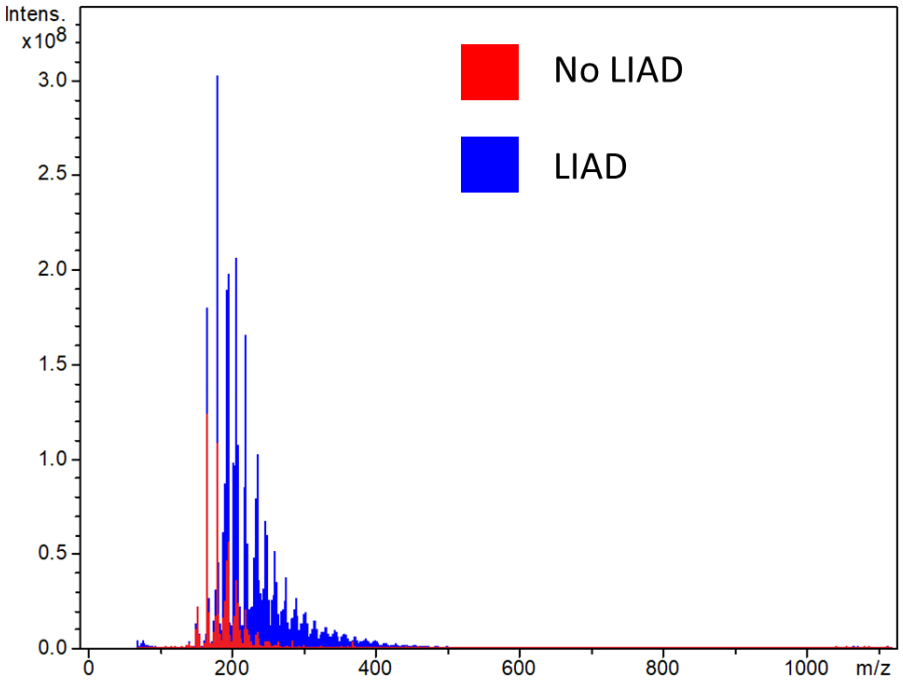

Figure 4-5: Comparison spectra. Signal obtained with no LIAD shown in red. Higher masses are liberated from the surface when LIAD is used and those already desorbing from flow increase in abundance.

LIAD-APPI FT-ICR MS using toluene as a dopant. To illustrate the effect of LIAD, Figure 4-5 is provided highlighting the increase in abundance of already present lower masses (due to high volatility or pick-up by the sweep jet) and appearance of higher mass species with LIAD enabled. Based on our previous predictions of a swirling vortex at the inlet for this source, the peaks observed in the absence of LIAD would suggest that some species are being lifted off via a mechanism similar to desorption atmospheric pressure ionization (DAPPI) [2, 27]. Regardless, Figure 4-5 illustrates the need for LIAD if a maximal amount of information is to be obtained.

Using a toluene dopant, this approach revealed a peak list containing ~22,000 peaks at S/N > 4. Spectra were internally calibrated using a series of alkylated triene hydrocarbons determined to be present through careful analysis of initial results. Compound identification was performed after the quadratic internal calibration with the Compass © software. The formula assignments were limited to a relative intensity threshold corresponding to a S/N = 4 and assignments with mass error > 1 ppm were discarded. Best results yielded an average mass error of -5.5 ppb, (root-mean-square) rms error of 235 ppb and 1173 assigned elemental formulas. A histogram of mass errors and plot of error vs. observed m/z is shown in Figure 4-6. The number of formula assignments is far from other studies on Macondo well oil by APPI however the mass errors obtained are comparable to

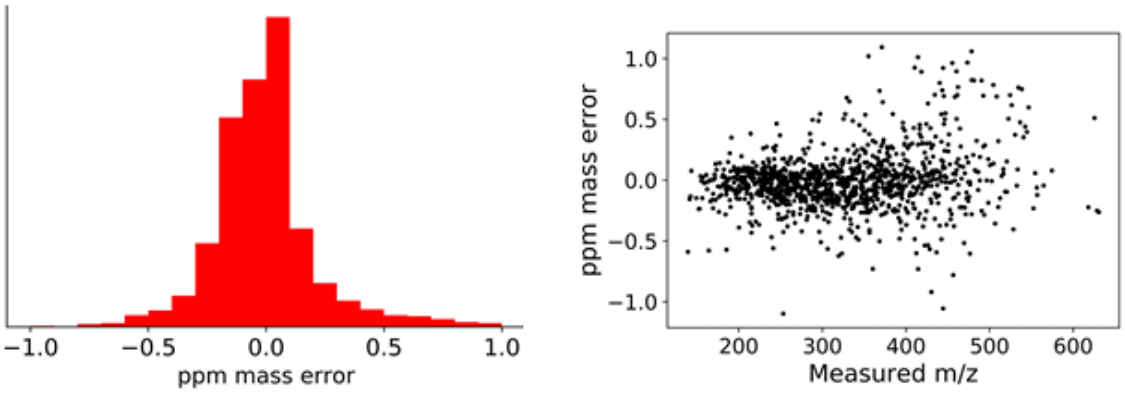

Figure 4-6: Histogram of mass errors from compound assignment (left) and scatter plot of mass errors vs m/z (right). The histogram indicates a distribution centered close to zero meaning that systematic error in assignment/measurement has been minimized. Error generally increases with increasing m/z as shown in the scatter plot.

other studies on similar samples [166]. An improvement of the number of peaks may be enhanced through use of stored-waveform inverse fourier transform (SWIFT) cyclotron

resonance excitation and using novel spectral stitching methods to obtain better signal over a wide range [184, 185]. A rms mass error of 122 ppb was obtained by McKenna et al. for Macondo well oil with APPI by using a novel "walking" calibration method not used for our study [186]. Thus, through the use of these enhanced data analysis and data collection workflows, a variety of dopants, and possibly higher resolution FT-ICR instrumentation, we expect LIAD-APPI to perform comparably for crude oil complex mixtures.

Anisole was also studied as a dopant for the Macondo well sample and offered less assigned formulas 916, but better rms mass error than toluene. With anisole, a mean error of -23.0 ppb and rms error of 183 ppb were obtained. A spectrum using ansiole as the

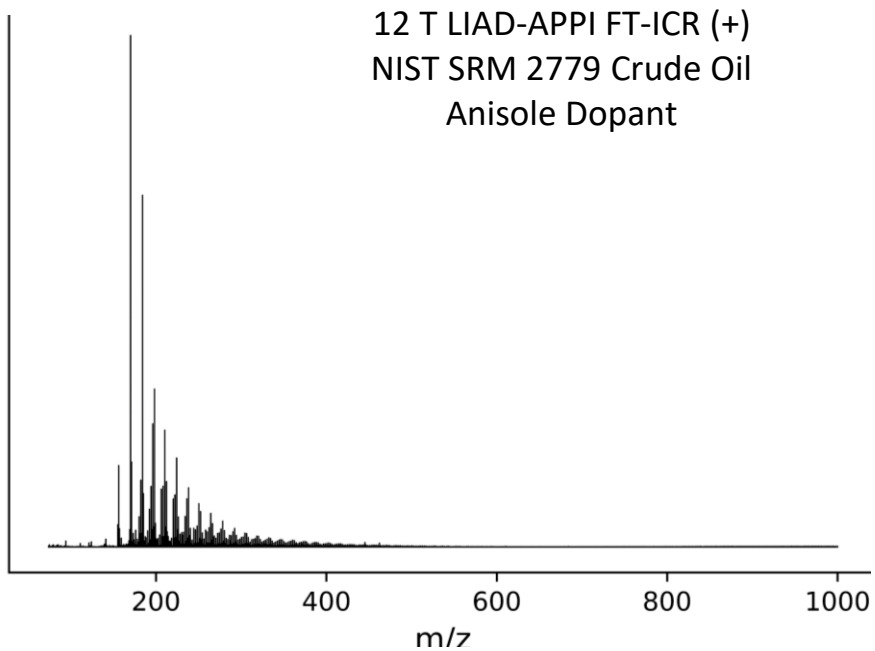

Figure 4-7: Positive mode spectrum for Macondo well oil using anisole dopant.

dopant shown in Figure 4-7 indicating a slight preference for lower mass species. Differences between the two dopants may arise from somewhat different dopant

ion-analyte neutral collison dynamics due to the lower IP of anisole, 8.2 eV versus 8.8 eV

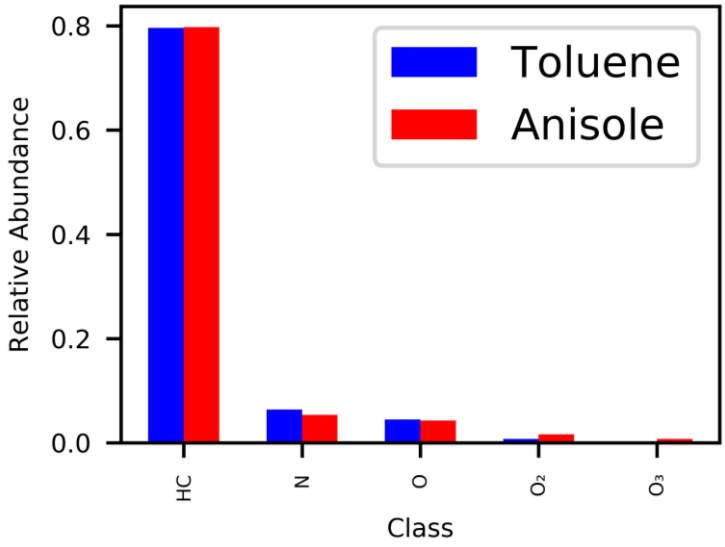

Figure 4-8: Class distribution comparison between toluene and anisole dopants. Relative abundance was determined by summing peak abundances normalized by the sum of intensities for the compounds assigned in the mass spectrum corresponding to a particular class.

for toluene. The lower error in compound assignment is likely due to the lower number of assignments stemming from lower abundances of already dilute components with anisole. Some of these peaks were excluded as the same compound assignment relative intensity threshold was used. To our knowledge, this has been a first instance of anisole's utility as a petroleomics APPI dopant. This brings forth the idea of establishing a variety of dopants and their performance characteristics for petroleomics which is an area of optimization that can be explored extensively with LIAD-APPI.

To compare the differences in compound assignment, class distributions obtained using the two different dopants are provided as a function of relative abundance (Figure 4-8). While toluene leads to predicting a slightly lower abundance of O_2 species, the results are fairly comparable between the two dopants. Based on elemental formula assignment, an

average double bond equivalence (DBE) for each dopant, was estimated for the entire sample according to the method provided by Bae et al. and shown in equation 28 [168].

$$avg\ DBE = \frac{\sum DBE_i I_i}{\sum I_i} \tag{30}$$

Where DBE_i is the double-bond equivalence for a particular assigned m/z, i, and I_i is the relative intensity of the assigned m/z. DBE_i can be calculated for a neutral molecule $C_c H_h N_n O_o S_s$ as follows [187, 188]:

$$DBE = c - \frac{h}{2} + \frac{n}{2} + 1 \tag{31}$$

For anisole, an average DBE of 2.4 was calculated versus 2.5 for toluene again illustrating little discrepancy for the analysis workflow presented.

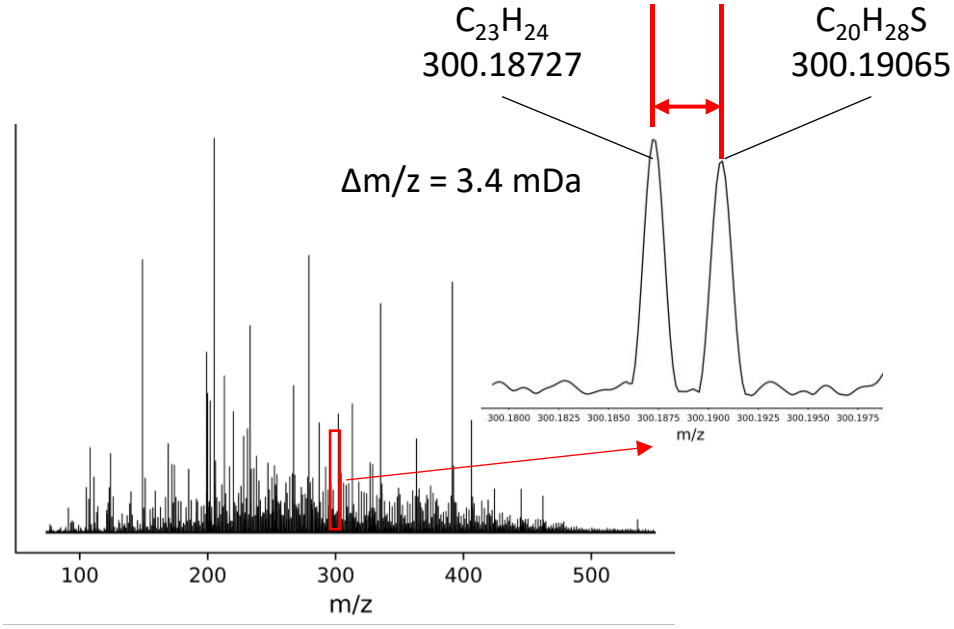

Figure 4-9: LIAD-APPI FT-ICR mass spectrum of Khatyspyt shale extract dated at ca 550 Ma. Inset shows the differentiating power of FT-ICR mass spectrometry distinguishing a SH_4 species from a C_3 species. Toluene was the dopant for all shale studies.

4.3.3 Khatyspyt formation shale extract

In addition to conventional petroleum products, we also analyzed a solvent extracted 550 Ma shale from the Khatyspyt formation as an example of an unconventional petroleum source illustrating ease of sample preparation and accurate assignments via LIAD-APPI FT-ICR MS. Typically, these petroleum sources are analyzed via GC-MS with MS/MS for identification [139, 140, 189]. While these approaches can yield structural information on compounds of interest, they fail to resolve the isobaric species, e.g. C_3 vs. SH_4 species with exact mass difference of 3.4 mDa. A spectrum of shale extract obtained by positive mode LIAD-APPI is shown in Figure 4-9 with an inset illustrating the separation of an identified C_3 and SH_4 species at nominal m/z 300 under broadband detection settings. ~15,850 peaks were observed at a S/N > 4 over a 110 – 700 m/z range. Using the confidence in mass accuracy obtained from initial instrument calibration, a homologous series was identified to use as an internal calibrant. After which, 1,341 compounds could be assigned elemental formulas with mean mass error of 1.5 ppb and a rms error of 247 ppb. Compound

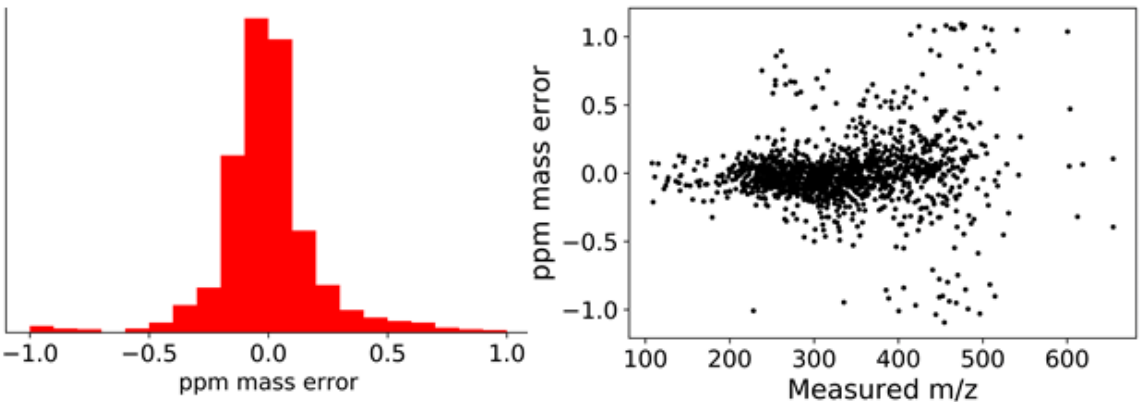

Figure 4-10: Error plots obtained for the Khatyspyt formation shale extract compound assignment. The histogram (left) is centered about 1.5 ppb and most errors fell below 500 ppb. Several assignments between m/z 400-500 had unusually high errors given by the scatter plot (right).

assignments with mass error > 1 ppm were discarded. Plots for the error analysis can be seen in Figure 4-10. Based on elemental formula assignment, an average DBE of 8.5 was estimated for the entire sample indicating our workflow qualitatively establishes the highly conjugated nature of shale oils versus light oils based on the results above for Macondo

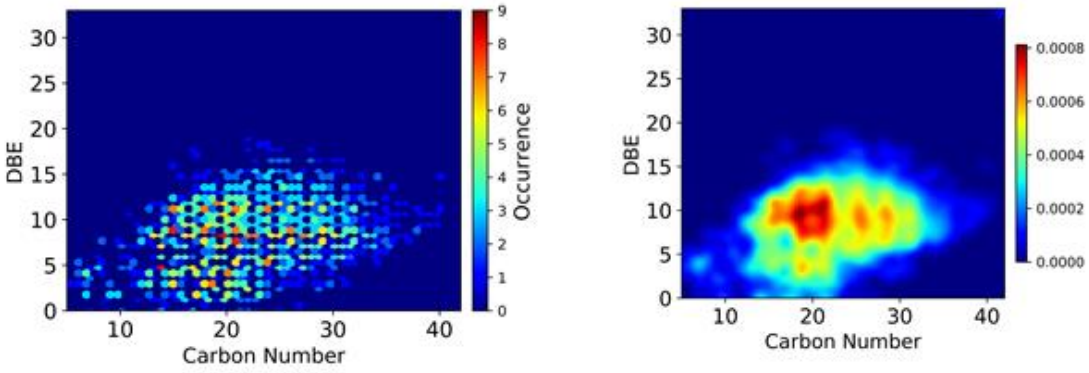

Figure 4-11: DBE plot obtained by using a hexagonal binning algorithm to group compounds by their carbon number and DBE (left) and a gaussian nearest neighbor (k = 2) smoothed histogram (right) for ease of visualization.

well oil. For visualization a plot of DBE versus carbon number illustrating the extent of conjugation over the entire sample is shown in Figure 4-11. An average DBE of the hydrocarbon (HC) class for this shale extract was determined to be 9.5 which is comparable to the HC class DBE determined for other shales via APPI methods [168, 190]. Upon investigation of the class distribution shown in Figure 4-12, we observe a fair number of O_1, O_2, O_3, O_4, and O_1S_1 species indicating a moderate degree of oxidation for this sample. This is to be expected for shales whose extracts are considered to be a degraded petroleum source. However, the highest abundance assignments are still due to the hydrocarbon content for our analyses. Therefore, these results indicate LIAD-APPI to be useful for identifying these heteroatom species which are known to cause pollutant formation and processing issues of fuel sources derived from high heteroatom content petroleum.

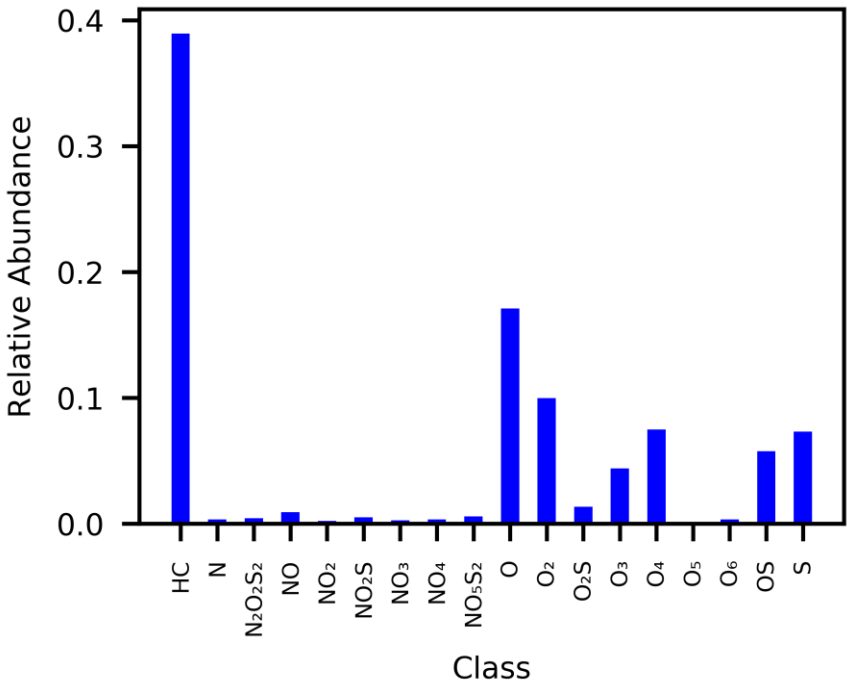

Figure 4-12: Class distribution for Khatyspyt shale extract obtained from formula assignments following LIAD-APPI FT-ICR MS. Relative abundance was determined by summing normalized peak intensities for the compounds assigned in the mass spectrum corresponding to a particular class.

Like the Macondo well oil analyses, higher numbers of compound assignments could enhance the results obtained by elucidating more of the chemical space. Nevertheless, we express confidence in the elemental formula assignments provided though it is unclear how representative they are of the sample given the lower number of compound assignments by comparison to similar studies on shale samples [168].

4.3.4 Azerbaijan Heavy Sweet (AH) and Venezuelan Heavy Sour (VH) Crude Oils

To demonstrate characterization with one of the most chemically complex petroleum sources, two samples of heavy crude oils were obtained. Information provided by ONTA (See Supplemental section) indicated one to be an aromatic-naphthenic heavy

"sweet" crude sourced from Azerbaijan where as the other was a Venezuelan heavy "sour" (high sulfur content) crude. Physical observations for each included a viscous liquid where the aromatic-naphthenic crude had a homogenous brown appearance and the sour crude had a jet-black tar-like character. Based on the observed performance with the Macondo well oil, toluene was used as the dopant in these analyses.

The heavy sweet sample proved to be the most complex giving large distributions for many heteroatom classes in both positive and negative mode. The positive mode results yielded a m/z distribution somewhat similar in mode and shape to the Macondo well sample. A summary of compound identification results can be seen in Table 4-1.

Table 4-1: Compound Identification Results for all Crude Oil Samples

	Peaks (S/N > 4)	Assigned Formulae	Average DBE	Mean mass error (ppb)	rms mass error (ppb)	Rel. Abundance Threshold (%)
AH (+ mode)	~20,000	842	10.3	-7.7	171	1.0
AH (- mode)	~20,000	1296	6.3	-20.9	252	4.0
VH (+ mode)	~20,000	1843	8.9	-3.7	225	1.5
Macondo well (+ mode)	~22,000	1173	2.5	-5.5	235	0.1

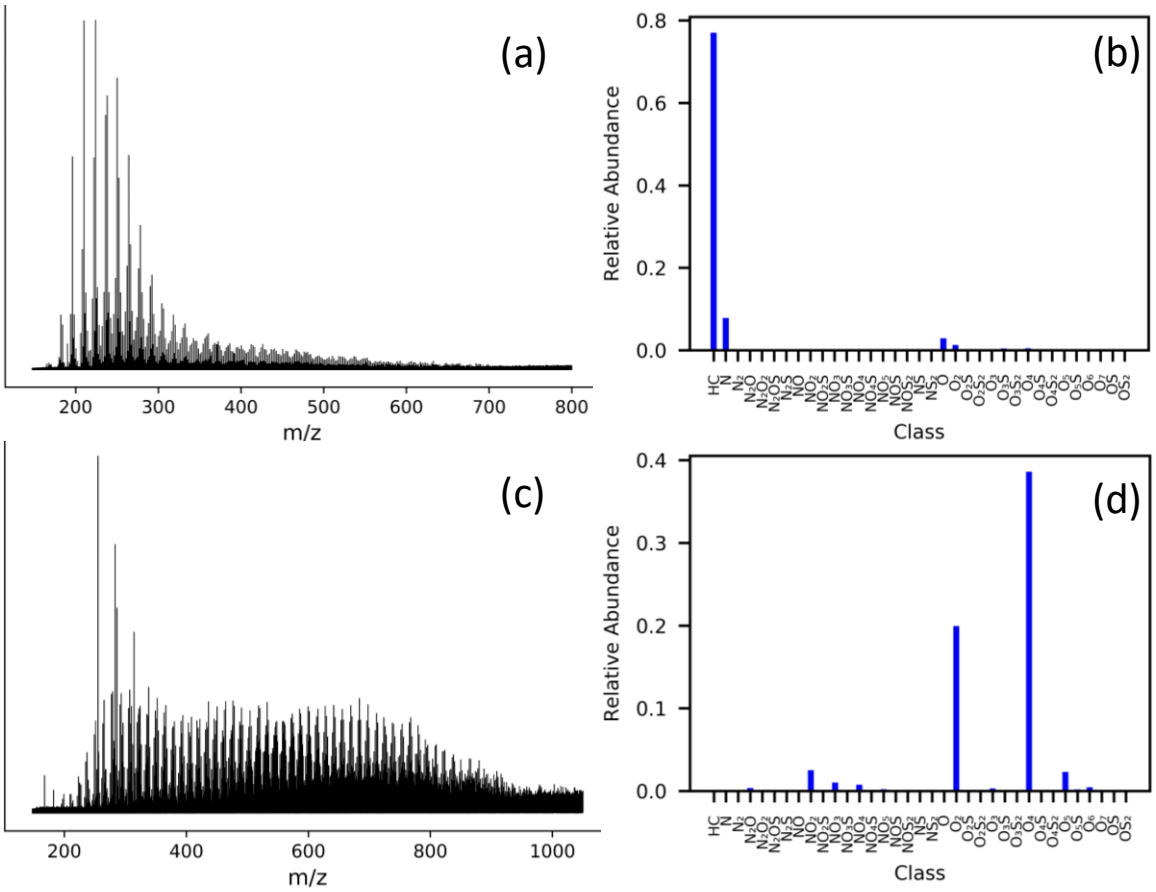

Figure 4-13: Positive mode spectra for the AH crude oil (a) with associated class distribution (b) and negative mode spectra (c) with associated class distribution (d). Results are indicative of heavy oxidation with a small abundance of N_1 class compounds assigned. Relative abundance was determined by summing normalized peak intensities for the compounds assigned in the mass spectrum corresponding to a particular class.

Positive and negative mode spectra for the AH crude oil can be seen next to their respective compound distributions in Figure 4-13.

Assigned compound distributions for the heavy sweet crude revealed high abundance of O_2 and O_4 species in negative mode indicating a high degree of oxidation of the sample. A more complete class distribution plot can be seen with Figure 4-16 in the supplemental section for this sample. The series corresponding to the O_2 species begins at

lower masses and decreases in abundance at about m/z 680 where as the O_4 series spans the 400-1000 m/z range. Oxidation of crude oil has been studied extensively in the wake of the *Deepwater Horizon* disaster revealing photooxidation and biodegradation to lead to the formation of these species [191, 192]. The appearance of these species in negative mode with APPI indicates that these heteroatom species are most likely series of fatty acids. Thus, this result indicates LIAD-APPI to not only be useful for the aromatic non-polar fraction of crude but also for the polar oxygenated species formed from weathering processes. This is consistent with our positive results on carboxylic acids in negative mode described earlier.

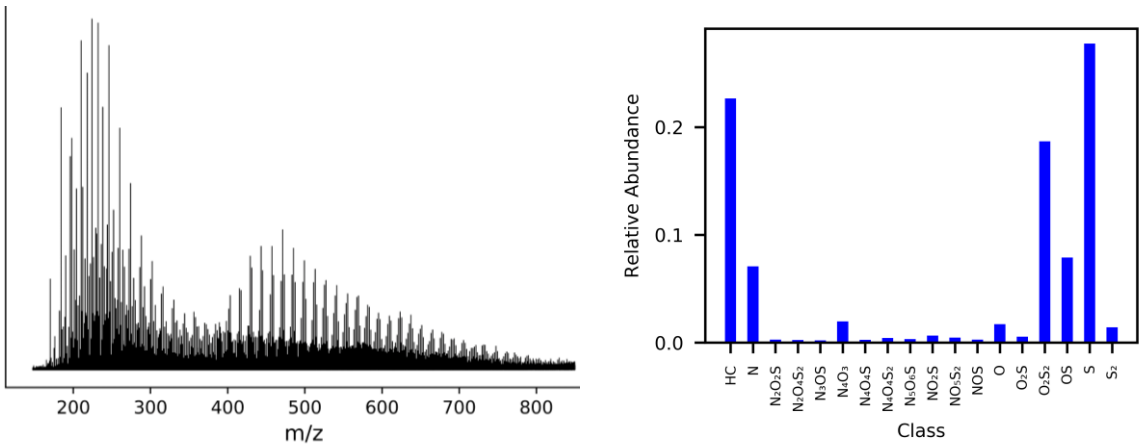

Figure 4-14:Positive mode spectrum for the VH crude oil (left) and associated class distribution (right). Significant sulfur-oxygen heteroatom species are observed after compound identification. Relative abundance was determined by summing peak abundances normalized by the sum of intensities for the compounds assigned in the mass spectrum corresponding to a particular class.

Extending these analyses, we were able to identify 1,843 compounds in the VH crude oil sample in positive mode with comparable error estimates to other samples (See Table 4-1). The resulting spectrum and class distribution obtained on positive mode in Figure 4-14 (left) reveals two modal distributions of oxygenated-sulfurous heteroatom

species. From m/z 170-400, a large number of peaks corresponding to the O_1S_1 class were identified as well as a high number of S_1 class species. Spanning the m/z 400 – 800 range, series corresponding to the O_2S_2 and O_2S were identified. The presence of these species is consistent with the observed asphaltic nature of this sample and other Venezuelan heavy crude sources [193-195].

Only few small signals were obtained for the VH sample in negative mode where only about 116 compound assignments were made. Notable assignments were the presence

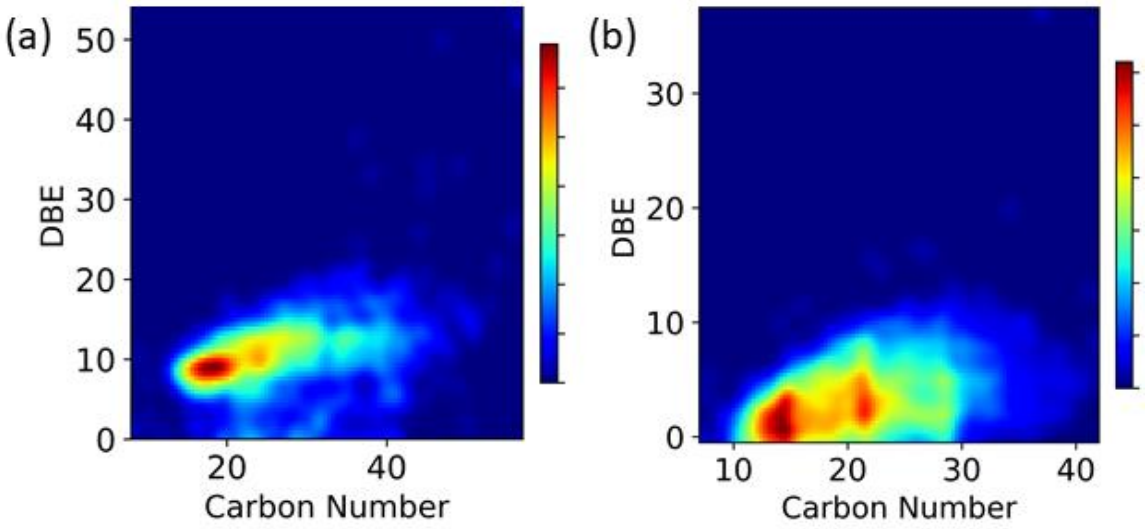

Figure 4-15: DBE distributions vs number of carbons in (a) AH crude oil assigned compounds from a positive mode spectrum and (b) Macondo well oil compounds from positive mode spectrum. Distribution for the AH crude extends beyond 40 carbons where as the Macondo well oil truncates at about 40 carbons.

of a few O_2 and O_4 species though no compounds assigned were in particularly high abundance. A qualitative trend in average DBE across the entire sample was noticed for the crude oils indicating consistent results with the reported general nature of the samples. For the AH sample reported to be an aromatic-naphthenic crude, an average DBE of 10.2 was calculated for positive mode based on formula assignment. This is consistent with the

observation that ring-like and conjugated species ionize readily with LIAD-APPI in positive mode and that the conjugated nature of these samples should be higher than that of light oils such as the Macondo well oil studied here. A comparison of DBE vs Carbon number plots is shown in Figure 4-15 for both the AH and Macondo crudes illustrating a shift in the 2D distribution towards higher DBE for the AH sample relative to the Macondo oil. This would be consistent with the light (minimally degraded, high H/C ratio) vs. heavy (degraded, reduced H/C ratio) designations. Additionally, an average DBE for the VH crude was calculated at 8.9 indicating a higher presence of heteroatom species and conjugation relative to the light crude samples. Therefore, it appears that the qualitative nature between degraded and light oils is retained when using LIAD-APPI with our data analysis workflow.

4.4 **Conclusion**

Based on our results above, LIAD-APPI offers a unique and effective avenue for sampling deposited petroleum samples. This not only constitutes the first instance of LIAD-APPI coupled with a ultra-high resolution FT-ICR mass spectrometer but also the first application of our source technology to some of the most chemically complex mixtures known. With our experimental protocol and data analysis workflow, spectra with > 20,000 peaks at a S/N > 4 are routine. Improvements such as “spectral stitching” and automated-motion sample stages could increase the amount of peaks observed by increasing S/N for less abundant species through optimized signal collection windows and enabling an increased number of scans. For the Azerbaijan heavy crude oil, a total of 2,138 compounds

were identified from LIAD-APPI analyses combining both negative and positive mode. This figure is an order of magnitude lower than the number of compounds typically identified by others for crude oil by APPI but we note that this data analysis is in the absence of using a "walking calibration" method and the other signal collection and processing methods used by others [163, 166, 186]. This work ultimately serves to demonstrate LIAD-APPI as a useful ambient desorption-ionization method when coupled with a FT-ICR mass spectrometer. Key benefits are ease of sample preparation, lower mass loads on the spectrometer, non-polar as well as mildly polar compound analysis capabilities, and low-source temperatures. Additionally, we presented the notion of utilizing a diverse set of atmospheric dopants including volatile alkanes to extend the types of species which can be ionized by APPI. This is only afforded by elimination of the standard APPI liquid flow injection achieved by our ambient desorption ionization source configuration.

4.5 Acknowledgements

We thank David Deamer and Andrew Knoll for providing the Khatyspyt shale sample analyzed in this work. This work was supported by the NSF and NASA Astrobiology Program under the NSF Center for Chemical Evolution grant number CHE-1504217.

4.6 Supplemental

Useful yet unreferenced data plots can be seen in this section regarding the error analysis for the heavy crude oil samples and DBE vs Carbon plots otherwise not shown.

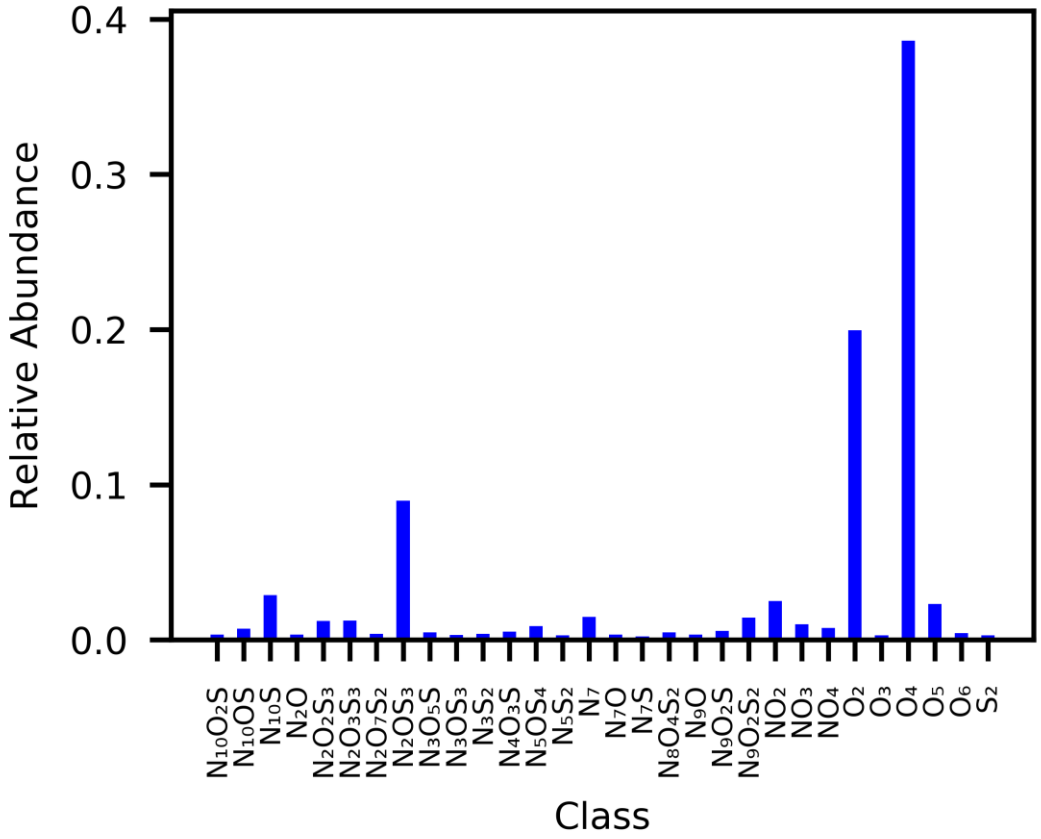

Figure 4-16: AH class distribution for 30 of the most abundant classes determined after compound assignment based on the negative mode spectra.

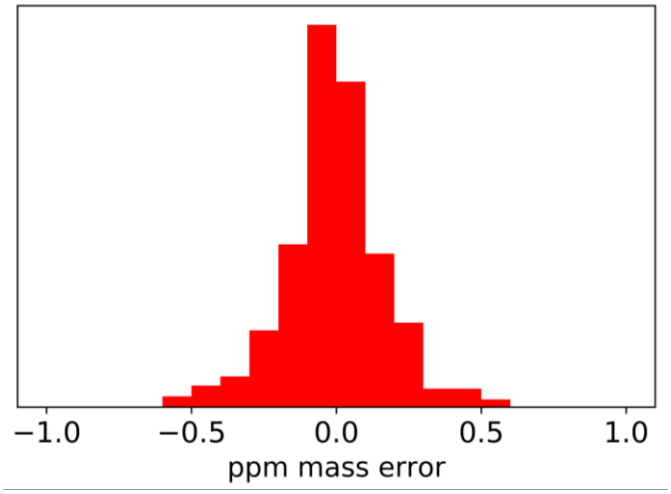

Figure 4-17: Histogram error plot for the Azerbaijan heavy aromatic-naphthenic crude oil compound assignments in positive mode. Distribution is centered around -7.7 ppb mean error. The plot has a generally gaussian shape at the abundance threshold of 1% used to limit compound assignments.

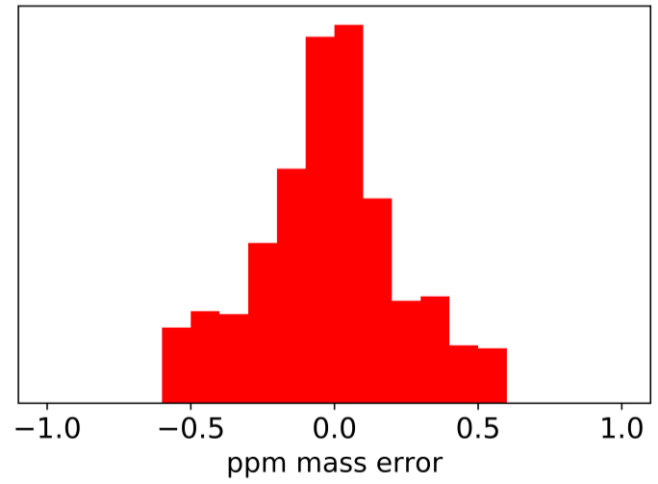

Figure 4-18: Histogram error plot for the Azerbaijan heavy aromatic-naphthenic crude oil compound assignments in negative mode. Truncation of the assigned compound distribution was held at an absolute error or 500 ppb. The histogram is centered about a mean error of -20.8 ppb. Abundance threshold was 4%, lower thresholds gave a near uniform error distribution for these samples.

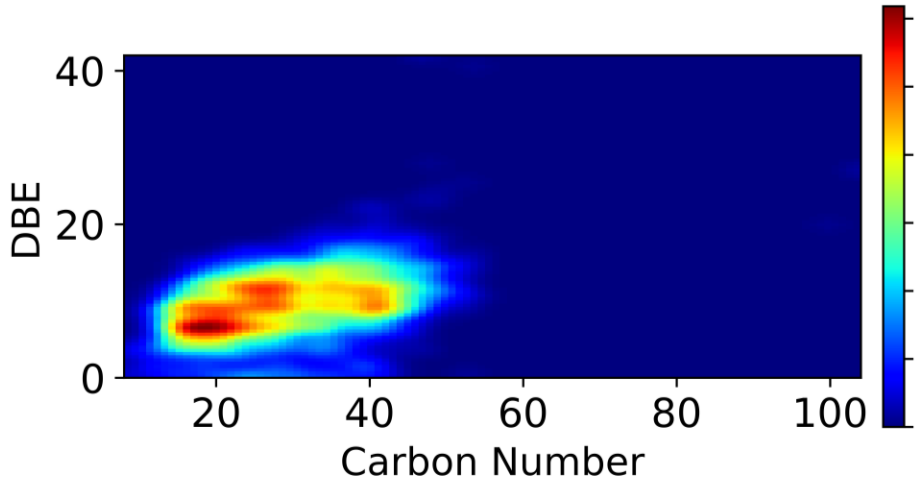

Figure 4-19: DBE versus number of carbons for the Venezuelan heavy sour crude taken in positive mode. Higher carbon numbers were noted for this sample with a substantial degree of O_oS_s class species present. Average double bond equivalence is calculated at 8.9 for all compounds identified.

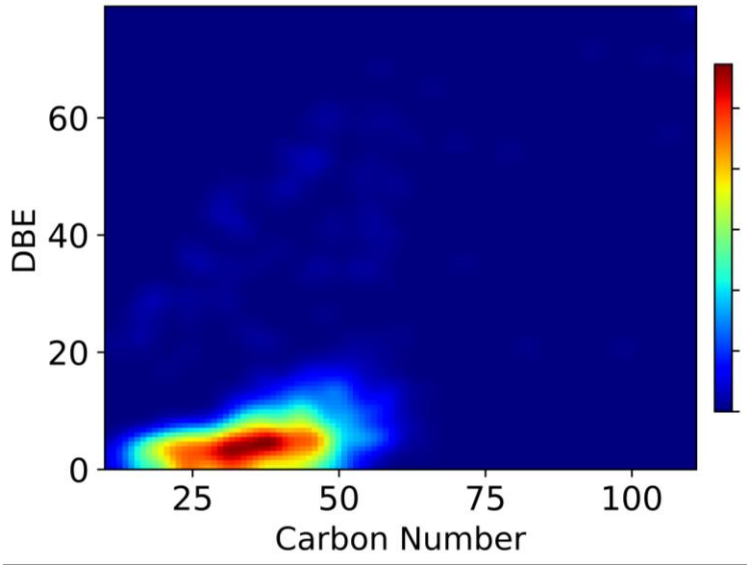

Figure 4-20: DBE plot for the Azerbaijan heavy aromatic-naphthenic crude oil compound assignments in negative mode. This distribution in general exhibited lower DBE than the positive mode results with an average DBE of 6.3 for all compounds identified.

Table 4-2: ESI Calibration Result

Compound	Exact m/z	Measured m/z	Error (ppm)
Na2(CF3CO2)	158.964029	158.96403	0.006290731
Na3(CF3CO2)2	294.938837	294.93886	0.07798227
Na4(CF3CO2)3	430.913645	430.91367	0.058016265
Na5(CF3CO2)4	566.888453	566.88856	0.188749655
Na6(CF3CO2)5	702.863262	702.86335	0.125202162
Na7(CF3CO2)6	838.83807	838.83821	0.166897528
Na8(CF3CO2)7	974.812878	974.81312	0.248252773
Na9(CF3CO2)8	1110.787686	1110.78768	-0.00540157
Na10(CF3CO2)9	1246.762494	1246.76263	0.109082524
Na11(CF3CO2)10	1382.737303	1382.73738	0.055686644
Na12(CF3CO2)11	1518.712111	1518.71291	0.52610366

Table 4-3: Physical Properties of Azerbaijan Aromatic-Naphthenic Crude Oil

Property	**Value**
Density	0.9395 g/mL
Ash Content	0.11%
Cocking Behavior	3.27%
Content of Resin	Vitriolic 24%; Silica gel 11.4%
Sulfur Content	0.31%
Nitrogen Content	0.24%
Asphaltene	0.49%
Pour Point (Setting Point)	20°C
Flash Point	125°C
Viscosity (@ 50°C)	Conditional Degrees 51.48
Acidity	1.29 mg KOH/g

Table 4-4: Bulk Chemical Properties of Azerbaijan Aromatic-Naphthenic Crude Oil

Hydrocarbon Group	**Yield, % Oil (Oil Output Percentage)**
Naphthenic	55.0
Aromatic Light	9.0
Aromatic Medium	11.7
Aromatic Heavy	10.1
Resin	14.2

Table 4-5: Physical Properties of Venezuelan Heavy Sour Crude Oil (Reference ID: OGJ 99)

Property	**Value**
API Gravity	14.7°
Flash Point	37°C
Reid Vapor Pressure	14 kPa
Density (@ 15°C)	0.9679 g/mL
Pour Point	-12 °C
Kinematic Viscosity Temp. (°C)	**Kinematic Viscosity Value (**mm^2/s or cSt)
38	992
99	39
Distillation Boiling Range (°C)	**Yield of Crude (%)**
IBP – 100	1
100-150	2
150-200	2
200-250	5
250-300	6
300-343	6
343-402	12
402-461	10
461-520	9
>520	46

Table 4-6: Bulk Chemical and Trace Element Properties of Venezuelan Heavy Sour Crude Oil (Reference ID: OGJ 99)

Sulfur Weight	2.74 %
Asphaltene Weight	9.00%
Nitrogen Weight	0.51%
Trace Metals	**Concentration (ppm)**
Aluminum	< 5
Nickel	84
Sodium	25
Vanadium	303

CHAPTER 5. CONCLUSIONS AND OUTLOOK

5.1 Review of Results

When this project began, the source technology consisted only of a MHCD device fabricated to about the size of a soda can utilizing a cumbersome gas mixing manifold. The size of the device limited the flexibility for close proximity source configurations, an important feature when using VUV radiation in atmospheric conditions. Also, the gas manifold limited the length of time experiments could be run due to the periodic need for generating new Ne/H_2 stock gas. Furthermore, due to limited access to appropriate instrumentation, it was unclear if the Lyman-α emission we expected to be forming was even successfully transmitted out of the device. Applications of these devices as photoionization tools for mass spectrometry appeared to be limited only to small, volatile molecules using only photoirradiation from the device for desorption and ionization. Hence, in terms of source robustness and utility the project was in its infancy with regards to mass spectrometry applications.

The first major accomplishment of this work was demonstrated in Chapter 2 where the device was miniaturized and generation of Lyman-α light and its transmission out of the device window was confirmed. Though in working to further the use of MHCDs as photoionization devices for mass spectrometry, several other key improvements were made defining the trajectory for the rest of this work. Most importantly, LIAD was coupled with the device as an effective means of desorption for a range of molecules. Additionally, after observing the limited sensitivity and scope of compounds which could be ionized solely by photoionization, toluene was utilized as an atmospheric dopant for dopant-assisted

APPI. This had been the standard for spray-based APPI since its inception. As a result, this became the first instance of LIAD combined with post-desorption ionization by APPI thus coining the term LIAD-APPI. Key results indicated utility and sensitivity for small non-polar species relying solely on the forward ejected velocity of desorbates and pressure-driven inlet flow for collection.

Of course, there were challenges with the approach in Chapter 2. One such challenge being detection limits an order of magnitude higher than comparable studies due to a significant time delay to reach peak signal after LIAD had started. Thus, the need for a mass transport component became apparent introducing the sweep-jet configuration discussed in Chapter 3. Additionally, a minor scientific yet substantial workflow improvement was made by replacing the Ne/H_2 gas mixing manifold with a 0-50 sccm mass flow controller dedicated to the neon plasma gas and 0-10 sccm mass flow controller dedicated to pure H_2 for admixture purposes. Although this was not an advancement in terms of the physical science, it allowed longer operation times enabling iterations LIAD-APPI source optimization experiments discussed in Chapter 3. Initially, these additions improved the detection limits of test compounds to comparable values in the hundreds of fmol range. Expansions of the analytical capabilities allowed detection of the seldom studied cholesterol-ester compounds and larger triacylglycerols using both toluene and anisole as atmospheric dopants illustrating differences in fragmentation patterns that should be considered. Chapter 3 also introduced LIAD-APPI's capability for low-polarity complex mixtures including extra-virgin olive oil (EVOO) and shale hydrocarbon extracts. A range of species in EVOO were able to be assigned due to the mixtures well-known composition though, were this an unknown, the confidence in assignment would be fairly

low due to m/z errors typical of TOF mass analyzers. We also discussed the mechanistic function behind the transport of the species using computational fluid dynamics (CFD) and particle trajectory simulations. These simulations indicated that forward ejected velocity after LIAD only propagates the particles a few mm from the surface. The sweep-jet induced a swirling flow eventually drawing these species into the streamlines entering the inlet. While in the swirling vortex, it was expected that the analyte molecules underwent multiple collisions with dopant photoions thereby increasing ionization efficiency. These improvements brought forth LIAD-APPI from its inception-state to an application ready source.

Due to the improvements and successes discussed in Chapter 3, this led the determination that an ideal application field of choice for this source would be petroleomics. Chapter 4 utilizes LIAD-APPI to gain a holistic chemical analysis for several complex petroleum mixtures. This not only constituted the first time LIAD-APPI had been used for crude oil samples, but also the first coupling of LIAD-APPI to an ultra-high resolution FT-ICR mass spectrometer. Results indicated that LIAD-APPI was well suited to desorb and ionize a range of species in both positive and negative mode offering a substantial amount of peaks, comparable to most studies on petroleum. Using modern data processing and analysis approaches for these samples would most likely provide at least equal if not greater amounts of peaks and compound assignments if compared to other techniques.

From its concept to the analysis of complex mixtures in petroleomics, this writing serves as an account for the step-wise development of the novel desorption-ionization technique, LIAD-APPI. This is not only the first instance of APPI with LIAD, but also an

instance utilizing the novel MHCD device to its full potential. It is now clear that these devices can ionize a large number of species when utilizing dopant volatile molecules. Though indications of performance at this stage are good, there are still many questions that can be addressed surrounding this technology. We will now aim to discuss these in the next section.

5.2 Future Directions

Though the technology has proceeded down an exemplary and conclusive path for development, several options remain to improve LIAD-APPI and the technologies therein. Avenues exist to potentially extend this work to other molecular classes, improve upon the existing workflows, elucidate fundamental mechanisms, and adopt these technologies in other areas.

As discussed in Chapter 4, one benefit LIAD-APPI presents is a much larger dopant parameter space. Because the dopant is no longer required to be the solvent (or at least fraction of the solvent) for spray-based APPI, this frees the mass spectrometrist to utilize any volatile organic with an IP < ~10.2 eV that may act to ionize the molecular class of interest. One such example would be the use of small molecule, volatile alkanes to enable hydride abstraction ionization in positive mode of high alkanes. This was presented as a possible pathway for forming the $[M-H]^+$ with APCI by Marotta et al. [182]. However, this approach has not been attempted at the present moment of this work and could extend an otherwise incapable ionization method to these species.

During the development of this source, several workflow hinderances were identified. One such unsolved issue is the attachment and consistent positioning of the foil

sample mount. As briefly mentioned in Chapter 2, the foil is stretched and secured to a tube which is situated on some fixture secured to a ¼-20 screw size mounting plate. For each sample, a foil must be re-stretched and mounted. This provided an ad-hoc sample mounting method but introduced the possibility for inconsistent sample positioning, decreasing reproducibility. This also required manual rotation of the sample tube involving reaching near the source to perform this by hand which is not ideal. A proposal to alleviate this might involve the use of motorized and computer-controlled rotation or rastering stages which can automatically move the foil sample stage allowing the fixed laser to desorb from multiple areas. In conjunction with the iMatrixSpray deposition method discussed this would provide a relatively consistent and repeatable process. Additionally, foils could stand to be replaced with metal-glass substrates ensuring flat surfaces as well. A note of caution to those who proceed down this path might be that it is unclear what effect the metal-glass junction will have on desorption efficiency with LIAD. Other enhancements along this same vein could include engineering a modular source door to attach to common mass spectrometers which keeps the dopant nebulizer, MHCD device, sample mount, and possibly some of the laser optics in reproducible, fixed positions.

In addition to overall LIAD-APPI source development, there are potential pathways for advancing the efficacy of MHCD VUV photon generation and their range of capable emission spectra. Thus far, we have only demonstrated the use of MHCDs with a single hollow through the electrodes. Though no serious hinderances have been noticed from this design, this in effect means that most of the VUV generation occurs in a small 100 μm diameter, 200 μm deep volume. By fabricating electrode-insulator-electrode structures with multiple holes this should effectively increase the VUV flux generated by a factor of

n for n hollows in the electrode structure. An important parameter space to characterize for these designs would be the current-voltage characteristic, plasma gas flow rate, and VUV output where a measurement of the Lyman-α line intensity would be a good indicator of performance. In addition to electrode structures, it has been theorized that these devices lend themselves to be tunable, a characteristic not shared by rf discharge lamps. In order to bring this concept to fruition, it would be necessary to engineer an evacuating gas manifold which can load and purge itself of several rare gases to achieve a range of photon outputs. And, because these devices were originally developed as VUV sources for spaceflight missions, it would be useful to develop a circulating flow to reutilize and conserve the precious rare gas for long periods of time. Another avenue for increasing the VUV efficiency of these devices could be the incorporation of pulsed DC power sources. Many researchers have utilized this concept and shown an increase in efficiency due to the higher instantaneous power density and electron temperature obtained from generating a discharge under these conditions [196-200]. Therefore, a multitude of avenues exist to improve upon these devices which appear to still have an active research interest in the literature.

Upon the petroleomics applications of LIAD-APPI in Chapter 4, it became apparent that the analysis and instrumentation was just as important for the signal processing and post-collection data analysis. In an effort to retrieve software and programs to perform these operations in a transparent way outside of proprietary algorithms provided by instrument manufacturers, it became apparent that there was no truly open-source petroleomics data analysis software that was feasible for compound identification[201, 202]. Formularity offered promise though its capabilities were limited and was already

precompiled therefore it could not be modified [202]. Given the current prevalence of open-source software and the relative unavailability of these processing programs, it would be in the best interest of the field of petroleomics to create an open access repository in python to house programs capable of FT-ICR MS data analysis. The vision stated here would include raw FID signal processing protocols, visualization tools, plotting tools, formula assignment, calibration protocols, and spectral processing tools. Of course, this is no small task but would benefit the field immensely by standardizing the data workflows of the field such that protocols could be replicated between experiments enhancing the collaborative nature of the field. Furthermore, because python is the proposed language, this would allow for cross platform installation where as current packages are observed to be limited. Software packages of greater scales and similar academic nature are also found in areas like computational chemistry and available in python [203, 204]. For the analytical chemist seeking to gain solid statistical and software skills, this would be an ideal undertaking. Some small contributions in this direction can already be seen in Appendix E of this work for common petroleomic plot generation in python.

5.3 Final Remarks

Hopefully it is now apparent of how far this technology has come and the contributions it has made with respect to ion sources in mass spectrometry. I am both interested and optimistic to see the advances made on top of what this work has accomplished. Though, it is my opinion that, after several years of work on this project, the field of mass spectrometry leaves little room for further development in the realm of ion sources. For the aspiring mass spectrometrist, the greatest impacts stand to occur in the realms of statistics and software development whether they be state-of-the art machine

learning models or enhanced user-friendly design and accessibility. I digress, but these are the trends of today which, from my perspective, stand to put the most power in the scientist's fingertips.

APPENDIX A. BASIC OPERATION FOR LIAD-APPI FT-ICR MS EXPERIMENTATION

This section is meant to describe the general set up procedures and protocols to run an analysis with the LIAD-APPI source on the Bruker solariX XR 12T FT-ICR.

A.1 Requirements:

1. Computer with at least 2 USB ports for COM Communication
2. VUV Controller 2.7.5 software and LabVIEW and a general idea of its function.
3. Opotek Laser Control Systems software
4. Basic training on Bruker solariX FT-ICR with ESI
5. A prepared LIAD sample on foil attached to the sample tube.
6. Laser authorization and set-up specific knowledge.

A.2 Set Up and Run Procedure

1. Upon entering the lab space, hook your computer to the National Instruments (digital acquisition) DAQ and laser power supply (black box) USB cables.
2. Start the laser cooler (Big Sky ®) by turning the key on the front panel. You should see the box light up and hear the pump working. Note there is a direct control box on top of the red laser module, this shouldn't read any errors after a few seconds.
3. Power on the laser power supply (black box) via a switch on the front panel.

4. To prevent backflow and trace contaminants from entering the plasma gases, with the quick valves closed, open and close the main valves on the neon and hydrogen cylinders to pressurize the small space between the main valve and quick valve.
5. Open the quick valves.
6. Purge the MHCD device with nitrogen before running by opening the nitrogen gas line and introducing ~4 SLM flow to the device via the clear plastic flow meter on the electronics tower.
7. Start the VUV Controller 2.7.5 program and click the “Open 0” and “Open 1” buttons and un-click the “Close 0” and “Close 1” buttons to open mass flow controller (MFC) 0 and 1 valves and purge the plasma device with the gases. (This only needs to be done once a day). The program should read MANUAL SETPOINTS in the grey box on the control panel.
8. After it appears that the pressure has been substantially depleted, open the main valve on the neon and hydrogen cylinders. Let purge for ~5 min.
9. If a calibration of the spectrometer is needed, use the NaFTA solution and ESI source to calibrate the instrument. This usually needs to be done every few days.
10. After calibration or if not required, make sure the Bruker software method is set to an appropriate LIAD-APPI method with ESI listed as the source and set the instrument in OPERATE mode.
11. IMPORTANT: Set capillary and endplate offset voltages (under the API Source tab) to 50 volts. Typically, one can just set the capillary voltage to 50 and the endplate voltage changes automatically. Check both negative and positive mode and make sure the voltages are set to 50V. If they aren’t, the LIAD-APPI pieces

will arc upon switching polarity and the entire system will get thrown off. It will cause various components to shut down.

12. With the instrument still in operate and wearing nitrile gloves, promptly remove the ESI door, spray shield, and small round capillary cover and place on a clean dust-free cloth on a clean surface.
13. Position the stainless button-pressing arm to press and hold the ESI door button so that the interlocks aren't tripped. This is a stainless steel optic stand with a small 4-40 screw for pressing the interlock-button on the instrument.
14. Take the nebulizing needle apparatus and attach to the appropriate stainless optic post and align directly with the capillary inlet. This should be preconfigured so that no adjustments need to be made other than the angle of the arm on which the nebulizer is attached.
15. Take the sample tube and place in the rotatable optic holder. Carefully align the tube directly under, but not touching, the inlet capillary and using an allen wrench, secure the sample holding apparatus to be fixed.
16. Lower the MHCD apparatus. Using one's best judgement, asses that the exit window of the MHCD is pointing to the space between nebulizer needle and the inlet. This isn't exact and is difficult to see directly. The signal is not terribly sensitive to this positioning.
17. Fill the designated Hamilton 250 µL (or bigger if desiring an upgrade) syringe with the desired dopant, hook to the nebulizer needle you just placed, and secure the syringe to the black syringe pump apparatus to the right of the instrument source. Note: Anisole is not generally thought to be harmful so best to stick with

this for most analyses. Though flow rates are low enough that vapors aren't prevalent enough to be harmful.

18. Carefully adjusting the tubing and wires to the MHCD device, place the laser blocking box around the set up and cover with the lid.
19. Start the syringe at a rate of 9.75 µL/min via the Bruker control software. Pressing the fast-forward ">>" key sometimes helps to get things started.
20. On the VUV Controller 2.7.5 software, press the grey button that reads MANUAL SETPOINTS. This should change to AUTO SETPOINTS. The MFCs are now set to flow the gas in a certain proportion.
21. Be sure the nitrogen purge set on the clear plastic flow meter is now turned off.
22. Power on the Stanford Research Systems power supply, but do not enable the HV. Set the limiting current to 6 mA.
23. Power on the MHCD by enabling the high voltage via the black switch on the bottom left corner of the panel. Ramp the limited current up 1 mA at a time until 10 mA is reached. The voltage will probably read around -1170V but will settle to ~-1130V. This will change between different electrode pairs but generally should never be above -1200V.
24. Lift the lid of the laser box and check for an orange, steady glow coming from the device. If flickering, check all gas gauges and plasma voltages. If those are fine then the electrodes may be bad and a device rebuild is in order. (See Appendix : MHCD Device Rebuild)

25. On the Bruker control software, make sure that the DRY GAS is set to 5 L/min, the NEBULIZER is set to 1 bar, and the DRY TEMP is at 120 °C unless other parameters are desired.
26. A good check to make sure things are working is to observe the background signal by placing the instrument in TUNE mode by clicking the TUNE button at the top left of the GUI window. For high vapor pressure and small molecules this will show signal from some of the sample compounds. Though for very low vapor pressure, higher mass molecules no background is typically observed. Exit the tune mode when finished.
27. Check the collection settings in the bottom left corner of the Bruker GUI. Typical settings include ACCUM = 0.100s and 10 spectra.
28. It is typically a good idea to obtain a blank foil control to understand what signals are coming from the dopant and background. Once the foil tube, MHCD, and dopant are in place or operating you can click ACQUISITION/SINGLE and take a control spectrum. If not needed. Continue to set up the laser.
29. On the computer hooked up to the laser, open the Opotek software. The software should recognize and automatically find the COM port corresponding to the USB connection. You should hear the motors homing in the red laser module.
30. Click LAMP to warm the flash lamps (takes ~ 10 s).
31. Set the laser power/intensity to ~75% via the scroll bar on the control panel in the software.

32. Typical LIAD-APPI collections on this instrument are done by starting the laser pulse sequence by pressing LASER on the Opotek software and pressing the ACQUISITION/SINGLE button in the Bruker GUI simultaneously.

A.3 Shutdown Procedure:

1. When ready to shutdown, first turn off the laser via the Opotek software by clicking LAMP to turn the flash lamps off and then FILE > EXIT. The laser should re-home the motors and the software will close. Then turn off the power supply and cooler.
2. Turn off the plasma power supply, set the VUV Controller program to MANUAL SETPOINTS then set the CLOSE 0 and CLOSE 1 buttons to be green. Press STOP.
3. Close the neon, hydrogen, and nitrogen tank valves.
4. Set the instrument in standby mode.
5. Remove the laser shielding box, raise the MHCD apparatus to the top of its post, remove the sample tube, reposition the holder, remove the nebulizing needle, and empty any excess dopant into the waste vial.
6. Re-assemble the inlet cover and shield and replace the ESI door.

A.4 Spectral Formula Assignment Workflow Using Bruker Compass © Software Suite

1. Make sure you have the profile spectra and open data file in the DataAnalysis program. If it is not the profile spectrum, you will see a flat baseline rather than oscillating noise. If it’s the profile spectrum, skip to point 3.

2. Open your data file in the FTMS Processing, for crude oil spectra first calculate the magnitude mode spectrum. Set the “maximum peaks” to 10,000 (doesn’t actually do anything to profile spectra), use 0% data reduction, make sure save profile spectra is checked, and click SAVE TO BAF.
3. With the profile spectrum open in the Bruker DataAnalysis software begin by running a rough compound identification by selecting “SmartFormula” under the “Chemistry” tab. \
4. Once this finishes you should see a list of some compounds assigned to what are your most abundant peaks. For crude oil, it should start to become apparent some of the homologous series obtained. Use this intuition to build and save an internal calibration list by clicking “Calibrate” and “Edit Reference Mass Lists…”. The empirical formula entered is automatically converted to an m/z value for the specified ion. Note: the mass of the electron actually matters with FT-ICR spectral assignments.
5. Once your list is built, click “Calibrate” – “Internal…”. Select your series you created or an existing one. Do not panic if the errors for the masses after recalibration are high. Usually this means the wrong peak was automatically picked due to low abundance of the correct peak. You can zoom in on the spectra with the window open and select the peak for the corresponding reference mass.
6. Typically, quadratic calibration produces the best results. Select this from the dropdown menu and click recalibrate.

7. It's also important to limit the m/z range of what peaks will be assigned by using the "Exclusion Masses" tab to build a list of individual masses or ranges to exclude from analysis. This is found by pulling up the "Parameters" pane.
8. To perform the full formula assignment go to "Chemistry" and click "Parameters".
9. Select the ions you expect to be forming in the spectra based on the analysis. For LIAD-APPI the panel typically appeared as such:

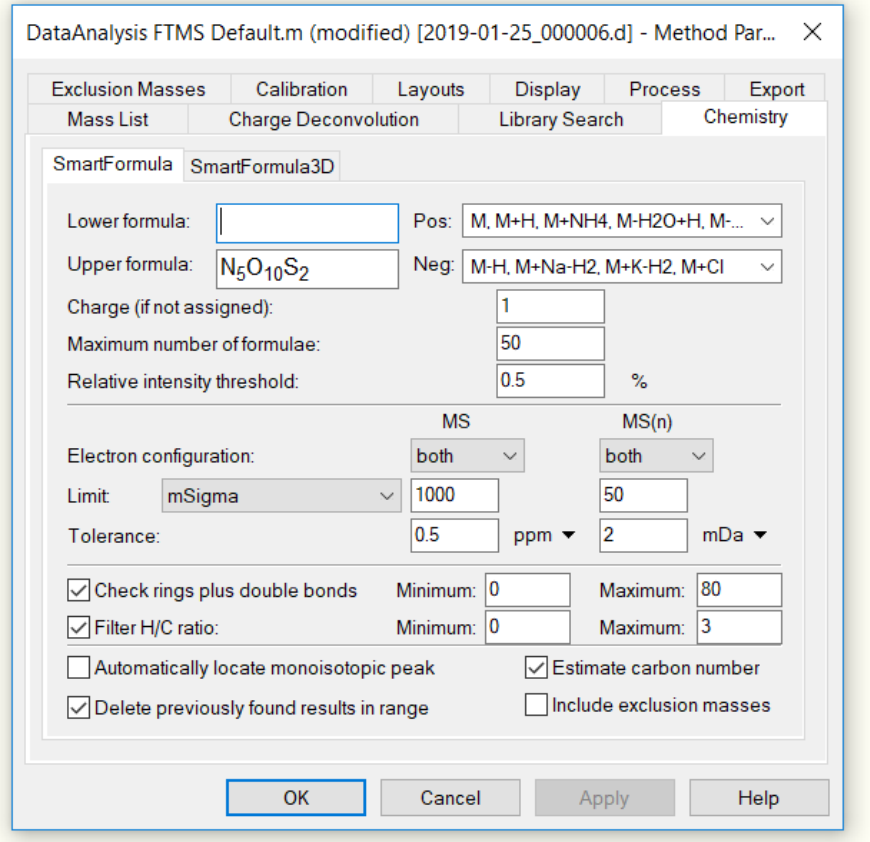

10. IMPORTANT: It is crucial to appropriately analyze the "Relative intensity threshold" parameter by understanding what the relative intensity of a S/N = 4 (or whatever S/N threshold you find suitable) corresponds to. This varies over the m/z range where higher m/z's typically have higher relative intensity and lower S/N.

There should just be a S/N threshold but this is what the software is limited to. If the threshold is too low, the software will assign a ton of compounds within your ppm tolerance but this will lead to uniformly distributed error, e in the interval $[-ppm_{tol},\ ppm_{tol}]$. This would indicate a low confidence in the assignments made.

11. Click APPLY and OK.
12. Click SmartFormula to run the analysis under the standard parameters on the new screen.
13. After the job is finished, a table will be formed under the SmartFormula tab. Right click the table and go to “Layouts”. If you want to use the python figure generator described next, make sure to include “Measured Intensity” and “rdb”. Also make sure that the rows are sorted by “Measured m/z”.
14. This is the cumbersome part. Click a row in the SmartFormula output table and press CTRL+A. This will select the table which you can copy with CTRL+C. This takes awhile and causes the program to not respond. For the moment, it’s the only means to get the information exported.
15. Paste this information into an empty Excel table by selecting the top leftmost cell and pressing CTRL+V. Save this table as a UTF-8 formatted .csv file under the directory in which you will run the plot generation program. Save it as a unique name where the only “.” is before the “csv” extension. It’s useful to save as something corresponding to the analysis as the figures are auto assigned names.

16. Open the “compound_id.ipynb” iPython notebook in Jupyter Notebook installed with the Anaconda 3.7 python package management suite. Found here: https://www.anaconda.com/distribution/
17. In one of the first cells, there is a string variable “file”. Assign your filename to this variable.
18. Click Cells-Run All.
19. Your plots should be generated and saved. You can preview them in the notebook but it will be blurry. Feel free to edit the code as needed to perform whatever tasks you like. A lot of the difficult class and heteroatom counting is done in the notebook.

APPENDIX B. MULTIVARIATE ANALYSIS OF MASS SPECTROMETRY DATA FROM CHEMICALLY COMPLEX FOOD SAMPLES – A DATA PROCESSING INVESTIGATION

The work presented in this section pertains to studies performed in 2017 at QuoData Quality & Statistics, Berlin, Germany. It serves to demonstrate some useful information regarding data processing of mass spectra and the extents to which principal component analysis of multivariate data can be applied.

B.1 Introduction

Food fraud is a significant area of concern for public health, the food industry, the beverage industry, and virtually any industry that relies on the harvest, production, or sale of ingestible products. Development of methods to detect food fraud has poses a significant challenge to regulatory and standards agencies due to the significant variability and chemical complexity of food samples. Therefore, many chemical analysis techniques and data processing methods have been developed to assess this problem, even within specific food types such as olive oil [205-207]. In many cases, some combination of mass spectrometry and multivariate analysis or machine learning has been employed.

Mass spectrometry (MS) is a diverse field with many different techniques to analyze complex biological samples. Three leading techniques include electrospray ionization (ESI) , gas chromatography MS (GC-MS), or matrix-assisted laser desorption ionization MS (MALDI-MS). Each technique in general includes a mechanism to ionize and evaporate chemical samples so that the distribution of molecular species can be

determined by the mass spectrometer. The resulting data is then a large spectrum with many peaks and thousands of data points. Due to the different electronics, settings, performance capabilities, and manufacturer preferences, these mass spectrometers can output very different spectra between instruments from the perspective of a pure data analyst. Therefore, comparing raw data between instruments poses a difficult task considering each generates data with a systematic variance relating to nothing more than the varied components between instruments.

To increase comparability of data from different instruments, many manufacturers have included data treatment algorithms in their software. These algorithms perform manipulations on the data such as normalization, noise reduction, peak alignment, signal smoothing, baseline subtraction, and many more. Each of these processing steps has underlying mathematical theory and each manufacturer most likely employs a different algorithm to apply those theories to the data. While these techniques enhance visual comparability, the actual effects of the algorithms could introduce artificial variance which can ultimately affect the outcome of a multivariate classification method. For example, Instrument 1 employs normalization, baseline correction, and peak alignment using some specific mathematical computation and Instrument 2 does the same using a different mathematical computation. While necessary to achieve (at least) visual comparability between instruments, the variance introduced to the different spectra could create different peak values, peak shifts, or peak eliminations that ultimately could introduce artificial variance into some data classification routine's outcome. Therefore, it is necessary to understand the degree of this variation and qualify various data processing methods to minimize any artificial variance. In addition, it would be beneficial to characterize the

effect of the variance introduced by various processing methods as statistically significant or insignificant.

Ultimately, the goal is to pre-process the data in so that all samples are on comparable scales and apply a multivariate analysis method to classify samples as belonging to a certain population or not belonging. In general, this can be accomplished by "scoring" the individual samples and then using a distance metric to describe the distribution of the individual population clusters. These individual sample scores can then be evaluated against the population distributions to determine a classification. An example of a common approach for this is principal components analysis (PCA) followed by some clustering protocol of the data in the principal component space. For clarity, we will refer to a single spectra taken from a real sample as an *example* and each intensity measurement along that spectra as a *feature*. Thus, a typical spectra-only data set would consist of m examples and n features, a common notation in data science.

B.2 Incorrect Data Processing Approaches

Magnitude of signal is a trait that must always be accounted for between examples by some form of normalization. A common technique to normalize a single spectra is to divide the spectra by the highest intensity point found within the spectra. This results in the highest peak being equal to one and all others less than one. While this is a useful visual tool, one can easily realize that for a set of spectra with the same base peak the variance for that peak will be eliminated. This is especially problematic since variance of the most prominent peaks can be of large importance.

For a set of spectra from a certain sample group, one can calculate a mean μ, and standard deviation σ for each peak. Using the traditional definition μ/σ, one can calculate the S/N for each point. However, due to the substantial variation in large peaks in MS, if one were to keep only those peaks above a certain S/N threshold, much of the important data might be removed following this definition. Furthermore, this relies on the arbitrary definition of what constitutes a good S/N value. (Typically S/N > 3 is considered good)

Savitzky-Golay filtering is an approach used to filter the noise out of spectral data [208]. This algorithm uses a spectral window and the derivative within that window to determine the noise in the signal and smooth the data. It can be considered as a generalized moving average filter. Unfortunately, this requires several parameter inputs. With slight alteration of these parameters, the signal can be over-smoothed which of course is undesirable and may fail given different instrumental resolutions and varied resolution across a single spectral example.

Asymmetric least-squares baseline determination is a method to determine and remove the baseline of a spectrum. This algorithm approximates the baseline of the data through an iterative process which is based on the minimization of a penalized least squares function. The performance does a good job of selecting the base of the noise however, it has a tendency to leak into parts of the real peaks. Furthermore, it requires a careful selection of parameters for each spectra. There exists no computationally inexpensive routine to select the optimal parameters for each spectra and because of the peak leaking, it is not recommended this baseline determination be used.

B.3 Suggested Data Processing

A very simple technique which simply uses a specified nth-order polynomial,

$f(x) = a_0 + a_1x^1 + \cdots + a_nx^n$ to match the baseline. This process known as polynomial regression baseline correction, is solved using least squares regression for the coefficients $a_0, \ldots, a_n$. Because the spectrum contains many points, using a sufficiently low n results in a smooth curve running along the base of the spectrum with no peak selection. For the analyses performed in this work, an order 5 polynomial seemed to do a nice job of baseline correction for MALDI data. Based on the following plot:

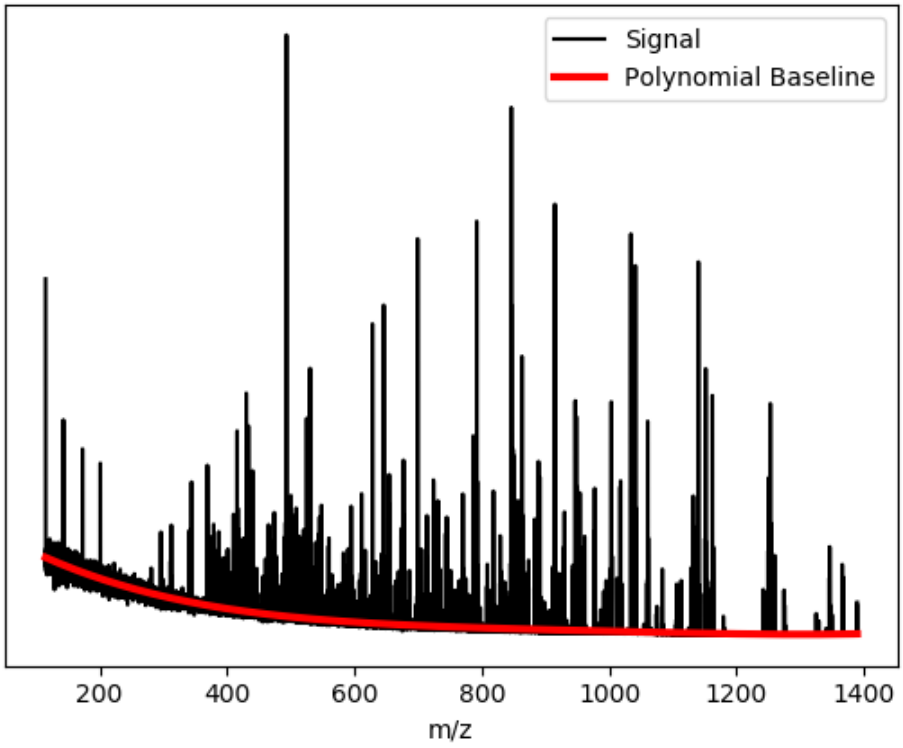

Figure B.1 Baseline determination (red) from MALDI spectrum (black) generated from 16 protein fingerprints.

The baseline smoothly traverses though the middle of the noise where, upon subtraction, this would yield a flattened curve for this MALDI example. Baseline rise is an observed trait of many MALDI spectra and is thought to arise from detector swamping by the MADLI matrix.

The restrained moving average baseline correction technique uses a moving average to discriminate peaks from noise. It typically tends to capture the highly non-uniform low-mass range baseline seen in MALDI spectra as well as capturing the rise in baseline seen near large peaks. The only input required is the window size which is recommended to take integer values between 3-5 for high resolution MALDI data.

Wavelet transform soft-threshold filtering is a better approach for removing the noise from spectral data. In a very general sense, this method transforms the data using a wavelet function and de-noises the spectra based on a soft thresholding technique. For a detailed analysis see Donoho [209]. This does a good job of retaining original peak heights while smoothing the low-lying noise in the spectra. The main function of this method is to de-noise the spectra to maximize peak selection accuracy in the alignment algorithm. Therefore, for noisy spectra it is important to perform this prior to peak alignment. This does not have much influence on the outcome of PCA.

Peak alignment is also a particularly important step for pre-processing when considering a comparison across multiple spectra. Most mass spectrometry software packages include an algorithm for alignment of peaks between different spectra. Typically, an average spectrum or a well calibrated reference spectrum from a particular population is used to align peaks from all other spectra. This aids in deconvolution of the systematic

mass spectrometer differences from the actual sample differences. This has been shown to be an important step for data standardization for the purpose of multivariate analysis [210, 211].

Probabilistic quotient (PQ) normalization is also a useful form of normalization for placing multiple spectral datasets on a comparable magnitude scale. This form of normalization is given by a special procedure in Dieterle et al. [212]. In their work, the PQ normalization is proposed as a more appropriate alternative to the integral normalization. Because the purpose of normalization is essentially scaling the concentrations of all species to similar virtual level, each species, or feature should be scaled by its most probable dilution factor. They assert this to be a more general form of normalization due to the assumed absence of interferences inherently assumed with integral normalization in NMR spectra. The PQ normalization uses a median reference spectrum from the data set c_0, usually determined from an included reference population, calculates quotients $f_i / c_{0,i}$ from a sample F with features f_i and corresponding median feature $c_{0,i}$, finds the median of these quotients as the scalar q_0, and normalizes the spectrum by the quotient, F/q_0. Total ion count normalization is a suggested first step to place spectra with different intensities on a similar scale.

It should be noted, that these are the recommended data processing steps to place all spectra on a similar, comparable scale while not losing significant information in the data set. These are suggested to precede any multivariate analysis that will score the data and use those scores for classification. If quantitative information regarding sample

concentrations is needed, these steps would not be appropriate and more specific experimental protocol would need to be employed during the original data gathering.

B.4 Testing

To test various pre-processing steps, qualitative analysis of the principal components score plots is employed. The idea is that populations of samples (spectra) from different species should appear as distinct clusters.

PCA is a powerful technique that is used to perform various tasks and analyses on high dimension data. It is useful in decreasing the difficulty for interpretation of high dimension data sets by reducing the data into only a few principal component scores (PCs). To find the (PCs), one must first find principal component axes of the data. These axes are defined as a set of ordered orthonormal vectors starting with the first axis which maximizes the variance of the dataset in all dimensions. The second axis maximizes the variance in an orthogonal direction to the first and this process continues until a number of axes equal to the number of samples or features, whichever is smallest, are found. These axes are arranged in order according to the magnitude of their eigenvalue. The best way of accomplishing this is by the singular value decomposition (SVD) of a centered data matrix X. For a $n\,x\,m$ matrix X, where n is the number of features and m is the number of examples, its SVD is given by:

$$X = USV^T$$

where, U is the eigenvector matrix of XX^T, S is a diagonal matrix of singular values, and V is the eigenvector matrix of X^TX.

For the given orientation of X, the columns of US or SV^T are found to be the PCs. These columns are projections of the data on the new principal component axes which typically capture the variance of the data set in exponentially decreasing order. Below is an example of a scree plot determined by a two class, artificially generated yeast mass spectrum dataset (80 examples, 40 per class) illustrating the percentage of variance described by each principle component.

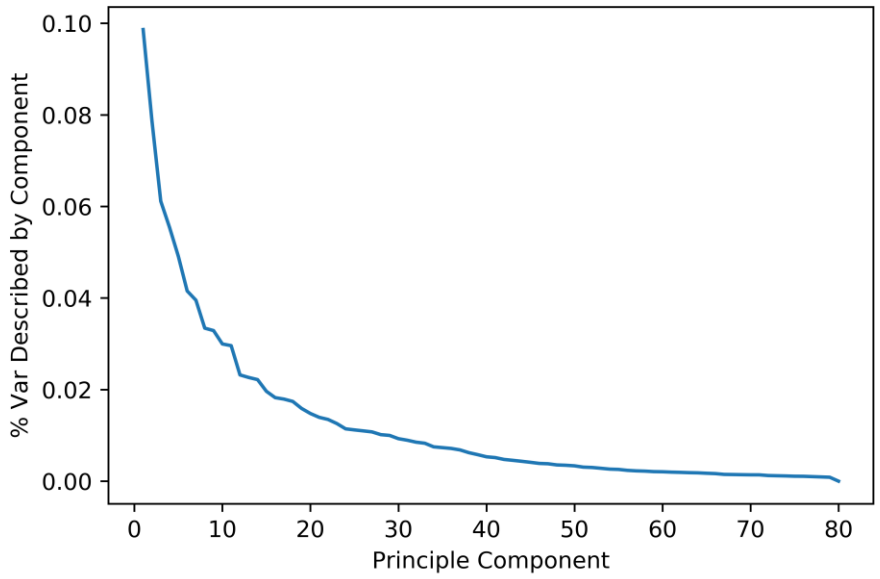

Figure B.2 Scree plot demonstrating the percent of the variance in the data described by each principle component or principle component axis. Axes were sorted by the weight held in each of their singular values, converted to eigenvalues to generate this plot.

In this plot, 95% of the variance in the data is described by 51 components. The weight that each principle component describes is given by the relative magnitude of the individual eigenvalues λ, of the covariance matrix which are equal to square of the singular values, s obtained from the SVD decomposition.

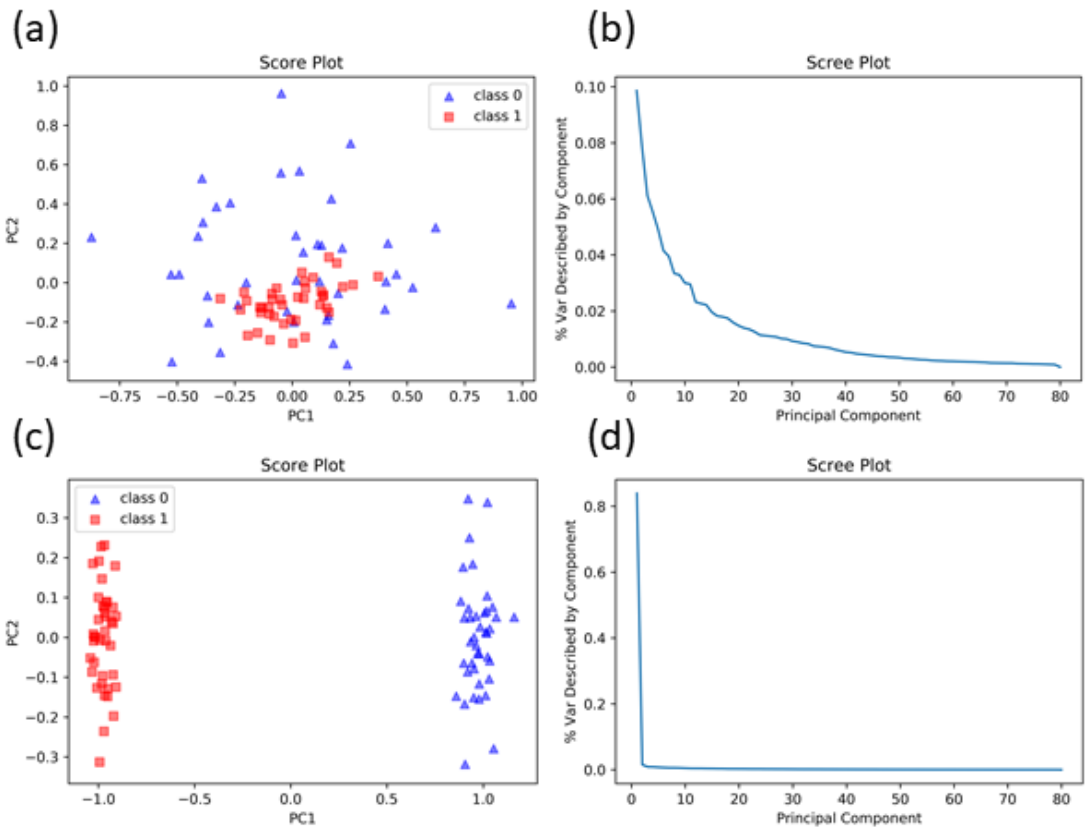

Figure B.3 (a) and (b) are the score and scree plot for a generated dataset consisting of two populations of 40 spectra based on 16 protein fingerprints only differing by one major peak of a protein fingerprint between the populations. Class 0 was also generated with an extra 10% of random peak variance. (c) and (d) are the score and scree plots for a dataset generated from a 16 protein fingerprint set where each class differed by an entire fingerprint (~10-15 peaks).

Thus, in only a few dimensions, one can analyze the relationship of all samples by a score plot. To obtain scores for each spectrum (or example) one must take the PCs as the rows of SV^T. The scores represent a value given to each spectrum when projected on the principal component axes. In the scatter plots (Figures B.3a, B.3c), one will observe

clusters of points which represent populations in the data. The idea being that the samples that are scored similarly must be related. The set of scree and score displayed are examples for easily differentiable two population datasets and a two population dataset that does not show clear separation along the first two principal component axes. The spectra used for Figure B.3c and B.3d were artificially generated from a subset of protein fingerprints from a yeast protein database where each class differed by one entire fingerprint (~20 - 80 peaks). This illustrates the success of this visualization when the sets are significantly different. The success of this representations ability to describe the high-dimension data in just two dimensions is given by sharp decline in magnitude of the weights or eigenvalues for the principal component axes. Notice that for Figure B.3d, the data can be mostly represented by the first few principal components. In Figure B.3a, B.3b, only a single peak between the spectra in the datasets was differed. Because of the lack of differing peaks between the two samples, the populations are not discerned well by the first few components as given by the score and scree plots. Note that these are only the first few components' representation's of the data and that less significant components may capture the minute differences in the populations.

In addition to analysis of clusters via the principal component scores of the samples, two methods were considered for finding unique and discriminant features of the spectral sets. The first method involves finding the outliers of the PCA loading plot of the m/z points (i.e. features). These values can be found by taking the columns of US for the matrix orientations described. These outliers correspond to large peaks with significant variance across all samples.

A second method was employed under the assumption that the large variance peaks in known, alternative populations to the reference should be identified as falling outside a statistical interval centered on the mean values of the individual m/z points across a reference population. The method is employed as follows:

- Define an average and standard deviation for all m/z points in a reference population
- Count how many times the matching m/z values from other samples/populations fall outside of the interval $\left[\mu_{i,ref} - 3\sigma_{i,ref} \ , \ \mu_{i,ref} + 3\sigma_{i,ref}\right]$
- Multiply the count list by each m/z standard deviation for all samples outside of the reference.
- Sort the list to find which m/z values have the highest count*σ.

For proteomic data sets, the method returned similar m/z peaks as the PCA outlier method due to large amounts of large shared peaks with high variance. However, for high mass MALDI datasets with fewer distinct yet broader peaks, the method returned the differing peaks in the spectra.

B.5 Continued Steps

The above descriptions of various pre-processing on MS data and analysis by PCA is a beginning framework for the ultimate goal of classifying unknown food samples by their mass spectra and determining error in the analysis techniques using the MS data alone. In general, the two major analysis steps each have a goal that need to be met. The first is that the pre-processing must place all spectra on a comparable basis without removing important information. The second goal is to use a statistically rigorous protocol to define:

- Distance of a sample from a population distribution
- Distance of two population distributions

With an appropriate distance, whether this is calculated from the clusters in PCA or some other generalized N-dimensional distance metric, one can establish more interpretable and high-fidelity statistical methods for the identification and classification of food samples.

B.6 Python source-code

Code for the data generation can be found at https://github.com/kbenham4102/MSGen containing a function module specsim.py to generate the data and a script datagen.py to generate the entire dataset from a subset of protein fingerprints formatted as the NIST yeast proteomics database shown in the yeast1.txt example. Datagen.py includes the following parameters:

```
respwr = 50000 # Resolving power, best left alone.
numsamp = 40 # Number of spectra to generate for the set
Enoise = 5e-4 # Electronic noise level
pkv = 0.10 # Random variance of peak heights
bsl = False # Whether to introduce baseline asymmetry
misal = False # Whether to add small variation in peak
              # position
pts = 30000 # Array length, carefully tuned wrt respwr
blev = 0.05 # exponential factor for baseline asymmetry
```

General protocols for PCA can be found at https://github.com/kbenham4102/PCAMS but for many of the plots seen here, the code was written and executed ad hoc.

APPENDIX C. MHCD SOFTWARE, DESIGN NOTES, AND MAINTENANCE

C.1 Software Requirements

Software for the MHCD devices is crucial to running these devices smoothly and effectively. The package needed can be found under the Orlando lab file server with appropriate permission. To run the control software you will need:

1. LabVIEW 2016 or later
2. DAQmx Driver Package from National Instruments

C.2 Software Operation

The VUV Controller software is primarily meant to control the mass flow controllers which introduce the plasma gas to the device at a fixed total flow rate and mixture concentration. This section will go over how to accomplish this and some features of the software. Other features of the software include monitoring the discharge characteristics through a circuit network like that described in chapters 2 & 3 but is no longer connected or needed for mass spectrometry experiments.

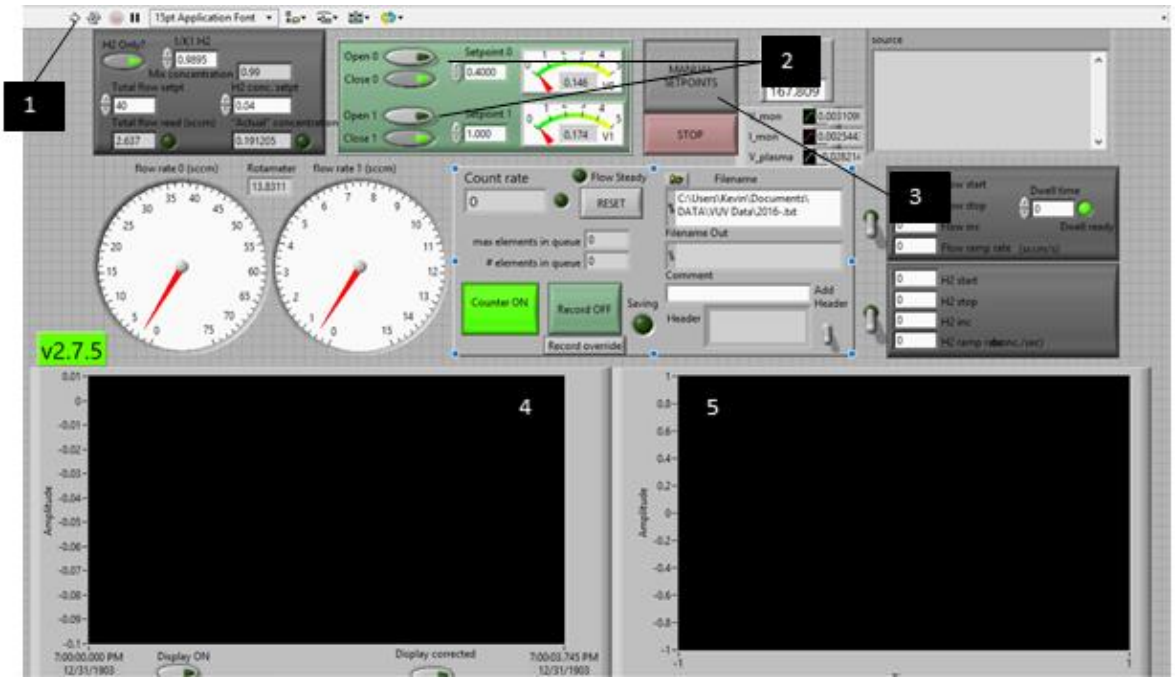

Figure C.1 View of the VUV Controller main panel. 1 indicates the start button at the top level. 2 points to the mass-flow-control (MFC) switches. Note: if both Open and Close are pressed (or not pressed) as indicated by the bright green button, then the MFCs stay closed. 3 Points to the MANUAL SETPOINTS and STOP button. The MANUAL SETPOINTS button indicates the MFCs are set to flow at maximum capacity given a pressurized input. If pressed, this switches operation to an AUTO SETPOINTS where the MFCs are set to flow at the specified total flow setpoint with specified gas mix concentration (panel right of label 1). Panels 4 and 5 are for monitoring the IV characteristics of the discharge and are typically not used for mass spectrometry experiments.

A special note should be made for Figure C.1 in that the current set up is meant to run a pure neon gas through MFC 0 and pure hydrogen MFC 1. The “H2 Only” button indicates that a pure gas is to be flowing through MFC 1 with a flow rate value determined by the “1/K1” setting. The K1 values can be found in the user manuals for Omega MFCs for a number of common gases. Typical start up and operation is described in more detail with Appendix A.

C.3 Device Design, Geometry, and Fabrication

The overall device design is discussed in more detail in chapters 2, 3 and 4. However, not mentioned are the specific dimensions for the electrodes. Currently, the device is built such that there are circular electrodes with centered and aligned holes. The dimensions of these components can be seen in Figure C.2.

C.4 Maintenance - Electrode Replacement

The following are point wise instructions for replacing the electrodes of the current cubic device configuration described first in chapter 3. Each point must be read carefully before executing. You will need:

- Allen wrench set

- 0.003 in thick stainless-steel wire

- 2x 100 μm thick Mo electrodes and 100 μm thick mica layer with aligned holes

- Clean bench with an adjustable clamp

1. Remove the device gas lines, high-voltage (HV) wire, and ground wire from the device.

2. Take the device to the clean workbench and remove the 4, 2-56 socket cap screws holding the device layers together and the 0-80 flat head screws holding the plastic separator to the device body.

3. Place the window assembly and plastic separator aside, it may be a good idea to wipe these down with isopropyl alcohol.

4. The foils should fall out, place these aside for evaluation if needed. Clamp the device with the foil side up to the table.

5. Take the 0.003 in. stainless steel wire and thread this through the center gas channel of the device, exiting where the electrodes were placed. Tape the end of the wire at the rear of the device so that it doesn't slip out of the channel.

6. Thread the anode, mica and, cathode onto the open end of the wire. Center these in a stack on the circular cut-out on the face of the device body.

7. Carefully thread the plastic separator on the wire as to not disturb the foils. Note: there is a 0-80 cap screw which makes.

8. Replace the 0-80 flathead screws to secure the plastic separator. Initially, very lightly tighten. This is important for the next step.

9. Grab both ends of the wire and carefully work to center the aligned electrode holes in the center of the plastic separator hole. This must be done by eye to the best of ones ability.

10. Once centered, carefully tighten the 0-80 flathead screws, clamping the plastic separator onto the foils. Alternate tightening screws every few threads. Before removing the wire, make sure it can be pulled freely through the holes of the electrodes with minimal resistance. Any resistance indicates a kink in the 100 μm diameter channel which can disrupt gas flow and hamper discharge characteristics.

11. After securing the plastic separator, test the top electrode (cathode) for connectivity with the HV wire using a multimeter. If no connectivity is detected, this probably means a

poor contact was made between the 0-80 cap screw in the plastic separator. Causes may be disconnected HV wire, the cap screw was depressed into the plastic separator too far, or foil was misaligned.

12. Secure the window assembly to the device to seal and complete the rebuild. Be sure to inspect for any significant gaps in the construction. The parts should be flush.

13. The rebuild is finished. Reconnect device gas lines and voltage wiring to test. A substantial N_2 purge should be used as well as a longer plasma gas purge. It may take a moment for plasma voltage to stabilize upon the first startup.

C.5 Design Notes – Pressure Simulations

As a note to the reader regarding the design of this device, several pathways for optimization have been discussed. One of these is managing gas pressure via flow. Because the formation of VUV light is generally dependent on a 3-body collision between rare gas species to form excimers, these can be enhanced by optimizing flow conditions to maximize this formation while preserving low-power consumption IV characteristics. In pursuit of developing these devices, we have demonstrated preliminary CFD calculations indicating a small pressure increase for a neutral gas with these devices. This effect can be seen in Figure C.2 for a neutral He gas flowing through the gas channel to hollow structure in a simplified geometry. The popular $k-\epsilon$ turbulent flow model was used as normal forces were expected to be experienced as the fluid reaches the outer surface of the anode of the device. A 2D axisymmetric geometry model was used for the calculation given the symmetry of the device where the inlet boundary condition was set at 40 mL/min He. The results indicate a small pressure spike of ~ 1% from atmoshpere initially entering the

hollow and near the edges of the cathode hollow. This would indicate possible pressure increase aiding in the excimer formation. However, a couple of caveats must be noted. For

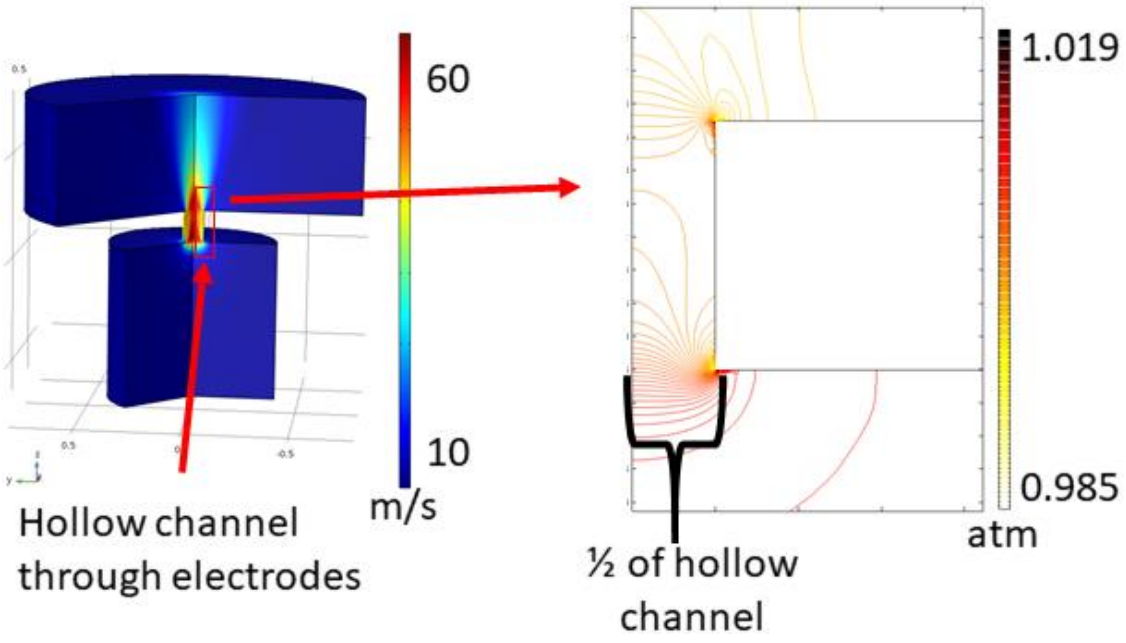

Figure C.2 Simulation of fluid flow through a simplified geometry of the MHCD device gas channel to electrode hollow structure. The jet like feature emitting from the cathode side of the structure would be consistent with observed plasma jets emitted from these devices.

one, this is a neutral flow which does not capture the full dynamics of the hydrodynamic transport environment occurring in many plasma systems. While this is necessary to capture the full behavior of the real system, the computational complexity would be very large for a system as we have described here. Despite this, some have attempted to accurately simulate the flow and plasma dynamics of these systems with a significant degree of computational effort relative to this study [213]. Therefore, these are important considerations when designing the next generation of these versatile devices.

APPENDIX D. OPERATING PROCEDURE FOR THE IMATRIXSPRAY OPEN-SOURCE DEPOSITION SYSTEM

One of the key components enabling confidence in the LIAD-APPI studies discussed is the iMatrixSpray deposition system used in chapters 2 and 3. This system enabled the deposition of standard and mixture samples in both polar and non-polar solutions with a high degree of surface homogeneity. It's standard operating procedure is shown below.

START UP:

1.) Open N2 valves on N2 tank opposite of the sprayer fume hood. Ensure that the line is securely connected to the quick connect at the back of the iMatrixSpray.
2.) Press the SILVER button to start the system. Should light up blue if plugged in.
3.) Using a SmartPhone, log in to the WiFi LAN generated by the system:
    a. Network Name: iMatrixSpray
    b. Password: 0000000000
4.) Using your phone's web browser, go to http://10.10.10.10
5.) When the control page loads, press the INIT button on the page.

OPERATION:

1.) On the right of the control page set the solution you wish to deposit, A, B, or C.
2.) Press SPRAY. The system will now go through its purging, cleaning, cleaning and spraying cycles with the parameters that are set.

GUIDELINES:

1.) Unless special circumstances are encountered, the only parameters that need be adjusted are the Density, Cycles, and Delay parameters. In general:
    a. Density, between 1-5 $\mu L/cm^2$
    b. Cycles, as many as needed. At least 10 for 5% homogeneity error. more cycles with low concentrations = higher surface homogeneity.
    c. Delay, 0 s unless using a solvent with low volatility. Set as needed.
2.) Concentrations of deposition solutions should not exceed ~10 mM. SYSTEM CAN BE CONTAMINATED AND CONTAMINATE OTHER USERS SAMPLES.

SHUT DOWN:

1.) Wait for iMatrixSpray to finish all cycles. The needle chassis will return to the overhead, centered position.
2.) On the control web page, press MOTORS OFF.
3.) Press the silver button to turn off.
4.) Close N2 valves

APPENDIX E. PYTHON CODE FOR PETROLEOMICS PLOT GENERATION

Important: To use this program one must have installed the Anaconda 3 software package (https://www.anaconda.com/distribution/) and saved your data files in a UTF-8 comma-separated values (.csv) format. These must include the columns *rdb*, *I*, *Meas. m/z*, *m/z*, and *Ion Formula* corresponding to the rings and double-bonds, measured intensity, measured mass-to-charge ratio, formula mass-to-charge ratio, and assigned ion formula, respectively. These can be included in the columns of data returned by the Bruker DataAnalysis' SmartFormula routine when they are copy and pasted to a .csv file. The table must be sorted by *Meas. m/*z in the software before copy-pasting into the .csv file.

The current build for the plots shown here can be found at the public github repository https://github.com/kbenham4102/petro-analyze . Download this and place the formula assignment data to be processed in the same directory as the *compound_id.py* script. Run the program to generate plots as follows:

```
$ python compound_id.py -data YourDataFile.csv [Options]
```

Where "options" can be found by running:

```
$ python compound_id.py -h
```

This returns a help menu with all of the parameters that can be specified and a short description.

REFERENCES

REFERENCES

1. Benham, K., Hodyss, R., Fernandez, F.M., Orlando, T.M.: Laser-Induced Acoustic Desorption Atmospheric Pressure Photoionization via VUV-Generating Microplasmas. Journal of The American Society for Mass Spectrometry. **27**, 1805-1812 (2016)

2. Benham, K., Fernández, F.M., Orlando, T.M.: Sweep Jet Collection Laser-Induced Acoustic Desorption Atmospheric Pressure Photoionization for Lipid Analysis Applications. Journal of The American Society for Mass Spectrometry. (2019)

3. Kauppila, T.J., Kostiainen, R.: Ambient mass spectrometry in the analysis of compounds of low polarity. Analytical Methods. **9**, 4936-4953 (2017)

4. Yamashita, M.F., John B.: Electrospray Ion Source. Another Variation on the Free-Jet Theme. Journal of Physical Chemistry. **88**, 4451-4459 (1984)

5. Taylor, S.G.: Disintegration of water drops in an electric field. Proceedings of the Royal Society of London. Series A. Mathematical and Physical Sciences. **280**, 383-397 (1964)

6. Iribarne, J.V.: On the evaporation of small ions from charged droplets. The Journal of chemical physics. **64**, 2287 (1976)

7. Dole, M., Mack, L.L., Hines, R.L., Mobley, R.C., Ferguson, L.D., Alice, M.B.: Molecular Beams of Macroions. The Journal of chemical physics. **49**, 2240-2249 (1968)

8. Mack, L.L., Kralik, P., Rheude, A., Dole, M.: Molecular Beams of Macroions. II. The Journal of chemical physics. **52**, 4977-4986 (1970)

9. Murphy, R.C., Axelsen, P.H.: Mass spectrometric analysis of long-chain lipids. Mass Spectrometry Reviews. **30**, 579-599 (2011)

10. Hsu, F.-F.T., John: Structural Determination of Sphingomyelin by Tandem Mass Spectrometry With Electrospray Ionization. Journal of The American Society for Mass Spectrometry. **11**, 437-449 (1999)

11. Byrdwell, W.C.: Atmospheric Pressure Chemical Ionization Mass Spectrometry for Analysis of Lipids. Lipids. **36**, 327-346 (2001)

12. Vrkoslav, V., Rumlova, B., Strmen, T., Nekvasilova, P., Sulc, M., Cvacka, J.: Applicability of low-flow atmospheric pressure chemical ionization and photoionization mass spectrometry with a microfabricated nebulizer for neutral lipids. Rapid Communications in Mass Spectrometry. **32**, 639-648 (2018)

13. Niessen, W. (3rd Edition ed.). CRC Press, Taylor and Francis Group, Boca Raton, Florida (2006)

14. Trickl, T., Cromwell, E.F., Lee, Y.T., Kung, A.H.: State-selective ionization of nitrogen in the X 2Σ+gv+=0 and v+=1 states by two-color (1+ 1) photon excitation near threshold. The Journal of chemical physics. **91**, 6006-6012 (1989)

15. Robb, D.B., Covey, T.R., Bruins, A.P.: Atmospheric Pressure Photoionization: An Ionization Method for Liquid Chromatography-Mass Spectrometry. Analytical Chemistry. **72**, 3653-3659 (2000)

16. Kauppila, T.J., Kostiainen, R., Bruins, A.P.: Anisole, a new dopant for atmospheric pressure photoionization mass spectrometry of low proton affinity, low ionization energy compounds. Rapid Communications in Mass Spectrometry. **18**, 808-815 (2004)

17. Kauppila, T.J., Kuuranne, T., Meurer, E.C., Eberlin, M.N., Kotiaho, T., Kostiainen, R.: Atmospheric Pressure Photoionization Mass Spectrometry. Ionization Mechanism and the Effect of Solvent on the Ionization of Naphthalenes. Analytical Chemistry. **74**, 5470-5479 (2002)

18. Robb, D.B., Blades, M.W.: Factors affecting primary ionization in dopant-assisted atmospheric pressure photoionization (DA-APPI) for LC/MS. Journal of The American Society for Mass Spectrometry. **17**, 130-138 (2006)

19. Cai, Y., Kingery, D., McConnell, O., Bach, A.C.: Advantages of atmospheric pressure photoionization mass spectrometry in support of drug discovery. Rapid Communications in Mass Spectrometry. **19**, 1717-1724 (2005)

20. Robb, D.B., Blades, M.W.: Effects of solvent flow, dopant flow, and lamp current on dopant-assisted atmospheric pressure photoionization (DA-APPI) for LC-MS. Ionizationvia proton transfer. Journal of the American Society for Mass Spectrometry. **16**, 1275-1290 (2005)

21. Itoh, N., Aoyagi, Y., Yarita, T.: Optimization of the dopant for the trace determination of polycyclic aromatic hydrocarbons by liquid chromatography/dopant-assisted atmospheric-pressure photoionization/mass spectrometry. Journal of Chromatography A. **1131**, 285-288 (2006)

22. Karuna, R., von Eckardstein, A., Rentsch, K.M.: Dopant assisted-atmospheric pressure photoionization (DA-APPI) liquid chromatography–mass spectrometry for the quantification of 27-hydroxycholesterol in plasma. Journal of Chromatography B. **877**, 261-268 (2009)

23. McCulloch, R., Alvaro, A., Astudillo, A.M., del Castillo, J.C., Gómez, M., Martín, J.M., Amo-González, M.: A novel atmospheric pressure photoionization – Mass spectrometry (APPI-MS) method for the detection of polychlorinated dibenzo P-dioxins and dibenzofuran homologues in real environmental samples collected within the vicinity of industrial incinerators. International Journal of Mass Spectrometry. **421**, 135-143 (2017)

24. McKenna, A.M., Purcell, J.M., Rodgers, R.P., Marshall, A.G.: Heavy Petroleum Composition. 1. Exhaustive Compositional Analysis of Athabasca Bitumen HVGO Distillates by Fourier Transform Ion Cyclotron Resonance Mass Spectrometry: A Definitive Test of the Boduszynski Model. Energy & Fuels. **24**, 2929-2938 (2010)

25. Vaikkinen, A., Shrestha, B., Kauppila, T.J., Vertes, A., Kostiainen, R.: Infrared laser ablation atmospheric pressure photoionization mass spectrometry. Analytical Chemistry. **84**, 1630-1636 (2012)

26. Takats, Z., Wiseman, J.M., Gologan, B., Cooks, R.G.: Mass Spectrometry Sampling Under Ambient Conditions with Desorption Electrospray Ionization. Science. **306**, (2004)

27. Haapala, M.P.l., Jaroslav; Saarela, Ville; Arvola, Ville; Kotiaho, Tapio; Ketola, Raimo A.; Franssila, Sami; Kauppila, Tiina J.; Kostianen, Risto: Desorption Atmospheric Pressure Photoionization. Analytical Chemistry. **79**, 7867-7872 (2007)

28. Cody, R.B., Laramée, J.A., Durst, H.D.: Versatile New Ion Source for the Analysis of Materials in Open Air under Ambient Conditions. Analytical Chemistry. **77**, 2297-2302 (2005)

29. Symonds, J.M., Galhena, A.S., Fernández, F.M., Orlando, T.M.: Microplasma Discharge Ionization Source for Ambient Mass Spectrometry. Analytical Chemistry. **82**, 621-627 (2010)

30. Weston, D.J.: Ambient ionization mass spectrometry: current understanding of mechanistic theory; analytical performance and application areas. The Analyst. **135**, 661-668 (2010)

31. Hsu, C.-C., Chou, P.-T., Zare, R.N.: Imaging of Proteins in Tissue Samples Using Nanospray Desorption Electrospray Ionization Mass Spectrometry. Analytical Chemistry. **87**, 11171-11175 (2015)

32. Jarmusch, A.K., Pirro, V., Baird, Z., Hattab, E.M., Cohen-Gadol, A.A., Cooks, R.G.: Lipid and metabolite profiles of human brain tumors by desorption

electrospray ionization-MS. Proceedings of the National Academy of Sciences. **113**, 1486-1491 (2016)

33. Zhou, Z., Zare, R.N.: Personal Information from Latent Fingerprints Using Desorption Electrospray Ionization Mass Spectrometry and Machine Learning. Analytical Chemistry. **89**, 1369-1372 (2017)

34. Venter, A., Sojka, P.E., Cooks, R.G.: Droplet Dynamics and Ionization Mechanisms in Desorption Electrospray Ionization Mass Spectrometry. Analytical Chemistry. **78**, 8549-8555 (2006)

35. Andrade, F.J., Shelley, J.T., Wetzel, W.C., Webb, M.R., Gamez, G., Ray, S.J., Hieftje, G.M.: Atmospheric Pressure Chemical Ionization Source. 2. Desorption−Ionization for the Direct Analysis of Solid Compounds. Analytical Chemistry. **80**, 2654-2663 (2008)

36. Ratcliffe, L.V., Rutten, F.J.M., Barrett, D.A., Whitmore, T., Seymour, D., Greenwood, C., Aranda-Gonzalvo, Y., Robinson, S., McCoustra, M.: Surface Analysis under Ambient Conditions Using Plasma-Assisted Desorption/Ionization Mass Spectrometry. Analytical Chemistry. **79**, 6094-6101 (2007)

37. Harper, J.D., Charipar, N.A., Mulligan, C.C., Zhang, X., Cooks, R.G., Ouyang, Z.: Low-Temperature Plasma Probe for Ambient Desorption Ionization. Analytical Chemistry. **80**, 9097-9104 (2008)

38. Kauppila, T.J., Arvola, V., Haapala, M., Pól, J., Aalberg, L., Saarela, V., Franssila, S., Kotiaho, T., Kostiainen, R.: Direct analysis of illicit drugs by desorption atmospheric pressure photoionization. Rapid Communications in Mass Spectrometry. **22**, 979-985 (2008)

39. Luosujärvi, L., Kanerva, S., Saarela, V., Franssila, S., Kostiainen, R., Kotiaho, T., Kauppila, T.J.: Environmental and food analysis by desorption atmospheric pressure photoionization-mass spectrometry. Rapid Communications in Mass Spectrometry. **24**, 1343-1350 (2010)

40. Pól, J.e.a.: Automated Ambient Desorption-Ionization Platform for Surface Imaging Integrated with a Commercial Fourier Transform Ion Cyclotron Resonance Mass Spectrometer. Analytical Chemistry. **81**, 8479-8487 (2009)

41. Kauppila, T.J., Flink, A., Pukkila, J., Ketola, R.A.: Analysis of nitrogen-based explosives with desorption atmospheric pressure photoionization mass spectrometry. Rapid Communications in Mass Spectrometry. **30**, 467-475 (2016)

42. Suni, N.M., Aalto, H., Kauppila, T.J., Kotiaho, T., Kostiainen, R.: Analysis of lipids with desorption atmospheric pressure photoionization-mass spectrometry (DAPPI-MS) and desorption electrospray ionization-mass spectrometry (DESI-MS). Journal of Mass Spectrometry. **47**, 611-619 (2012)

43. Nemes, P., Vertes, A.: Laser Ablation Electrospray Ionization for Atmospheric Pressure, in Vivo, and Imaging Mass Spectrometry. Analytical Chemistry. **79**, 8098-8106 (2007)

44. Gao, J., Borton, D.J., 2nd, Owen, B.C., Jin, Z., Hurt, M., Amundson, L.M., Madden, J.T., Qian, K., Kenttamaa, H.I.: Laser-induced acoustic desorption/atmospheric pressure chemical ionization mass spectrometry. Journal of The American Society for Mass Spectrometry. **22**, 531-538 (2011)

45. Dow, A.R., Wittrig, A.M., Kenttämaa, H.I.: Laser-Induced Acoustic Desorption Mass Spectrometry. European Journal of Mass Spectrometry. **18**, 77-92 (2012)

46. Borton, D.J., Amundson, L.M., Hurt, M.R., Dow, A., Madden, J.T., Simpson, G.J., Kenttämaa, H.I.: Development of a High-Throughput Laser-Induced Acoustic Desorption Probe and Raster Sampling For Laser-Induced Acoustic Desorption/Atmospheric Pressure Chemical Ionization. Analytical Chemistry. **85**, 5720-5726 (2013)

47. Nyadong, L., Quinn, J.P., Hsu, C.S., Hendrickson, C.L., Rodgers, R.P., Marshall, A.G.: Atmospheric pressure laser-induced acoustic desorption chemical ionization mass spectrometry for analysis of saturated hydrocarbons. Analytical Chemistry. **84**, 7131-7137 (2012)

48. Cheng, S.-C., Cheng, T.-L., Chang, H.-C., Shiea, J.: Using Laser-Induced Acoustic Desorption/Electrospray Ionization Mass Spectrometry To Characterize Small Organic and Large Biological Compounds in the Solid State and in Solution Under Ambient Conditions. Analytical Chemistry. **81**, 868-874 (2009)

49. Linder, B., Seydel, U.: Laser Desorption Mass Spectrometry of Nonvolatlles under Shock Wave Conditions. Analytical Chemistry. 895-899 (1985)

50. Golovlev, V.V., Allman, S.L., Garrett, W.R., Chen, C.H.: Laser-induced acoustic desorption of electrons and ions. Applied Physics Letters. **71**, 852 (1997)

51. Zinovev, A.V., Veryovkin, I.V., Moore, J.F., Pellin, M.J.: Laser-Driven Acoustic Desorption of Organic Molecules from Back-Irradiated Solid Foils. Analytical Chemistry. 8232-8241 (2007)

52. Adamson, A.W.G., Alice P. John Wiley & Sons, New York (1997)

53. Hébert, H., Vidal, F., Martin, F., Kieffer, J.C., Nadeau, A., Johnston, T.W., Blouin, A., Moreau, A., Monchalin, J.P.: Ultrasound generated by a femtosecond and a picosecond laser pulse near the ablation threshold. Journal of Applied Physics. **98**, 033104 (2005)

54. Freund, L.B.S., S. Cambridge University Press, Cambridge (2003)

55. Zinovev, A.V., Veryovkin, I.V., Pellin, M.J.: Molecular Desorption by Laser–Driven Acoustic Waves: Analytical Applications and Physical Mechanisms. In: Beghi MG (ed.). InTech, (2011)

56. Zinovev, A.V., Veryovkin, I.V., Pellin, M.J., Iguchi, T., Watanabe, K.: Laser-induced desorption of organic molecules from front- and back-irradiated metal foils. AIP Conference Proceedings. **1104**, 200-206 (2009)

57. Pérez, J., Ramírez-Arizmendi, L.E., Petzold, C.J., Guler, L.P., Nelson, E.D., Kenttämaa, H.I.: Laser-induced acoustic desorption/chemical ionization in Fourier-transform ion cyclotron resonance mass spectrometry. International Journal of Mass Spectrometry. **198**, 173-188 (2000)

58. Campbell, J.L., Crawford, K.E., Kenttämaa, H.I.: Analysis of Saturated Hydrocarbons by Using Chemical Ionization Combined with Laser-Induced Acoustic Desorption/Fourier Transform Ion Cyclotron Resonance Mass Spectrometry. Analytical Chemistry. **76**, 959-963 (2004)

59. Peng, W.-P., Yang, Y.-C., Kang, M.-W., Tzeng, Y.-K., Nie, Z., Chang, H.-C., Chang, W., Chen, C.-H.: Laser-Induced Acoustic Desorption Mass Spectrometry of Single Bioparticles. Angewandte Chemie International Edition. **45**, 1423-1426 (2006)

60. Crawford, K.E., Campbell, J.L., Fiddler, M.N., Duan, P., Qian, K., Gorbaty, M.L., Kenttämaa, H.I.: Laser-Induced Acoustic Desorption/Fourier Transform Ion Cyclotron Resonance Mass Spectrometry for Petroleum Distillate Analysis. Analytical Chemistry. **77**, 7916-7923 (2005)

61. Peng, W.-P., Lin, H.-C., Lin, H.-H., Chu, M., Yu, A.L., Chang, H.-C., Chen, C.-H.: Charge-Monitoring Laser-Induced Acoustic Desorption Mass Spectrometry for Cell and Microparticle Mass Distribution Measurement. Angewandte Chemie International Edition. **46**, 3865-3869 (2007)

62. Chen, F.F. (3rd Edition ed.). Springer, Switzerland (2016)

63. Knoll, G.F. (3rd Edition ed.). John Wiley and Sons, New York (2000)

64. Paschen, F.: Ueber die zum Funkenübergang in Luft, Wasserstoff und Kohlensäure bei verschiedenen Drucken erforderliche Potentialdifferenz. Annalen der Physik. **273**, 69-96 (1889)

65. Go, D.B., Venkattraman, A.: Microscale gas breakdown: ion-enhanced field emission and the modified Paschen's curve. Journal of Physics D: Applied Physics. **47**, (2014)

66. Rumbach, P., Go, D.B.: Fundamental properties of field emission-driven direct current microdischarges. Journal of Applied Physics. **112**, 103302 (2012)

67. Becker, K.H., Schoenbach, K.H., Eden, J.G.: Microplasmas and applications. Journal of Physics D: Applied Physics. **39**, R55 (2006)

68. Roth, J. IOP Publishing Ltd., Philidelphia (1995)

69. Günther-Schulze, A.: Die Stromdichte des Normalen Kathodenfalles. Zeitschrift für Physik. **19**, 313-332 (1923)

70. Karl, H.S., Ahmed, E.-H., Wenhui, S., Marco, C.: High-pressure hollow cathode discharges. Plasma Sources Science and Technology. **6**, 468 (1997)

71. Schoenbach, K.H., El-Habachi, A., Moselhy, M.M., Shi, W., Stark, R.H.: Microhollow cathode discharge excimer lamps. Physics of Plasmas. **7**, 2186-2191 (2000)

72. Wieser, J., Salvermoser, M., Shawy, L.H., Ulrich, A., Murnick, D.E., Dahiz, H.: Lyman-alpha emission via resonant energy transfer. Journal of Physics B: Atomic, Molecular, and Optical Physics. **31**, 4589-4597 (1998)

73. Kurunczi, P.F., Shah, H., Becker, K.H.: Hydrogen Lyman-alpha and Lyman-beta emissions from high-pressure microhollow cathode discharges in Ne–H2 mixtures. Journal of Physics B: Atomic, Molecular, and Optical Physics. **32**, L651-L658 (1999)

74. Becker, K.H., Kurunczi, P.F., Schoenbach, K.H.: Collisional and radiative processes in high-pressure discharge plasmas. Physics of Plasmas. **9**, 2399 (2002)

75. Moselhy, M., Petzenhauser, I., Frank, K., Schoenbach, K.H.: Excimer emission from microhollow cathode discharges. Journal of Physics D: Applied Physics. **36**, 2922-2927 (2003)

76. Monge, M.E., Harris, G.A., Dwivedi, P., Fernandez, F.M.: Mass spectrometry: recent advances in direct open air surface sampling/ionization. Chemical Reviews. **113**, 2269-2308 (2013)

77. Haapala, M., al, e.: Desorption Atmospheric Pressure Photoionization. Analytical Chemistry. **79**, 7867-7872 (2007)

78. Johnson, P.V., Hodyss, R., Beauchamp, J.L.: Ion funnel augmented Mars atmospheric pressure photoionization mass spectrometry for in situ detection of organic molecules. Journal of The American Society for Mass Spectrometry. **25**, 1832-1840 (2014)

79. Wu, C., Dill, A.L., Eberlin, L.S., Cooks, R.G., Ifa, D.R.: Mass spectrometry imaging under ambient conditions. Mass Spectrometry Reviews. **32**, 218-243 (2013)

80. Sezer, U., Wörner, L., Horak, J., Felix, L., Tüxen, J., Götz, C., Vaziri, A., Mayor, M., Arndt, M.: Laser-Induced Acoustic Desorption of Natural and Functionalized Biochromophores. Analytical Chemistry. **87**, 5614-5619 (2015)

81. Jia, L., Weng, J., Zhou, Z., Qi, F., Guo, W., Zhao, L., Chen, J.: Note: Laser-induced acoustic desorption/synchrotron vacuum ultraviolet photoionization mass spectrometry for analysis of fragile compounds and heavy oils. Review of Scientific Instruments. **83**, 026105 (2012)

82. Cheng, S., Cheng, T.-L., Chang, H.-C., Shiea, J.: Using Laser-Induced Acoustic Desorption/Electrospray Ionization Mass Spectrometry To Characterize Small Organic and Large Biological Compounds in the Solid State and in Solution Under Ambient Conditions. Analytical Chemistry. **81**, 868-874 (2009)

83. Zinovev, A.V., Veryovkin, I.V., Moore, J.F., Pellin, M.J.: Laser-Driven Acoustic Desorption of Organic Molecules from Back-Irradiated Solid Foils. Analytical Chemistry. **79**, 8232-8241 (2007)

84. Shea, R.C., Petzold, C.J., Liu, J.-a., Kenttämaa, H.I.: Experimental Investigations of the Internal Energy of Molecules Evaporated via Laser-Induced Acoustic Desorption into a Fourier Transform Ion Cyclotron Resonance Mass Spectrometer. Analytical Chemistry. **79**, 1825-1832 (2007)

85. Reid, G.E., Tichy, S.E., Perez, J., O'Hair, R.A.J., Simpson, R.J., Kenttämaa, H.I.: N-Terminal Derivatization and Fragmentation of Neutral Peptides via Ion-Molecule Reactions with Acylium Ions: Toward Gas-Phase Edman Degradation? Journal of the American Chemical Society. **123**, 1184-1192 (2001)

86. Linder, B., Seydel, U.: Laser Desorption Mass Spectrometry of Nonvolatlles under Shock Wave Conditions. Analytical Chemistry. **57**, 895-899 (1985)

87. Nyadong, L., McKenna, A.M., Hendrickson, C.L., Rodgers, R.P., Marshall, A.G.: Atmospheric Pressure Laser-Induced Acoustic Desorption Chemical Ionization Fourier Transform Ion Cyclotron Resonance Mass Spectrometry for the Analysis of Complex Mixtures. Analytical Chemistry. **83**, 1616-1623 (2011)

88. Symonds, J.M., Gann, R.N., Fernandez, F.M., Orlando, T.M.: Microplasma discharge vacuum ultraviolet photoionization source for atmospheric pressure ionization mass spectrometry. Journal of The American Society for Mass Spectrometry. **25**, 1557-1564 (2014)

89. Stoeckli, M., Staab, D.: Reproducible Matrix Deposition for MALDI MSI Based on Open-Source Software and Hardware. Journal of The American Society for Mass Spectrometry. **26**, 911-914 (2015)

90. Kurunczi, P.F., Martus, K.E., Becker, K.H.: Neon excimer emission from pulsed high-pressure microhollow cathode discharge plasmas. International Journal of Mass Spectrometry. **223-224**, 37-43 (2003)

91. Paschen, F. Annalen der Physik. **273**, 69-96 (1889)

92. Wyllie, S.G., Amos, B.A., Tökés, L.: Electron Impact Induced Fragmentation of Cholesterol and Related C-5 Unsaturated Steroids. Journal of Organic Chemistry. **42**, (1977)

93. Lu, K.-T., Eiden, G.C., Weisshaar, J.C.: Toluene cation: nearly free rotation of the methyl group. Journal of Physical Chemistry. **96**, (1992)

94. Baer, T., Tsai, B.P., Smith, D., Murray, P.T.: Absolute unimolecular decay rates of energy selected metastable halobenzene ions. Journal of Chemical Physics. **64**, (1976)

95. Traeger, J.C., McLouglin, R.G., Nicholson, A.J.C.: Heat of formation for acetyl cation in the gas phase. Journal of the American Chemical Society. **104**, (1982)

96. Klein, E., Lukeš, V., Ilčin, M.: DFT/B3LYP study of tocopherols and chromans antioxidant action energetics. Chemical Physics. **336**, 51-57 (2007)

97. Thantu, N., Weber, P.M.: Dependence of two-photon ionization photoelectron spectra on laser coherence band width. Chemical Physics Letters. **214**, (1993)

98. Shchuka, M.I., Motyka, A.L., Topp, M.R.: Two-photon threshold ionization spectroscopy of perylene and Van der Waals complexes. Chemical Physics Letters. **164**, (1989)

99. Koizumi, H., Lacmann, K., Schmidt, W.F.: VUV light-induced electron emission from organic liquids. Journal of Electron Spectroscopy and Related Phenomena. **67**, 417-427 (1994)

100. Novak, I., Kovac, B.: Electronic structure and biological activity of steroids. Biophysical Chemistry. **78**, 233-240 (1999)

101. Ishihara, M., Sakagami, H.: QSAR of Molecular Structure and Cytotoxic Activity of Vitamin K2 Derivatives with Concept of Absolute Hardness. Anticancer Research. **27**, 4059-4064 (2007)

102. Amirav, A.: Electron Impact Mass Spectrometry of Cholesterol in Supersonic Molecular Beams. The Journal of Physical Chemistry. **94**, (1990)

103. Zhou, Z., Xie, M., Wang, Z., Qi, F.: Determination of absolute photoionization cross-sections of aromatics and aromatic derivatives. Rapid Communications in Mass Spectrometry. **23**, 3994-4002 (2009)

104. Cottin, H., Moore, M.H., Bénilan, Y.: Photodestruction of Relevant Interstellar Molecules in Ice Mixtures. The Astrophysical Journal. **590**, 874-881 (2003)

105. Räsänen, R.-M., Dwivedi, P., Fernández, F.M., Kauppila, T.J.: Desorption atmospheric pressure photoionization and direct analysis in real time coupled with travelling wave ion mobility mass spectrometry. Rapid Communications in Mass Spectrometry. **28**, 2325-2336 (2014)

106. Stevens, K.G., Bader, C.A., Sorvina, A., Brooks, D.A., Plush, S.E., Morrison, J.L.: Imaging and lipidomics methods for lipid analysis in metabolic and cardiovascular disease. Journal of Developmental Origins of Health and Disease. **8**, 566-574 (2017)

107. Colsch, B., Seyer, A., Boudah, S., Junot, C.: Lipidomic analysis of cerebrospinal fluid by mass spectrometry-based methods. Journal of Inherited Metabolic Disease. **38**, 53-64 (2015)

108. Han, X., Gross, R.W.: Quantitative analysis and molecular species fingerprinting of triacylglyceride molecular species directly from lipid extracts of biological samples by electrospray ionization tandem mass spectrometry. Analytical Biochemistry. **295**, 88-100 (2001)

109. Caboni, M.F.I., Giovanna; Pelillo, Marco; Marconi, Emanuele: Analysis of Fatty Acid Steryl Esters in Tetraploid and Hexaploid Wheats: Identification and Comparison between Chromatographic Methods. Journal of Agricultural and Food Chemistry. **53**, 7465-7472 (2005)

110. Gusev, A.J.W., William R.; Proctor, Andrew; Hercules, David M.: Improvement of Signal Reproducibility and Matrix/Comatrix Effects in MALDI Analysis. Analytical Chemistry. **67**, 1034-1041 (1995)

111. Karas, M.B., Doris; Hillenkamp, Franz: Influence of the wavelength in high-irradiance ultraviolet laser desorption mass spectrometry of organic molecules. Analytical Chemistry. **57**, 2935-2939 (1985)

112. Black, C., Chevallier, O.P., Elliott, C.T.: The current and potential applications of Ambient Mass Spectrometry in detecting food fraud. TrAC Trends in Analytical Chemistry. **82**, 268-278 (2016)

113. Simoneit, B.R.T., Rushdi, A.I., Deamer, D.W.: Abiotic formation of acylglycerols under simulated hydrothermal conditions and self-assembly properties of such lipid products. Advances in Space Research. **40**, 1649-1656 (2007)

114. Hussler, G.C., J.; Albrecht, P.: Novel families of tetra- and hexacyclic aromatic hopanoids predominant in carbonate rocks and crude oils. Organic Geochemistry. **6**, 39-49 (1984)

115. Nytoft, H.P.: Novel side chain methylated and hexacyclic hopanes: Identification by synthesis, distribution in a worldwide set of coals and crude oils and use as markers for oxic depositional environments. Organic Geochemistry. **42**, 520-539 (2011)

116. Nytoft, H.P., Vuković, N.S., Kildahl-Andersen, G., Rise, F., Životić, D.R., Stojanović, K.A.: Identification of a Novel Series of Benzohopanes and Their Geochemical Significance. Energy & Fuels. **30**, 5563-5575 (2016)

117. Georgiou, C.D., Deamer, D.W.: Lipids as universal biomarkers of extraterrestrial life. Astrobiology. **14**, 541-549 (2014)

118. Apel, C.L.D., David W.: Dehydration/Condensation Reaction: Increasing the Chemical Complexity of Amphiphiles on the Early Earth. Origins of Life and Evolution of Biospheres. **35**, 323-332 (2005)

119. Zinovev, A.V., Veryovkin, I.V., Moore, J.F., Pellin, M.J.: Laser-Driven Acoustic Desorption of Organic Molecules from Back-Irradiated Solid Foils. Analytical Chemistry. **79**, 8232-8241 (2007)

120. Launder, B.E.S., B.I.: Application of the Energy Dissipation Model of Turbulence to the Calculation of Flow Near a Spinning Disc. Letters in Heat and Mass Transfer. **1**, 131-138 (1974)

121. Harris, G.A.F., Facundo M.: Simulations and Experimental Investigation of Atmospheric Transport in an Ambient Metastable-Induced Chemical Ionization Source. Analytical Chemistry. **81**, 322-329 (2009)

122. Harris, G.A., Hostetler, D.M., Hampton, C.Y., Fernandez, F.M.: Comparison of the internal energy deposition of direct analysis in real time and electrospray ionization time-of-flight mass spectrometry. Journal of The American Society for Mass Spectrometry. **21**, 855-863 (2010)

123. Galhena, A.S.H., Glenn A.; Nyadong, Leonard; Murray, Kermit K.; Fernández, Facundo M.: Small Molecule Ambient Mass Spectrometry Imaging by Infrared Laser Ablation Metastable-Induced Chemical Ionization. Analytical Chemistry. **82**, 2178 - 2181 (2010)

124. Menter, F.R.: Two-equation eddy-viscosity turbulence models for engineering applications. AIAA Journal. **32**, 1598-1605 (1994)

125. Wilcox, D.C.: Formulation of the k-w Turbulence Model Revisited. AIAA Journal. **46**, 2823-2838 (2008)

126. Plat, J., Mensink, R.P.: Plant stanol and sterol esters in the control of blood cholesterol levels: mechanism and safety aspects. American Journal of Cardiology. **96**, 15D-22D (2005)

127. Abidi, S.L.: Chromatographic analysis of plant sterols in foods and vegetable oils. Journal of Chromotography A. **935**, 173-201 (2001)

128. Rejsek, J., Vrkoslav, V., Vaikkinen, A., Haapala, M., Kauppila, T.J., Kostiainen, R., Cvacka, J.: Thin-Layer Chromatography/Desorption Atmospheric Pressure

Photoionization Orbitrap Mass Spectrometry of Lipids. Analytical Chemistry. **88**, 12279-12286 (2016)

129. Scholz, B., Menzel, N., Lander, V., Engel, K.H.: An approach based on ultrahigh performance liquid chromatography-atmospheric pressure chemical ionization-mass spectrometry allowing the quantification of both individual phytosteryl and phytostanyl fatty acid esters in complex mixtures. Journal of Chromatography A. **1429**, 218-229 (2016)

130. Marcus, R.A.: Unimolecular Dissociations and Free Radical Recombination Reactions. The Journal of chemical physics. **20**, 359-364 (1952)

131. Eyring, H.: The Activated Complex in Chemical Reactions. The Journal of chemical physics. **3**, 107-115 (1935)

132. Sánchez, J.H., John L.: Biosynthesis of triacylglycerols and volatiles in olives. European Journal of Lipid Science and Technology. **104**, 564-573 (2002)

133. Kuhajda, F.P.: Fatty-Acid Synthase and Human Cancer: New Perspectives on Its Role in Tumor Biology. Nutrition. **16**, 202-208 (2000)

134. Servili, M., Sordini, B., Esposto, S., Urbani, S., Veneziani, G., Di Maio, I., Selvaggini, R., Taticchi, A.: Biological Activities of Phenolic Compounds of Extra Virgin Olive Oil. Antioxidants (Basel). **3**, 1-23 (2013)

135. Alberici, R.M., Fernandes, G.D., Porcari, A.M., Eberlin, M.N., Barrera-Arellano, D., Fernandez, F.M.: Rapid fingerprinting of sterols and related compounds in vegetable and animal oils and phytosterol enriched- margarines by transmission mode direct analysis in real time mass spectrometry. Food Chemistry. **211**, 661-668 (2016)

136. Fahy, E., Sud, M., Cotter, D., Subramaniam, S.: LIPID MAPS online tools for lipid research. Nucleic Acids Research. **35**, W606-612 (2007)

137. Li, C., Zhang, Y., Li, S., Wang, G., Xu, C., Deng, Y., Wang, S.: Mechanism of formation of trans fatty acids under heating conditions in triolein. Journal of Agricultural and Food Chemistry. **61**, 10392-10397 (2013)

138. Beltrán, G.D.R., Carmen; Sánchez, Sebastian; Martínez, Leopoldo: Influence of Harvest Date and Crop Yield on the Fatty Acid Composition of Virgin Olive Oils from Cv. Picual. Journal of Agricultural and Food Chemistry. **52**, 3434-3440 (2004)

139. Rybicki, M., Marynowski, L., Simoneit, B.R.T.: Benzohopane Series, Their Novel Di-, Tri-, and Tetraaromatic Derivatives, and Diaromatic 23- and 24-Norbenzohopanes from the Lower Jurassic Blanowice Formation, Southern Poland. Energy & Fuels. **31**, 2617-2624 (2017)

140. Liao, J., Lu, H., Sheng, G., Peng, P.a., Hsu, C.S.: Monoaromatic, Diaromatic, Triaromatic, and Tetraaromatic Hopanes in Kukersite Shale and Their Stable Carbon Isotopic Composition. Energy & Fuels. **29**, 3573-3583 (2015)

141. Deamer, D.W.: Boundary structures are formed by organic components of the Murchison carbonaceous chondrite. Nature. **317**, 792-794 (1985)

142. Laiko, V.V., Moyer, S.C., Cotter, R.J.: Atmospheric Pressure MALDI/Ion Trap Mass Spectrometry. Analytical Chemistry. **72**, 5239-5243 (2000)

143. Smith, D.R., Robb, D.B., Blades, M.W.: Comparison of dopants for charge exchange ionization of nonpolar polycyclic aromatic hydrocarbons with reversed-phase LC-APPI-MS. Journal of The American Society for Mass Spectrometry. **20**, 73-79 (2009)

144. Riboulleau, A., Mongenot, T., Baudin, F., Derenne, S., Largeau, C.: Factors controlling the survival of proteinaceous material in Late Tithonian kerogens (Kashpir Oil Shales, Russia). Organic Geochemistry. **33**, 1127-1130 (2002)

145. Riboulleau, A., Derenne, S., Largeau, C., Baudin, F.: Origin of contrasting features and preservation pathways in kerogens from the Kashpir oil shales (Upper Jurassic, Russian Platform). Organic Geochemistry. **32**, 647-665 (2001)

146. Beckett, R., Jue, Z., Giddings, J.C.: Determination of molecular weight distributions of fulvic and humic acids using flow field-flow fractionation. Environmental science & technology. **21**, 289-295 (1987)

147. Chin, Y.-P., Aiken, G., O'Loughlin, E.: Molecular weight, polydispersity, and spectroscopic properties of aquatic humic substances. Environmental science & technology. **28**, 1853-1858 (1994)

148. Schobert, H.H. Cambridge University Press, New York (2013)

149. Kvenvolden, K.A.: Organic geochemistry – A retrospective of its first 70 years. Organic Geochemistry. **37**, 1-11 (2006)

150. Tissot, B., Welte, D. Springer Science & Business Media, (2012)

151. Anonymous: Bitumen and heavy crudes: the energy security problem solved? Oil and Energy Trends. **31**, 3-6 (2006)

152. Sassen, R.: Geochemical and carbon isotopic studies of crude oil destruction, bitumen precipitation, and sulfate reduction in the deep Smackover Formation. Organic Geochemistry. **12**, 351-361 (1988)

153. Masson, J.F.: Brief Review of the Chemistry of Polyphosphoric Acid (PPA) and Bitumen. Energy & Fuels. **22**, 2637-2640 (2008)

154. Zhao, X., Liu, Y., Xu, C., Yan, Y., Zhang, Y., Zhang, Q., Zhao, S., Chung, K., Gray, M.R., Shi, Q.: Separation and Characterization of Vanadyl Porphyrins in Venezuela Orinoco Heavy Crude Oil. Energy & Fuels. **27**, 2874-2882 (2013)

155. Vandenbroucke, M., Largeau, C.: Kerogen origin, evolution and structure. Organic Geochemistry. **38**, 719-833 (2007)

156. Rossini, F.D., Mair, B.J.: Composition of Petroleum. American Chemical Society, (1951)

157. Rabkin, Y.M., Lafitte-Houssat, J.J.: Cooperative research in petroleum chemistry. Scientometrics. **1**, 327-338 (1979)

158. Treibs, A.: Chlorophyll- und Häminderivate in organischen Mineralstoffen. Angewandte Chemie. **49**, 682-686 (1936)

159. Wang, Z., Fingas, M.: Developments in the analysis of petroleum hydrocarbons in oils, petroleum products and oil-spill-related environmental samples by gas chromatography. Journal of Chromatography A. **774**, 51-78 (1997)

160. Boduszynski, M.M.: Composition of heavy petroleums. 2. Molecular characterization. Energy & Fuels. **2**, 597-613 (1988)

161. Smith, D.F., Podgorski, D.C., Rodgers, R.P., Blakney, G.T., Hendrickson, C.L.: 21 Tesla FT-ICR Mass Spectrometer for Ultrahigh-Resolution Analysis of Complex Organic Mixtures. Analytical Chemistry. **90**, 2041-2047 (2018)

162. Comisarow, M.B., Marshall, A.G.: Fourier transform ion cyclotron resonance spectroscopy. Chemical Physics Letters. **25**, 282-283 (1974)

163. Chen, L., Wang, T.C.L., Ricca, T.L., Marshall, A.G.: Phase-modulated stored waveform inverse Fourier transform excitation for trapped ion mass spectrometry. Analytical chemistry. **59**, 449-454 (1987)

164. Comisarow, M.B., Marshall, A.G.: Frequency-sweep fourier transform ion cyclotron resonance spectroscopy. Chemical Physics Letters. **26**, 489-490 (1974)

165. Zhurov, K.O., Kozhinov, A.N., Tsybin, Y.O.: Evaluation of High-Field Orbitrap Fourier Transform Mass Spectrometer for Petroleomics. Energy & Fuels. **27**, 2974-2983 (2013)

166. McKenna, A.M., Nelson, R.K., Reddy, C.M., Savory, J.J., Kaiser, N.K., Fitzsimmons, J.E., Marshall, A.G., Rodgers, R.P.: Expansion of the Analytical Window for Oil Spill Characterization by Ultrahigh Resolution Mass Spectrometry: Beyond Gas Chromatography. Environmental Science & Technology. **47**, 7530-7539 (2013)

167. Kujawinski, E.B.: Electrospray Ionization Fourier Transform Ion Cyclotron Resonance Mass Spectrometry (ESI FT-ICR MS): Characterization of Complex Environmental Mixtures. Environmental Forensics. **3**, 207-216 (2002)

168. Bae, E., Na, J.-G., Chung, S.H., Kim, H.S., Kim, S.: Identification of about 30 000 Chemical Components in Shale Oils by Electrospray Ionization (ESI) and Atmospheric Pressure Photoionization (APPI) Coupled with 15 T Fourier Transform Ion Cyclotron Resonance Mass Spectrometry (FT-ICR MS) and a Comparison to Conventional Oil. Energy & Fuels. **24**, 2563-2569 (2010)

169. Purcell, J.M., Juyal, P., Kim, D.-G., Rodgers, R.P., Hendrickson, C.L., Marshall, A.G.: Sulfur Speciation in Petroleum: Atmospheric Pressure Photoionization or Chemical Derivatization and Electrospray Ionization Fourier Transform Ion Cyclotron Resonance Mass Spectrometry. Energy & Fuels. **21**, 2869-2874 (2007)

170. Haapala, M., Purcell, J.M., Saarela, V., Franssila, S., Rodgers, R.P., Hendrickson, C.L., Kotiaho, T., Marshall, A.G., Kostiainen, R.: Microchip Atmospheric Pressure Photoionization for Analysis of Petroleum by Fourier Transform Ion Cyclotron Resonance Mass Spectrometry. Analytical Chemistry. **81**, 2799-2803 (2009)

171. Ruddy, B.M., Hendrickson, C.L., Rodgers, R.P., Marshall, A.G.: Positive Ion Electrospray Ionization Suppression in Petroleum and Complex Mixtures. Energy & Fuels. **32**, 2901-2907 (2018)

172. Eckert, P.A., Roach, P.J., Laskin, A., Laskin, J.: Chemical Characterization of Crude Petroleum Using Nanospray Desorption Electrospray Ionization Coupled with High-Resolution Mass Spectrometry. Analytical Chemistry. **84**, 1517-1525 (2012)

173. Huang, Z., Horke, D.A., Küpper, J.: Laser-induced acoustic desorption of thermally stable and unstable biomolecules. arXiv. (2018)

174. Huang, Z., Ossenbrüggen, T., Rubinsky, I., Schust, M., Horke, D.A., Küpper, J.: Development and Characterization of a Laser-Induced Acoustic Desorption Source. Analytical Chemistry. **90**, 3920-3927 (2018)

175. Corilo, Y.E., Vaz, B.G., Simas, R.C., Lopes Nascimento, H.D., Klitzke, C.F., Pereira, R.C.L., Bastos, W.L., Santos Neto, E.V., Rodgers, R.P., Eberlin, M.N.: Petroleomics by EASI(±) FT-ICR MS. Analytical Chemistry. **82**, 3990-3996 (2010)

176. Schantz, M.M., Kucklick, J.R.: Interlaboratory Analytical Comparison Study to Support Deepwater Horizon Natural Resource Damage Assessment: Description and Results for Crude Oil QA10OIL01. National Institute of Standards and Technology (NIST) Report, Gaithersburg, MD. **20899**, (2011)

177. DiStefano, V.H., McFarlane, J., Anovitz, L.M., Stack, A.G., Gordon, A.D., Littrell, K.C., Chipera, S.J., Hunt, R.D., Lewis, S.A., Hale, R.E., Perfect, E.: Extraction of

organic compounds from representative shales and the effect on porosity. Journal of Natural Gas Science and Engineering. **35**, 646-660 (2016)

178. Kim, S., Rodgers, R.P., Marshall, A.G.: Truly "exact" mass: Elemental composition can be determined uniquely from molecular mass measurement at ~0.1mDa accuracy for molecules up to ~500Da. International Journal of Mass Spectrometry. **251**, 260-265 (2006)

179. Sleighter, R.L., McKee, G.A., Liu, Z., Hatcher, P.G.: Naturally present fatty acids as internal calibrants for Fourier transform mass spectra of dissolved organic matter. Limnology and Oceanography: Methods. **6**, 246-253 (2008)

180. Yuen, G.U., Kvenvolden, K.A.: Monocarboxylic Acids in Murray and Murchison Carbonaceous Meteorites. Nature. **246**, 301 (1973)

181. Purcell, J.M., Hendrickson, C.L., Rodgers, R.P., Marshall, A.G.: Atmospheric Pressure Photoionization Fourier Transform Ion Cyclotron Resonance Mass Spectrometry for Complex Mixture Analysis. Analytical Chemistry. **78**, 5906-5912 (2006)

182. Marotta, E., Paradisi, C.: A mass spectrometry study of alkanes in air plasma at atmospheric pressure. Journal of The American Society for Mass Spectrometry. **20**, 697-707 (2009)

183. Gao, J., Owen, B.C., Borton, D.J., Jin, Z., Kenttämaa, H.I.: HPLC/APCI Mass Spectrometry of Saturated and Unsaturated Hydrocarbons by Using Hydrocarbon Solvents as the APCI Reagent and HPLC Mobile Phase. Journal of The American Society for Mass Spectrometry. **23**, 816-822 (2012)

184. Krajewski, L.C., Rodgers, R.P., Marshall, A.G.: 126 264 Assigned Chemical Formulas from an Atmospheric Pressure Photoionization 9.4 T Fourier Transform Positive Ion Cyclotron Resonance Mass Spectrum. Analytical Chemistry. **89**, 11318-11324 (2017)

185. Marshall, A.G., Wang, T.C.L., Ricca, T.L.: Tailored excitation for Fourier transform ion cyclotron mass spectrometry. Journal of the American Chemical Society. **107**, 7893-7897 (1985)

186. Savory, J.J., Kaiser, N.K., McKenna, A.M., Xian, F., Blakney, G.T., Rodgers, R.P., Hendrickson, C.L., Marshall, A.G.: Parts-Per-Billion Fourier Transform Ion Cyclotron Resonance Mass Measurement Accuracy with a "Walking" Calibration Equation. Analytical Chemistry. **83**, 1732-1736 (2011)

187. Korsten, H.: Characterization of hydrocarbon systems by DBE concept. AIChE Journal. **43**, 1559-1568 (1997)

188. Koch, B.P., Dittmar, T.: From mass to structure: an aromaticity index for high-resolution mass data of natural organic matter. Rapid Communications in Mass Spectrometry. **20**, 926-932 (2006)

189. Zheng, L., Huang, X.: Occurrence of a tetraaromatic hopane in the late Holocene peat deposit, central China. Organic Geochemistry. **106**, 25-29 (2017)

190. Jin, J.M., Kim, S., Birdwell, J.E.: Molecular Characterization and Comparison of Shale Oils Generated by Different Pyrolysis Methods. Energy & Fuels. **26**, 1054-1062 (2012)

191. Hall, G.J., Frysinger, G.S., Aeppli, C., Carmichael, C.A., Gros, J., Lemkau, K.L., Nelson, R.K., Reddy, C.M.: Oxygenated weathering products of Deepwater Horizon oil come from surprising precursors. Marine Pollution Bulletin. **75**, 140-149 (2013)

192. Ray, P.Z., Chen, H., Podgorski, D.C., McKenna, A.M., Tarr, M.A.: Sunlight creates oxygenated species in water-soluble fractions of Deepwater horizon oil. Journal of Hazardous Materials. **280**, 636-643 (2014)

193. Head, I.M., Jones, D.M., Larter, S.R.: Biological activity in the deep subsurface and the origin of heavy oil. Nature. **426**, 344 (2003)

194. Liu, P., Shi, Q., Chung, K.H., Zhang, Y., Pan, N., Zhao, S., Xu, C.: Molecular Characterization of Sulfur Compounds in Venezuela Crude Oil and Its SARA Fractions by Electrospray Ionization Fourier Transform Ion Cyclotron Resonance Mass Spectrometry. Energy & Fuels. **24**, 5089-5096 (2010)

195. López, L., Lo Mónaco, S.: Geochemical implications of trace elements and sulfur in the saturate, aromatic and resin fractions of crude oil from the Mara and Mara Oeste fields, Venezuela. Fuel. **83**, 365-374 (2004)

196. Moselhy, M., Petzenhauser, I., Frank, K., Schoenbach, K.H.: Excimer emission from microhollow cathode argon discharges. Journal of Physics D: Applied Physics. **36**, 2922-2927 (2003)

197. Martin, V., Bauville, G., Fleury, M., Puech, V.: Exciplex emission induced by nanosecond-pulsed microdischarge arrays operating at high repetition rate frequency. Plasma Sources Science and Technology. **21**, 065001 (2012)

198. Lee, B.J., Rahaman, H., Nam, S.H., Iberler, M., Jacoby, J., Frank, K.: Excimer emission from pulsed microhollow cathode discharges in xenon. Physics of Plasmas. **20**, 123510 (2013)

199. Stephens, J., Fierro, A., Trienekens, D., Dickens, J., Neuber, A.: Optimizing drive parameters of a nanosecond, repetitively pulsed microdischarge high power 121.6 nm source. Plasma Sources Science and Technology. **24**, 015013 (2014)

200. Stephens, J., Fierro, A., Walls, B., Dickens, J., Neuber, A.: Nanosecond, repetitively pulsed microdischarge vacuum ultraviolet source. Applied Physics Letters. **104**, 074105 (2014)

201. Corilo, Y.E.: PetroOrg software. Florida State University. All rights reserved. (2014)

202. Tolić, N., Liu, Y., Liyu, A., Shen, Y., Tfaily, M.M., Kujawinski, E.B., Longnecker, K., Kuo, L.-J., Robinson, E.W., Paša-Tolić, L., Hess, N.J.: Formularity: Software for Automated Formula Assignment of Natural and Other Organic Matter from Ultrahigh-Resolution Mass Spectra. Analytical Chemistry. **89**, 12659-12665 (2017)

203. Smith, D.G.A., Burns, L.A., Sirianni, D.A., Nascimento, D.R., Kumar, A., James, A.M., Schriber, J.B., Zhang, T., Zhang, B., Abbott, A.S., Berquist, E.J., Lechner, M.H., Cunha, L.A., Heide, A.G., Waldrop, J.M., Takeshita, T.Y., Alenaizan, A., Neuhauser, D., King, R.A., Simmonett, A.C., Turney, J.M., Schaefer, H.F., Evangelista, F.A., DePrince, A.E., Crawford, T.D., Patkowski, K., Sherrill, C.D.: Psi4NumPy: An Interactive Quantum Chemistry Programming Environment for Reference Implementations and Rapid Development. Journal of Chemical Theory and Computation. **14**, 3504-3511 (2018)

204. Parrish, R.M., Burns, L.A., Smith, D.G.A., Simmonett, A.C., DePrince, A.E., Hohenstein, E.G., Bozkaya, U., Sokolov, A.Y., Di Remigio, R., Richard, R.M., Gonthier, J.F., James, A.M., McAlexander, H.R., Kumar, A., Saitow, M., Wang, X., Pritchard, B.P., Verma, P., Schaefer, H.F., Patkowski, K., King, R.A., Valeev, E.F., Evangelista, F.A., Turney, J.M., Crawford, T.D., Sherrill, C.D.: Psi4 1.1: An Open-Source Electronic Structure Program Emphasizing Automation, Advanced Libraries, and Interoperability. Journal of Chemical Theory and Computation. **13**, 3185-3197 (2017)

205. Dais, P., Hatzakis, E.: Quality assessment and authentication of virgin olive oil by NMR spectroscopy: A critical review. Analytica Chimica Acta. **765**, 1-27 (2013)

206. Georgouli, K., Martinez Del Rincon, J., Koidis, A.: Continuous statistical modelling for rapid detection of adulteration of extra virgin olive oil using mid infrared and Raman spectroscopic data. Food Chemistry. **217**, 735-742 (2017)

207. Iglesias-Otero, M.A., Esteki, M., Moldes, O.A., Mejuto, J.C., Simal-Gandara, J.: A critical review on the use of artificial neural networks in olive oil production, characterization and authentication AU - Gonzalez-Fernandez, I. Critical Reviews in Food Science and Nutrition. 1-14 (2018)

208. Savitzky, A., Golay, M.J.E.: Smoothing and differentiation of data by simplified least squares procedures. Analytical chemistry. **36**, 1627-1639 (1964)

209. Donoho, D.L.: De-noising by soft-thresholding. IEEE transactions on information theory. **41**, 613-627 (1995)

210. Ràfols, P., Vilalta, D., Brezmes, J., Cañellas, N., del Castillo, E., Yanes, O., Ramírez, N., Correig, X.: Signal preprocessing, multivariate analysis and software tools for MA(LDI)-TOF mass spectrometry imaging for biological applications. Mass Spectrometry Reviews. **37**, 281-306 (2018)

211. Tikunov, Y.M., Laptenok, S., Hall, R.D., Bovy, A., de Vos, R.C.H.: MSClust: a tool for unsupervised mass spectra extraction of chromatography-mass spectrometry ion-wise aligned data. Metabolomics. **8**, 714-718 (2012)

212. Dieterle, F., Ross, A., Schlotterbeck, G., Senn, H.: Probabilistic quotient normalization as robust method to account for dilution of complex biological mixtures. Application in 1H NMR metabonomics. Analytical chemistry. **78**, 4281-4290 (2006)

213. Wei, H., Wang, N., Duan, Z., He, F.: Experimental and simulation study of pulsed micro-hollow cathode discharge in atmospheric-pressure helium. Physics of Plasmas. **25**, 123513 (2018)